Doctoral Dissertation

DFT Study of the Adsorption States of an Organic Molecule Overlayer and a Single Platinum Atom on Graphene

密度汎関数理論によるグラフェン上の有機分子層
および単原子Ptの吸着状態に関する研究

Sasfan Arman Wella

サスファン　アルマン　ウェラ

February 2019

Department of Precision Science and Technology

Graduate School of Engineering

Osaka University

Abstract

Graphene is attracting enormous attention due to its outstanding electrical, mechanical, thermal and chemical properties. Understanding of the interactions of graphene with other atoms, nano-particles, or molecules is indispensable in order to find novel or improved usage of graphene in wide range of applications. First-principles electronic structure theory is a very powerful tool to understand the atomic, electronic, and chemical properties of materials in atomic scale and to clarify important factors governing the properties of materials, which should be useful knowledge to design new materials with desired properties. In this Ph.D work, I used density functional theory (DFT) and investigated three topics.

As the first topic, I studied the interaction of graphene with organic molecules, especially, the effect of organic adsorbates on the image potential states (IPSs), which are relevant to molecular-based electronic devices. In the case of metal surfaces, the presence of IPSs is a universal nature, characterized by a set of unoccupied states quantized to a Rydberg series analogous to the hydrogen atom. In this study, I extended the concept of the IPS-derived interlayer states to molecular adsorption on solid surfaces. Naphthalene adsorption on highly oriented pyrolitic graphite (HOPG) is typically used as a model of aromatic molecules physisorbed on solid surfaces. Recent experiments have revealed that naphthalene molecules form a well-ordered superstructure on graphite, and more importantly, the lowest IPS behaves almost as a free electron, despite the presence of the naphthalene overlayer. This is explained by assuming that the molecular overlayer is a dielectric medium with uniform permittivity and only shifts the Rydberg series with the effective mass m^* unchanged from the electronic mass m_e. On the other hand, the well-known Kronig-Penny theory suggests an increase in m^* if naphthalene acts as a periodic potential for the IPSs. In order to develop a coherent picture of the IPSs at organic-solid interfaces, I performed first-principles calculations of a simplified model composed of naphthalene on graphene. The results show that the intermolecular interaction induces IPS-like states on the naphthalene overlayer, which hybridize with the graphene IPSs in the bonding and antibonding manners. The impact of the naphthalene adsorption appears most prominently in the anisotropic effective mass of the resultant hybrid IPSs, which strongly reflects the molecular structure of naphthalene. It is expected that similar hybrid IPSs widely exist at interface of organic-solid surfaces.

As the second topic, I studied the interaction of graphene with single platinum (Pt) atoms to clarify the origin for the improved catalytic reactivities. The single-atom catalysis is one of the most promising ways to enhance the catalytic activity and to reduce the amount of precious metals used. Pt atoms deposited on graphene are reported to show enhanced catalytic activity for some chemical reactions, e.g. methanol oxidation in direct methanol fuel cells. However, the precise atomic structure, the key to understand the origin of the improved catalytic activity, is yet to be clarified. As my contribution in this issue, I present here a computational study to investigate the structure of Pt adsorbed on graphene with special emphasis on the edges of graphene nanoribbon (GNR). By means of DFT-based thermodynamics, it is found that the single Pt atom is preferentially adsorbed at the edge rather than on graphene, a good news regarding the search of a dense dispersion of metal single atoms on a support material. The calculated core level shifts (CLSs) for the stable structures are in reasonable agreement with the experiment, corroborating our findings. Large positive CLS indicate the strong interaction between single Pt atoms and graphene.

As the third topic, the catalytic activities of single Pt atoms anchored at the edges of GNRs (Pt@GNRs) are predicted based on the adsorption energies from DFT calculations combined with some kinetic models. Compared with the Pt(111) surface, Pt@GNRs show a better activity in CO oxidation reaction, which is presumably the origin for the improved CO tolerance in the anode electrode in direct methanol fuel cell. Some Pt@GNRs in metastable configurations are expected to be efficient catalysts for oxygen reduction reaction. This study could be a basis for further investigation of the development of single-atom catalysts based on platinum and graphene related materials.

Contents

List of Figures

List of Tables

I dedicate this dissertation to my beloved parents,

J. Wilson Limbong (†) *and* ***R. br. Simbolon****,*

whose love, support, and prayer

always motivated me to complete this work.

Chapter 1

General Introduction

1.1 Overview

Argument from Landau and Peierls [1, 2], that strictly two-dimensional (2D) crystals could not exist because they will be thermodynamically unstable, has lasted for a long time until A. K. Geim and K. S. Novoselov proofed the realness of 2D material in 2004 [3]. They invented an atomically thin 2D material formed a honeycomb pattern, named graphene. Graphene has basically a similar structure to graphite. However, graphene has unique properties that exceed those of graphite. In term of surface to volume ratio (aspect ratio), graphene as a 2D material has higher aspect ratio than graphite. Graphite is a very brittle material, it is not suitable to be used for structural material. Graphene, on the other hand, is the strongest material with an intrinsic tensile strength of 130.5 GPa and a Young's modulus of 1 TPa (150000000 psi) [4]. Another useful property of graphene is that it has high electrical conductivity with electron mobility up to $\sim$ 10000 $cm^2/V.s$ at room temperature [3]. It is due to pi (π) electrons in graphene. One carbon atom

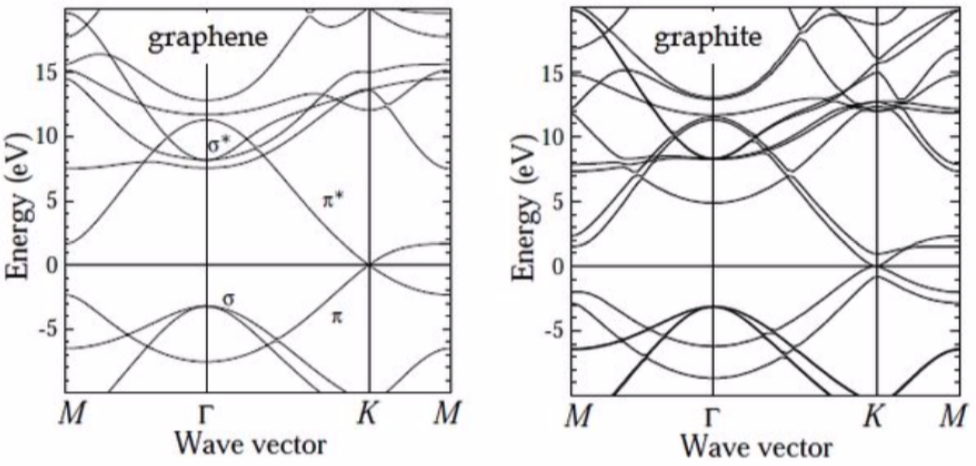

FIGURE 1.1: Electronic band structures for (a) graphene, and (b) graphite. This image was taken from Ref. 5.

has four valence electrons: three of them are used for the sp^2 bonds in graphene, leaving one electron freely available called π electron. The π electrons are located in the normal direction of the graphene sheet. As shown in Fig. 1.1(a), there is a Dirac cone in the vicinity of Fermi level, in particular at the K-point in the Brillouin zone, while it does not appear in graphite [Fig. 1.1(b)]. In the vicinity of Dirac point, the π and π^* orbitals have linear energy bands, meaning that the electrons and holes have zero effective mass. Therefore, they can travel relatively long distances without scattering. It makes graphene is considered as a material with very high electron mobility and conductivity. Note that, in order to make this high level of electronic conductivity becomes realistic, doping (with electrons or holes) is essentially required to overcome the zero density of states at the Dirac points of graphene. Overall, the superb properties of graphene make it becomes a very promising material to be widely used for many applications.

1.1.1 Graphene as a substrate for molecular-based electronic devices

Nowadays, molecular-based electronic devices are growing rapidly because this kind of technology offers some advantages, such as low-production cost, flexible, light, and friendly for the environment. Owing to its properties, graphene should be suitable to be applied for this application. To this end, it is necessary to investigate accurately the interaction between graphene and a specific organic molecule, especially the electronic properties of that system. For metal surfaces, it is a universal nature to find image potential states (IPSs), a set of unoccupied states quantized to a Rydberg series analogous to the hydrogen atom, on them. Moreover, the emergence of such states is also found in graphene. When graphene is interacted with an organic molecule, it is expected that the featureof IPSs is modified. Therefore, in this study, it is interesting to extend the concept of the IPS-derived interlayer states to molecular adsorption on solid surfaces.

Naphthalene on highly oriented pyrolytic graphite (HOPG) is a prototype system of aromatic molecules physisorbed on a solid surface and has been investigated intensively thus far. It has been reported that the effective mass m^* of the lowest IPS of the adsorbed system is unchanged from the electronic mass m_e despite the presence of the well-ordered naphthalene molecules on HOPG. It is suggested that molecule overlayer is a dielectric medium with uniform permittivity. Thus, only the Rydberg series are shifted while the m^* is unchanged. However, based on Kronig-Penny theory, the m^* should be increased if the well-ordered naphthalenes act as a periodic potential for the IPSs. In order to develop a coherent picture

of the IPSs at organic-solid interfaces, as my contribution in this issue, I studied theoretically the interaction between graphene and a simple organic molecule, naphthalene, using van der Waals density functional method, which is successfully improving the description of unoccupied states of the graphene. The detail insight of the organic-solid interfaces will help for developing molecule-based electronic devices.

1.1.2 Graphene as a support material for metal catalyst

Many people in the world are focusing on solving the 3E-Trilema (Economy, Energy, Environment). Reducing the dependence on fossil fuels could be one of the solutions; not only because fossil fuels are non-renewable energy, but also the pollution from these fuels is not friendly for the environment. Thus, an alternative energy technology, which is cheap, renewable, and also friendly for the environment, is then required to solve the problem. Fuel cells are one of the most promising candidates to be an alternative energy. Basically, fuel cells convert chemical energy to electrical energy via oxygen reduction reactions. Fig. 1.2 shows the work principle of direct-methanol fuel cell (DMFC) as one kind of fuel cells. By supplying methanol and water in anode and also air (oxygen) in cathode, this fuel cell can produce the electricity with carbon dioxide and water vapor as emissions. According to its supplies and emissions, fuel cell fulfills two criterion (economic and environment) needed as an alternative energy. However, efficiency of the fuel cell, which depends on the reaction both in anode and cathode, is also important to be considered. Unfortunately, methanol oxidation reaction in anode is quite

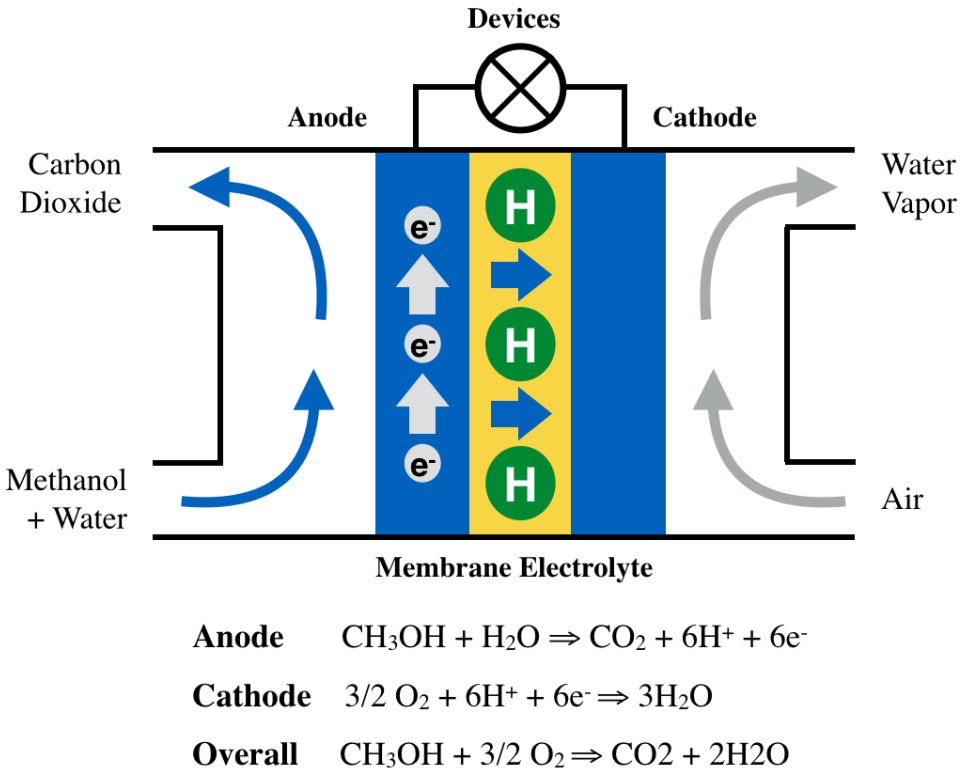

FIGURE 1.2: Work principle of DMFC.

slow, making production of electron is low as well. Accordingly, high-performance electrocatalysts are highly desired to enhance performance of the fuel cell.

So far, platinum (Pt) has shown the greatest potential as homogeneous catalyst material because it can be used for both hydrogen oxidation and oxygen reduction at low temperature and also can withstand the acidic conditions. Nevertheless, platinum catalyst has several limits. Not only because its price is expensive, but also it is potentially poisoned by CO which can affect the performance of the fuel cell itself. Huge efforts have been devoted to overcome these problems, including the use of non-precious metals for Pt–metal alloys, or the use of noble metal-free catalysts. Particularly interesting are Pt clusters supported by graphitic materials, such as carbon black, carbon nanotubes, and graphene, which have been extensively investigated thus far. A better catalytic activity of small Pt

clusters supported by graphene sheets has been demonstrated experimentally lead to the hypothesis that downsizing the Pt clusters to single atoms can enhance the catalytic activity. Indeed, single Pt atoms deposited on graphene are reported to show enhanced catalytic activity for some chemical reactions, e.g. methanol oxidation in direct methanol fuel cells. However, the precise atomic structure, the key to understand the origin of the improved catalytic activity, is yet to be clarified. Therefore, as my contribution in this issue, the details of the interaction between Pt and graphene as a support material is studied here, and further the insight of their interaction with the molecules will help to design new efficient catalysts for fuel cell electrodes.

1.2 Outline of Dissertation

This dissertation is divided into two main parts: the adsorption of naphthalene on graphene as a typical model to understand the interaction between organic molecules and solid surfaces; and single platinum atom supported by graphene edges as a catalyst for oxidation reduction reactions. Theoretical background related to this research is provided in **Chapter 2**. Here, I briefly explain about density functional theory. In **Chapter 3**, the investigation the adsorption geometry and electronic properties of naphthalene on graphene is presented. Here, the modification of the IPSs due to the presence of the organic molecules are discussed. **Chapters 4 and 5** are about single Pt atom supported by graphene as a catalyst. The stability of single Pt atom on several graphitic system is investigated and the results are discussed in **Chapter 4**. It is concluded that single Pt atom is

preferentially adsorbed at the edge of graphene. In **Chapter 5** the adsorption of some molecules on single Pt atom supported by graphene nanoribbons is shown. The mechanisms to predict the catalytic activity of the single Pt atom catalyst supported by graphene for CO oxidation and oxygen reduction reaction are explained here. Finally, all findings in this dissertation are summarized in **Chapter 6**. The future outlook on this study is also discussed.

References

[1] R. Peierls, "Quelques propriétés typiques des corps solides," *Annales de l'institut Henri Poincaré*, vol. 5, no. 3, pp. 177–222, 1935.

[2] L. D. Landau, "Zur theorie der phasenumwandlungen ii," *Phys. Z. Sowjetunion*, vol. 11, pp. 26–35, 1937.

[3] K. S. Novoselov, A. K. Geim, S. V. Morozov, D. Jiang, Y. Zhang, S. V. Dubonos, I. V. Grigorieva, and A. A. Firsov, "Electric field effect in atomically thin carbon films," *Science*, vol. 306, no. 5696, pp. 666–669, 2004.

[4] C. Lee, X. Wei, J. W. Kysar, and J. Hone, "Measurement of the elastic properties and intrinsic strength of monolayer graphene," *Science*, vol. 321, no. 5887, pp. 385–388, 2008.

[5] S. Reich, C. Thomsen, and J. Maultzsc, *Carbon Nanotubes: Basic Concepts and Physical Properties*. Weinheim: Cambridge, 2004.

Chapter 2

Methods

2.1 Many-body System

In quantum mechanics, a state of a physical system can be described by a state vector or a wave function. In system of nuclei and electrons (see Fig. 2.1), interaction among electrons and also interaction between electrons and nuclei could be known by determining the wave function accurately.

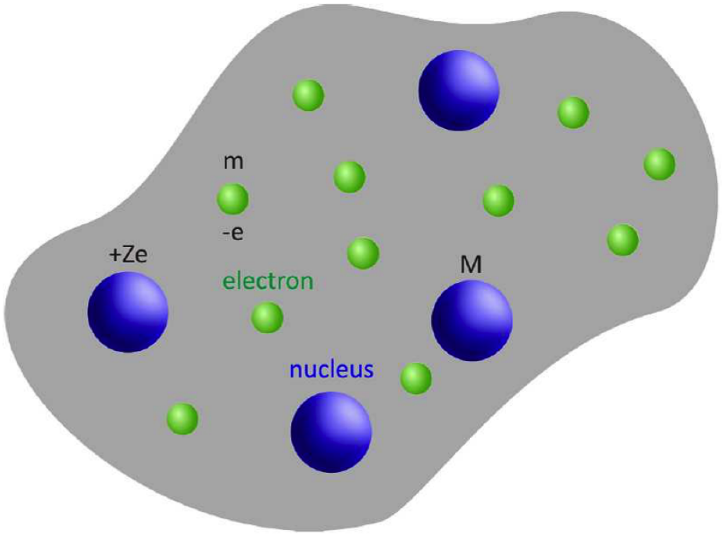

FIGURE 2.1: System of nuclei and electrons.

In order to know the behavior of the system of nucleus and electrons, we need to solve the time-independent Schrödinger:

$$\hat{H}\,\Psi\Big(\Big\{\vec{R}_N,\vec{r}_M\Big\}\Big) = E\,\Psi\Big(\Big\{\vec{R}_N,\vec{r}_M\Big\}\Big) \tag{2.1}$$

where, N, M are number of nuclei and number of electrons, respectively. $\hat{H}$ is Hamiltonian operator which represents total energy of the system. The Hamiltonian operator can be written as

$$\begin{aligned}\hat{H} &= -\frac{1}{2}\sum_{i}^{N}\nabla_i^2 - \frac{1}{2}\sum_{I}^{M}\frac{1}{M_I}\nabla_I^2 - \sum_{i}^{N}\sum_{I}^{M}\frac{Z_I}{r_{iI}} \\ &+ \sum_{i}^{N}\sum_{j\neq i}^{N}\frac{1}{r_{ij}} + \sum_{i}^{M}\sum_{J\neq I}^{M}\frac{Z_I Z_J}{R_{IJ}}\end{aligned} \tag{2.2}$$

where, the first and the second terms are kinetic energy of electrons and kinetic energy of nucleus, respectively. The third term is potential interaction among electrons. The fourth term is potential interaction among nuclei. The last term is potential interaction between electrons and nuclei.

2.2 Born-Oppenheimer Approximation

As mentioned earlier, the wave function Ψ contains many information about characteristic of the system. Solving Eq. 2.1, absolutely, is not an easy job. It is desired to simplify the Hamiltonian in Eq. 2.2 to reduce the complexity of the calculation. To this, let us use the fact that mass of a single nuclei is approximately 1800 times larger than mass of the electron. Here, the movement of the electrons is much

faster than the movement of the nuclei. This implies that electrons are moving in fixed nucleus, relatively. Therefore, the term of kinetic energy of nuclei can be neglected. For the term of potential interaction among nuclei can be substituted with a constant. Thus, after simplification the Hamiltonian can be rewritten as

$$\begin{aligned} \hat{H} &= -\frac{1}{2}\sum_{i}^{N}\nabla_i^2 + \sum_{i}^{N}\sum_{j\neq i}^{N}\frac{1}{r_{ij}} - \sum_{i}^{N}\sum_{I}^{M}\frac{Z_I}{r_{iI}} \\ &= \hat{T} + \hat{V}_{\text{ee}} + \hat{V}_{\text{ne}} \end{aligned}$$

Even though the Hamiltonian has been simplified, it is still difficult to solve the Schrödinger equation analytically. However, using some methods, the analytical solutions can be approximated. One of these methods is density functional theory.

2.3 Density Functional Theory

Density functional theory (DFT) is a method which success to describe the ground state of molecule or solid system. DFT describes the energy function of the system based on electronic density, $E(n\{\vec{r}_i\})$. It is different with Hartree-Fock method which describes the energy function of the system based on wave function, $E(\Psi)$. This approach has been proposed independently by L. H. Thomas and E. Fermi in 1927 [1, 2]. However, the Thomas-Fermi method is not able to explain some electronic properties of the material system. Finally, in 1964, the new DFT approach was proposed by P. Hohenberg and W. Kohn [3].

2.3.1 Hohenberg-Kohn Theorems

Hohenberg-Kohn theorem is the fundamental theory of DFT. There are two fundamental theorems which are giving a great contribution for DFT.

Theorem I :

The external potential, $V_{\text{ext}}(\vec{r})$, is uniquely determined by the electronic density, $n(\vec{r})$, except for a trivial additive constant. Since in turn $V_{\text{ext}}(\vec{r})$ fixes $\hat{H}$, we see that the full many particle ground state is a unique functional of $n(\vec{r})$.

Proof: Let us use other external potential,

$$V'_{\text{ext}}(\vec{r}) = V_{\text{ext}}(\vec{r}) + C$$

where, C is a constant. Both $V_{\text{ext}}(\vec{r})$ and $V'_{\text{ext}}(\vec{r})$ giving the same $n(\vec{r})$ for its ground state. Now, we have two Hamiltonians $\hat{H}$ and $\hat{H}'$ whose ground densities were the same although the normalized wave functions, Ψ and Ψ', would be different. Therefore, we have a chance to use Ψ' for $\hat{H}$ problem.

$$\begin{aligned} E_0 < \langle \Psi' | \hat{H} | \Psi' \rangle &= \langle \Psi' | \hat{H}' | \Psi' \rangle + \langle \Psi' | \hat{H} - \hat{H}' | \Psi' \rangle \\ &= E'_0 + \int n(\vec{r}) \; [V_{\text{ext}}(\vec{r}) - V'_{\text{ext}}(\vec{r})] \, d\vec{r} \end{aligned} \tag{2.3}$$

where, E_0 and E_0' are the ground state energies of $\hat{H}$ and $\hat{H}'$, respectively. With the same procedure, taking Ψ as a trial function for $\hat{H}'$ problem.

$$\begin{aligned} E_0' < \langle\Psi|\hat{H}'|\Psi\rangle &= \langle\Psi|\hat{H}|\Psi\rangle + \langle\Psi|\hat{H}' - \hat{H}|\Psi\rangle \\ &= E_0 + \int n(\vec{r})\ [V_{\text{ext}}(\vec{r}) - V'_{\text{ext}}(\vec{r})]\, d\vec{r} \end{aligned} \tag{2.4}$$

By adding Eq. 2.3 and Eq. 2.4, we would obtain a contradiction,

$$E_0 + E_0' < E_0 + E_0'$$

Hence, there is no two different $V_{\text{ext}}(\vec{r})$ that give the same $n(\vec{r})$ for their ground state. On the other hand, the specific ground state density $n(\vec{r})$ only determines a specific external potential, $V_{\text{ext}}(\vec{r})$. by defining $n(\vec{r})$, all properties of the ground state also could be investigated. Now, the ground state energy could be written by,

$$E_0 = \int n_0(\vec{r})\, V_{\text{ne}}\, d\vec{r} + F_{\text{HK}}[n_0] \tag{2.5}$$

where, F_{HK} is *Hohenberg-Kohn functional*, which contains the kinetic energy $\hat{T}$ and electron repulsion energy $\hat{V}_{\text{ee}}$. However, this form is still unclear. This form should contains the effect of self-interaction correction, exchange, and Coulomb correlation. But, we still do not know explicitly yet. Maybe we also would be questioned, how we could be sure that density, which we are looking for, is the ground-state density. Through the second theorem, Hohenberg-Kohn answered this question.

Theorem II :

A universal functional that delivers the ground state energy of the system, delivers the lowest energy ***if and only if*** *the input density is the true ground state density.*

By variational principles, we could write

$$E_0 \leq E[\tilde{n}]$$

In the other words, for any trial density $\tilde{n}(\vec{r})$, the energy from Eq. 2.5 represents an upper bound to the true ground state energy E_0. Satisfy that $\tilde{n}(\vec{r})$ fulfil the necessary boundary condition, $\tilde{n}(\vec{r}) \geq 0$ and $\int \tilde{n}(\vec{r})\, d\vec{r} = N$, where N is number of electrons.

2.3.2 Kohn-Sham Approach

According to Hohenberg-Kohn theorem, W. Kohn and L. J. Sham [4] introduced a method which is to replace interaction electrons with non-interacting electrons which moving in an effective potential. The effective potential consists the external potential, the Coulomb interaction among electrons, and also its effect such as exchange and correlation interaction. In order to obtain the ground state density and energy, we require to solve the equations.

As mentioned earlier, in DFT, the main focus is electrons density. This quantity is expressed by

$$n(\vec{r}) = \sum_{i}^{N} |\Psi_i(\vec{r})|^2 \tag{2.6}$$

Through electrons density, number of electron in $d\tau$ (element of volume) is $n(\vec{r})\,d\tau$. Then, the total potential energy due to interaction between electrons and nucleus could be written as

$$E_{\text{ne}} = \int V_{\text{ext}}\, n(\vec{r})\, d\tau \tag{2.7}$$

For the Coulomb interaction energy of electron density, it could be expressed by

$$E_{\text{ee}} = \frac{1}{2} \int \frac{n(\vec{r}) n(\vec{r}\,')}{|\vec{r} - \vec{r}\,'|}\, d\tau d\tau' \tag{2.8}$$

where, $1/2$ is correction factor for *double counting*.

And for the total kinetic energy of electrons, it could be expressed by

$$\begin{aligned} T &= -\frac{1}{2} \sum_{i}^{N} \langle \Psi_i | \nabla^2 | \Psi_i \rangle \\ &= \frac{1}{2} \sum_{i}^{N} \int |\nabla \Psi_i(\vec{r})|^2\, d\tau \end{aligned} \tag{2.9}$$

Now, including external potential, Kohn-Sham express the energy for the ground state as

$$E_{\text{KS}} = T[n] + E_{\text{ne}}[n] + E_{\text{ee}}[n] + E_{\text{XC}}[n] \tag{2.10}$$

Exchange-correlation energy E_{XC} is compilation of all effects of exchange and correlation. When we know all the functionals E_{XC}, the exact ground state density

and energy could be obtained.

Consider that Khon-Sham energy problem is a minimization problem which related with density $n(\vec{r})$. Solution of this minimization problem could be obtained by using functional as following derivation,

$$\begin{aligned}
\frac{\delta E_{\mathrm{KS}}}{\delta \Psi_i^*(\vec{r})} &= \frac{\delta}{\delta \Psi_i^*(\vec{r})} \left\{ T[n] + E_{\mathrm{ne}}[n] + E_{\mathrm{ee}}[n] + E_{\mathrm{XC}}[n] \right\} \\
0 &= \frac{\delta T[n]}{\delta \Psi_i^*(\vec{r})} + \left\{ \frac{\delta E_{\mathrm{ne}}[n]}{\delta n(\vec{r})} + \frac{\delta E_{\mathrm{ee}}[n]}{\delta n(\vec{r})} + \frac{\delta E_{\mathrm{XC}}[n]}{\delta n(\vec{r})} \right\} \frac{\delta n(\vec{r})}{\delta \Psi_i^*(\vec{r})} \\
&\quad - \frac{\delta}{\delta n(\vec{r})} \left\{ \varepsilon \left(\int n(\vec{r}) d\tau - N \right) \right\} \frac{\delta n(\vec{r})}{\delta \Psi_i^*(\vec{r})}
\end{aligned} \tag{2.11}$$

where

$$\frac{\delta n(\vec{r})}{\delta \Psi_i^*(\vec{r})} = \Psi_i(\vec{r})$$

Substituting Eq. 2.9 to the first term of Eq. 2.11, we could obtain

$$\frac{\delta T[n]}{\delta \Psi_i^*(\vec{r})} = -\frac{1}{2} \nabla^2 \Psi_i(\vec{r}) \tag{2.12}$$

For the second term of Eq. 2.11, it could be rewritten becomes

$$\left\{ \frac{\delta E_{\mathrm{ne}}[n]}{\delta n(\vec{r})} + \frac{\delta E_{\mathrm{ee}}[n]}{\delta n(\vec{r})} + \frac{\delta E_{\mathrm{XC}}[n]}{\delta n(\vec{r})} \right\} \frac{\delta n(\vec{r})}{\delta \Psi_i^*(\vec{r})} = V_{\mathrm{eff}}(\vec{r})\ \Psi_i(\vec{r}) \tag{2.13}$$

where

$$V_{\mathrm{eff}}(\vec{r}) = V_{\mathrm{ext}}(\vec{r}) + V_{\mathrm{ee}}(\vec{r}) + V_{\mathrm{XC}}(\vec{r})$$

The last term of Eq. 2.11 contains Lagrangian multiplier ε, which is for handling the constraints to obtain the non-trivial solution. This term also could be rewritten as

$$\frac{\delta}{\delta n(\vec{r})}\left\{\varepsilon\left(\int n(\vec{r})d\tau - N\right)\right\}\frac{\delta n(\vec{r})}{\delta \Psi_i^*(\vec{r})} = \varepsilon_i\,\Psi_i(\vec{r}) \tag{2.14}$$

Substituting Eqs. 2.12, 2.13, and 2.14 to Eq. 2.11, we could obtain

$$\left(-\frac{1}{2}\nabla^2 + V_{\text{eff}}(\vec{r})\right)\Psi_i(\vec{r}) = \varepsilon_i\,\Psi_i(\vec{r}) \tag{2.15}$$

This equation is called as Kohn-Sham Equation, which is one of eigenvalue problem. By solving this equation, the wave function that we need to obtain density of electrons, should be obtained. Notice that the density of electrons is also required when we construct the Hamiltonian matrix of Kohn-Sham. This condition is similar with *pseudo-eigenvalue* problem in Hartree-Fock method. Therefore, we also could solve this problem using iteration scheme. First step is preparing trial initial density of electrons. Then, by solving Kohn-Sham equation, final density of electrons should be obtained. We have to compare the initial and final density. At the ground state density, initial and final density should be areed each other. This scheme is called self-consistent Kohn-Sham equation, which could be seen in Fig. 2.2.

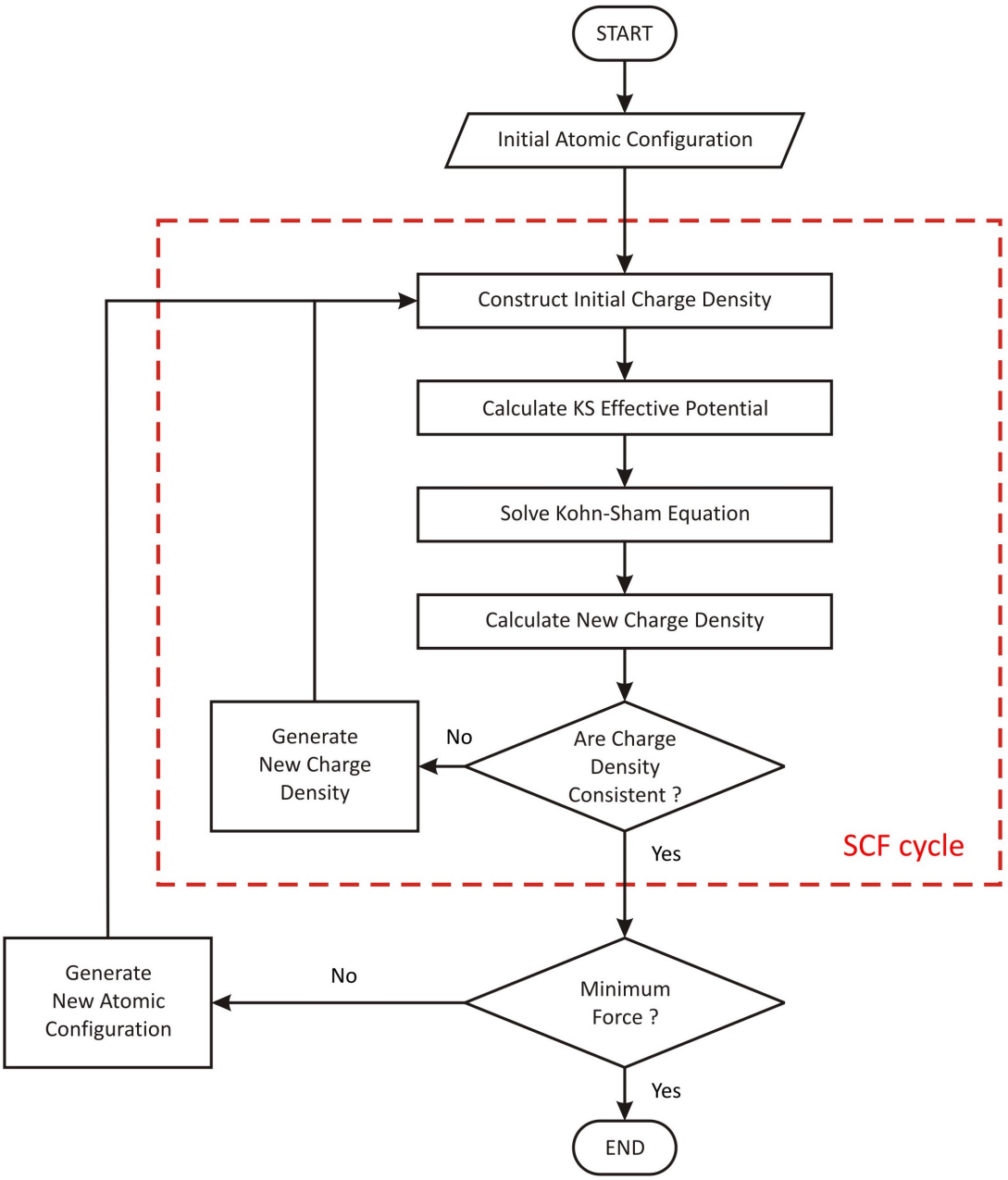

FIGURE 2.2: Self-Consistent Field cycle of Kohn-Sham equation (dash square) inside the structural optimization scheme.

2.3.3 Exchange-Correlation Energy

The exact ground state energy is difficult to be determined. Some assumption is required to approximate the exact ground state energy. Exchange-correlation term of Kohn-Sham equation (Eq. 2.10) gives big contribution to the approximation of exact ground state energy. The accuracy of the solution is limited to the approximation of exchange-correlation interactions. There are many method to approximate the exchange-correlation interactions, such as local density approximation (LDA), generalized gradient approximation (GGA), etc.

2.3.3.1 Local Density Approximation

In LDA, we assume that electrons density near $\vec{r}$ inside the element of volume $d\tau$ is homogeneous, exchange-correlation energy per electron $\epsilon_{\mathrm{xc}}(n(\vec{r}))$ is also homogeneous [5]. From this assumption, the exchange-correlation energy could be written by

$$E_{\mathrm{XC}}[n] = \int \epsilon_{\mathrm{xc}}(n(\vec{r}))\, n(\vec{r})\, d\tau$$

and

$$V_{\mathrm{XC}}[n] = \frac{\delta E_{\mathrm{XC}}[n]}{\delta n(\vec{r})} = \frac{\partial[\epsilon_{\mathrm{xc}}(n(\vec{r}))\, n(\vec{r})]}{\partial n(\vec{r})} = \epsilon_{\mathrm{xc}}(n(\vec{r})) + n(\vec{r})\frac{\partial \epsilon_{\mathrm{xc}}(n(\vec{r}))}{\partial n(\vec{r})}$$

2.3.3.2 Generalized Gradient Approximation

The density of electron is not always homogeneous as in LDA. An improvement could be made to handle any rapid change in the density. We could carry out the

expansion of electronic density in term of gradient or higher order derivatives. It can be simply written as

$$\frac{\delta E_{\mathrm{XC}}[n]}{\delta n(\vec{r})} = \epsilon_{\mathrm{xc}}(n(\vec{r})) + n(\vec{r})\frac{\partial \epsilon_{\mathrm{xc}}(n(\vec{r}))}{\partial n(\vec{r})} + n(\vec{r})\frac{\partial \epsilon_{\mathrm{xc}}(n(\vec{r}))}{\partial \nabla n(\vec{r})}\nabla \tag{2.16}$$

In the last term of Eq. 2.16, a term that proportional with the squared gradient of the density is introduced. Some studies [6, 7] considered the exchange-correlation potential up to fourth order. Moreover, recently, the general derivation of the exchange-correlation gradient expansion is expanded up to sixth order by using second order density response theory [7].

2.3.4 Plane-Wave Basis Set

Generally, is an approach of the solution of differential equation. By using plane waves, eigenfunction from the solution of the Kohn-Sham equation can be described. According to Bloch's Theorem [8], wave functions can be expressed by

$$\Psi_i(\vec{r}) = \exp(i\vec{k}\cdot\vec{r})\ f_i(\vec{r}) \tag{2.17}$$

where, $f_i(\vec{r})$ is periodic in space with the same periodicity with the cell, which can be expanded into a set of plane waves as below

$$f_i(\vec{r}) = \sum_{\vec{G}} c_{i,\vec{G}}\ \exp(i\vec{G}\cdot\vec{r}) \tag{2.18}$$

Inserting Eq. 2.18 to Eq. 2.17, the wave function can be written as

$$\Psi_i(\vec{r}) = \sum_{\vec{G}} c_{i,\vec{G}+\vec{k}} \exp(i(\vec{G}+\vec{k}) \cdot \vec{r}) \tag{2.19}$$

According to Eqs. 2.6 and 2.19, notice that the density of electron can be expressed as superposition of plane waves [9]. In the term of reciprocal space $\vec{k}$, the Kohn-Sham equation (Eq. 2.15) can be rewritten as below

$$\sum_{\vec{G}'} = \left[\frac{1}{2}|\vec{k}+\vec{G}|^2 \, \delta_{\vec{G},\vec{G}'} + V_{\text{eff}}(\vec{G}-\vec{G}')\right] c_{i,\vec{k}+\vec{G}} = \varepsilon_i \, c_{i,\vec{k}+\vec{G}} \tag{2.20}$$

Kinetic energy in Eq. 2.20 has diagonal form, and the potential is given in the form of Fourier transformation. Solution of Eq. 2.20 can be obtained by using matrix diagonalization. Size of the Hamiltonian matrix is depending on kinetic energy *cut off* E_{cutoff}. A finite plane wave set is obtained by taking all plane waves up to a given kinetic energy *cut off*. Error of total energy value can be appear due to this limitation. However, we can reduce the error by increasing the kinetic energy *cut off* until the total energy is already convergent.

2.3.5 Pseudopotential

Electronic structure of materials can be distinguish into core electron and valence electron. Valence electron can moving freely relative to core electron, which is locate near the nuclei so that its movement is limited. As mentioned earlier, based on Bloch's theorem, electronic wave function can describe into discontinuous plane-wave basis set. However, it difficult to describe the wave function of

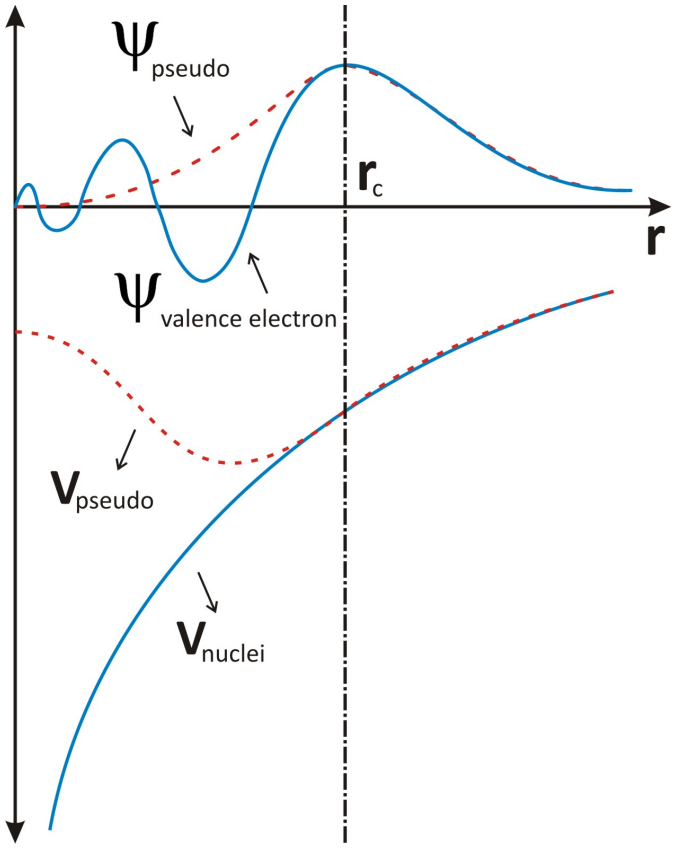

FIGURE 2.3: Illustration of valence electron wave function and nuclei potential (complete line) and pseudo wave function and pseudopotential (dash line).

electrons near nuclei. Large number of plane wave are needed to expand the wave function of core electrons due to rapid oscillation near the nuclei. By constructing a pseudopotential, we can reduce the number of plane wave.

Generally, in order to investigate the properties of materials, the valence electron has greater influence than core electron. The approximation is performed by replacing core electrons and strong nuclei potential with weaker pseudopotential and pseudo wave functions. As illustrated in Fig. 2.3, pseudopotential and pseudo wave function should be same with nuclei potential and valence electron wave function when $r \geq r_c$. Notice that near the nuclei, we still have tightly bonded core electrons. However, orthogonality and exclusion principle must be fulfilled by

both valence electron and core electron. There are two kinds of pseudopotential, norm-conserving pseudopotential and ultrasoft pseudopotential.

2.3.5.1 Norm-Conserving Pseudopotential

Constructing the pseudopotential is an inverse problem. The pseudo wave function should: beyond some distance decays exactly as the all electron wave functions. The pseudo wave function is also an eigenstate of pseudo Hamiltonian, which has the same eigenvalue as all electron wave functions. To obtain the pseudopotential, the radial Schrödinger equation is inverted for such pseudo wave function:

$$\left\{-\frac{d^2}{dr^2}+\frac{l(l+1)}{2r^2}+v(r)\right\} r\,\Psi = \epsilon\, r\,\Psi$$

To construct the norm-conserving pseudopotential [10], we need to fulfil some important conditions, such as

(i) For a chosen atomic configuration, all-electron and pseudo valence eigenvalues are same.

$$\epsilon_i^{\mathrm{AE}} = \epsilon_i^{\mathrm{PS}}$$

(ii) All-electron and pseudo valence wave functions agree in the outside core region.

$$\Psi_i^{\mathrm{AE}}(r) = \Psi_i^{\mathrm{PS}}(r), \quad r \geq R_{\mathrm{c}}$$

(iii) At the core radius R_c, logarithmic derivatives of the all-electron must be same with logarithmic derivatives of pseudo valence.

$$\frac{d}{dr} \ln \Psi_i^{\mathrm{AE}}(r) = \frac{d}{dr} \ln \Psi_i^{\mathrm{PS}}(r)$$

(iv) Inside core radius ($r < R_c$), the total charge for each wave function must be same (norm-conservation).

$$\int_0^{R_c} |\Psi_i^{\mathrm{AE}}(r)|^2 = \int_0^{R_c} |\Psi_i^{\mathrm{PS}}(r)|^2$$

(v) Implying point (iv), the first energy derivative of the logarithmic derivatives of all-electron and pseudo valence must be same for $r \geq R_c$.

However, the norm-conserving pseudopotential still have limitations, which are still "hard" and required a large plane-wave basis sets ($E_{\mathrm{cutoff}} = 70\,\mathrm{Ry}$) for:

- First row elements, in particular N, O , F
- Transition metals, in particular the 3d row: Cr, Mn, Fe, Co, Ni, etc.

Even if just one atom is "hard", a high cutoff is required. This translates into large CPU and RAM requirements.

2.3.5.2 Ultrasoft Pseudopotential

In 1190, Vanderbilt introduced a pseudopotential, which is smoother and highly transferable pseudopotential called ultrasoft pseudopotential [11]. In this approach, the pseudo wave functions are required to be equal to the all electron wave functions outside R_c, as with norm-conserving pseudopotential, but inside the core radius they are allowed to be as soft as possible.

In this kind of pseudopotential scheme, the Kohn-Sham total energy (Eq. 2.11) including a non-local pseudopotential V_{non} which is described by the wave function ϕ_i, is given by

$$\begin{aligned} E_{\text{tot}} &= \sum_i \langle \phi_i | -\nabla^2 + V_{\text{non}} | \phi_i \rangle \\ &+ \frac{1}{2} \int \frac{n(\vec{r}) n(\vec{r}\,')}{|\vec{r} - \vec{r}\,'|} \, d\tau d\tau' \\ &+ \int V_{\text{ext}} \, n(\vec{r}) \, d\tau + E_{\text{XC}} \end{aligned} \tag{2.21}$$

The non-local pseudopotential V_{non} in Eq. 2.21 is given by

$$V_{\text{non}} = \sum_{nm} D^0_{nm} \ |\beta_n\rangle \langle \beta_m|$$

where β is a set of local wave functions to be determined.

The electron density $n(\vec{r})$ in Eq. 2.21 is given by

$$n(\vec{r}) = \sum_i \left[|\phi_i(\vec{r})|^2 + \sum_{nm} Q_{nm}(\vec{r}) \, \langle \phi_i | \beta_n \rangle \, \langle \beta_m | \phi_i \rangle \right]$$

where Q_{nm} is a core augmentation charge, which is expressed by

$$Q_{nm}(\vec{r}) = \Psi_n^{\mathrm{AE}*}(\vec{r})\ \Psi_m^{\mathrm{AE}}(\vec{r}) - \Psi_n^{\mathrm{US}*}(\vec{r})\ \Psi_m^{\mathrm{US}}(\vec{r})$$

The relaxation of the norm-conserving condition is achieved by introducing a generalized orthonormal condition

$$\left\langle \phi_i | \hat{S} | \phi_j \right\rangle = \delta_{ij} \tag{2.22}$$

where, $\hat{S}$ is a Hermitian overlap operator, which is given by

$$\hat{S} = \hat{I} + \sum_{nm} q_{nm}\ \ |\beta_n\rangle \langle \beta_m|$$

with $q_{nm} = \int Q_{nm}(\vec{r}) d\vec{r}$. Under condition (Eq. 2.22), the ground state wave functions ϕ_i are those which minimize the total energy (Eq. 2.21),

$$\frac{\delta E_{\mathrm{tot}}}{\delta \phi_i^*(\vec{r})} = \varepsilon_i\ \hat{S}\ \phi_i(\vec{r})$$

where ε have been introduced as Lagrange multipliers. Due to the fact that the augmentation part of the charge density depends on the wave functions, additional terms appear in the Kohn-Sham equations from the density-dependent terms in the total energy (Eq. 2.21).

$$\frac{\delta n(\vec{r}\,')}{\delta \phi_i^*(\vec{r})} = \phi_i(\vec{r}\,')\delta(\vec{r}\,' - \vec{r}) + \sum_{nm} Q_{nm}(\vec{r}\,')\beta_n(\vec{r})\ \langle \beta_m | \phi_i \rangle \tag{2.23}$$

As an example, by using Eq. 2.23 the exchange and correlation energy can be written as

$$\begin{aligned}\frac{\delta E_{\mathrm{XC}}[n]}{\delta \phi_i^*(\vec{r})} &= \int \frac{\delta E_{\mathrm{XC}}[n]}{\delta n(\vec{r}\,')} \frac{\delta n(\vec{r}\,')}{\delta \phi_i^*(\vec{r})} \\ &= \mu_{\mathrm{xc}}(\vec{r})\phi_i(\vec{r}) + \sum_{nm} \beta_n(\vec{r}) \langle \beta_m | \phi_i \rangle \int \mu_{\mathrm{xc}}(\vec{r}\,') Q_{nm}(\vec{r}\,') \end{aligned} \tag{2.24}$$

where

$$\mu_{\mathrm{xc}}(\vec{r}) = \frac{\delta E_{\mathrm{XC}}[n]}{\delta n(\vec{r})}$$

The other terms can be calculated similarly.

Then, the Schrödinger eguation can be written as

$$\hat{H} \ |\phi_i\rangle = \varepsilon_i \, \hat{S} \ |\phi_i\rangle \tag{2.25}$$

with

$$\hat{H} = -\nabla^2 + V_{\mathrm{eff}} + \sum_{nm} D_{nm} \ |\beta_n\rangle \langle \beta_m|$$

Here, V_{eff} is screened effective local potential, which is given by

$$V_{\mathrm{eff}}(\vec{r}) = \frac{\delta E_{\mathrm{tot}}[n]}{\delta n(\vec{r})} = V_{\mathrm{ext}}(\vec{r}) + \int \frac{n(\vec{r}\,')}{|\vec{r} - \vec{r}\,'|} + \mu_{\mathrm{xc}}(\vec{r})$$

The eigenvalue problem, which is shown in Eq. 2.25, can be solved iteratively. First, we need to construct the initial ultrasoft pseudo wave function ϕ_i. Then, compute the density $n(\vec{r})$. By using $n(\vec{r})$, we can calculate the potentials to compute E_{tot}. Finally, we have to solve Eq. 2.25 using these estimated values.

Before that, we need to construct β. The solution can be obtained when the initial and final wave function have been consistent.

References

[1] L. H. Thomas, "The calculation of atomic fields," *Mathematical Proceedings of the Cambridge Philosophical Society*, vol. 23, p. 542, 1927.

[2] E. Fermi, "Un metodo statistico per la determinazione di alcune priorieta dell'atome," *Rend. Accad. Naz. Lincei*, vol. 6, p. 602, 1927.

[3] P. Hohenberg and W. Kohn, "Inhomogeneous electron gas," *Phys. Rev.*, vol. 136, p. B864, 1964.

[4] W. Kohn and L. J. Sham, "Self-consistent equations including exchange correlation effects," *Phys. Rev.*, vol. 140, p. A1133, 1965.

[5] R. M. Martin, *Electronic Structure Basic Theory and Practical Methods*. Cambridge University Press, 2004.

[6] J. P. Perdew and K. Burke, "Comparison shopping for a gradient-corrected density functional," *Int. J. Quant. Chem*, vol. 57, p. 309, 1996.

[7] P. S. Svendsen and U. von Barth, "Gradient expansion of the exchange energy from second-order density response theory," *Phys. Rev. B*, vol. 54, p. 17402, 1996.

[8] C. Kittel, *Introduction to solid state physics, sixth edition*. John Wiley - Sons Inc, 1986.

[9] M. C. Payne, M. P. Teter, D. C. Allan, T. A. Arias, and J. D. Joannopoulos, "Iterative minimization techniques for *Ab initio* total-energy calculations: Molecular dynamics and conjugate gradients," *Rev. Mod. Phys.*, vol. 64, p. 1045, 1992.

[10] D. R. Hamann, M. Schlüter, and C. Chiang, "Norm-conserving pseudopotentials," *Phys. Rev. Lett.*, vol. 43, p. 1494, 1979.

[11] D. Vanderbilt, "Soft self-consistent pseudopotentials in a generalized eigenvalue formalism," *Phys. Rev. B*, vol. 41, p. 7892, 1990.

Chapter 3

Hybrid Image Potential States in Naphthalene Overlayer on Graphene

3.1 Background

The emergence of image potential states (IPSs) is a universal nature of metal surfaces, characterized by a set of unoccupied states quantized to a Rydberg series analogous to the hydrogen atom [1, 2]. IPSs exist even on graphene, an atomically thin two-dimensional material, where the IPSs on the two surfaces hybridize to form a double Rydberg series corresponding to symmetric and antisymmetric states with respect to the graphene sheet [3, 4]. More exotic IPSs appear on curved graphene, typical examples of which are tubular IPSs extended around carbon nanotubes [5] and superatom molecular orbitals of C_{60} fullerene [6].

The hybridization of these IPSs results in the interlayer states with a nearly-free-electron feature in a variety of graphitic materials such as graphite [3], multi-walled [7, 8] or bundles [9, 10] of carbon nanotubes, fullerite solids [11, 12] and carbon nanopeapods [13]. In particular, the interlayer states in graphite are believed to be crucial for the superconductivity of graphite-intercalation compounds [14].

In this study, I extend the concept of the IPS-derived interlayer states to molecular adsorption on solid surfaces. From an applicational point of view, it is of particular importance to understand unoccupied states including IPSs for improving the performance of molecular-based electronic devices such as organic light emitting diodes. Naphthalene on highly oriented pyrolytic graphite (HOPG) is a prototype system of aromatic molecules physisorbed on a solid surface, and has been investigated intensively thus far [15, 16, 17, 18, 19]. Recent scanning tunneling microscopy (STM) experiments have revealed that naphthalene molecules form a well-ordered superstructure [Fig. 3.1(a-d)] with a tilted molecular adsorption geometry [Fig. 3.1(e)] with periodicity of $(2\sqrt{3} \times 2\sqrt{3})$ R30° with respect to the unit cell of graphene [17]. More importantly, the results of angle-resolved two-photon photoemission (2PPE) spectroscopy suggest that the lowest IPS (LIPS) behaves almost as a free electron despite the presence of the naphthalene overlayer [18]. This is explained by assuming that the molecular overlayer is a dielectric medium with uniform permittivity and only shifts the Rydberg series with the effective mass m^* unchanged from the electronic mass m_e [1]. However, the well-known Kronig-Penny theory [20] suggests an increase in m^* if naphthalene acts as a periodic potential for the IPSs.

To develop a coherent picture of the IPSs at organic-solid interfaces, I here perform first principles calculations of a simplified model composed of naphthalene on graphene with the van der Waals density functional (vdW-DF) method [21, 22]. My results predict that the interaction between naphthalene molecules does not onlystabilize the naphthalene superstructure on graphene, but also induces extended states analogous to IPSs on the naphthalene overlayer. The IPS-like states

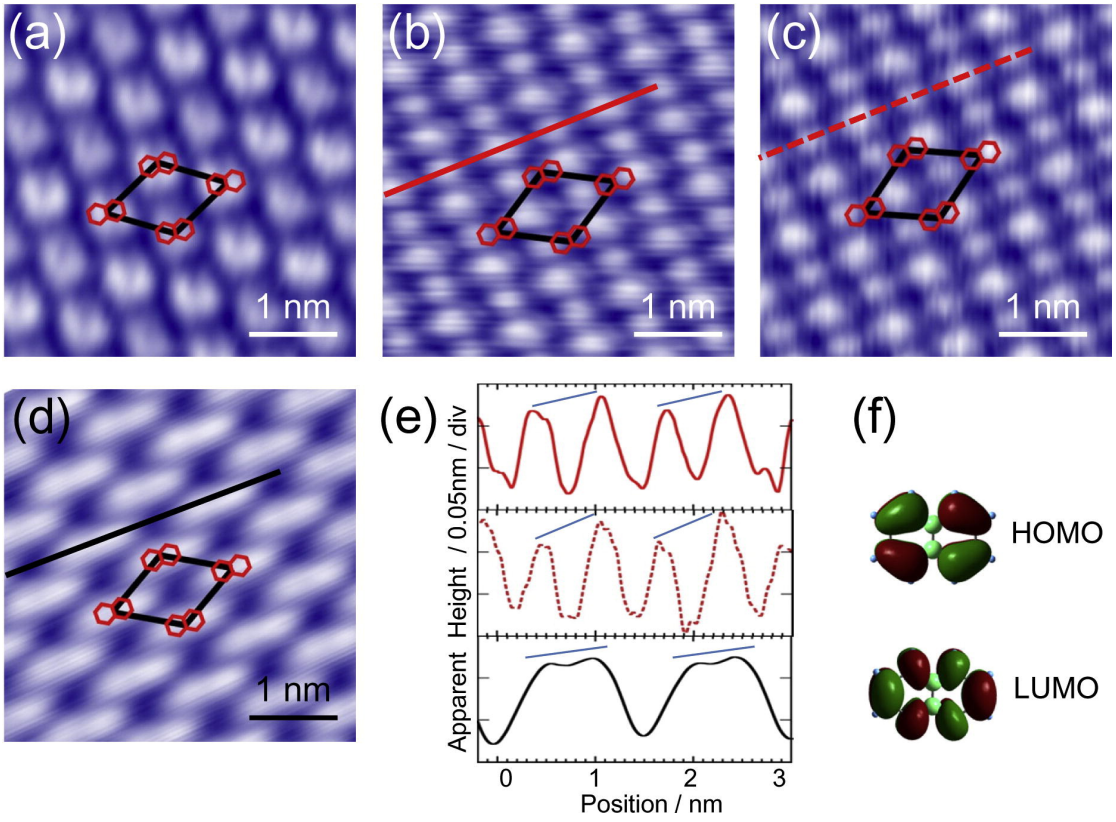

FIGURE 3.1: (a) Occupied state image obtained with a sharp tip. Carbon frameworks of molecules and a unit cell are shown in the image as a guide to the eye. 4.0×4.0 nm^2, $V_s = -2.79$ V, $I_t = 0.10$ nA. (b) Another high resolution occupied state image. 4.0×4.0 nm^2, $V_s = -3.10$ V, $I_t = 0.15$ nA. (c) STM image taken along the vertical scan direction (from top to bottom) at the same area as (b). 4.0×4.0 nm^2, $V_s = -3.10$ V, $I_t = 0.15$ nA. (d) Unoccupied state image of (b). 4.0×4.0 nm^2, $V_s = 3.00$ V, $I_t = 0.08$ nA. (e) Spatial line profiles along the lines in (b)–(d). Upper panel represents the profiles along the red line in (b), middle panel, along the red-dashed-line in (c) and lower panel, along the black line in (d). (f) DFT calculations of the HOMO and LUMO for a free naphthalene molecule, performed with the B3LYP method and the LANL2DZ basis set. Reprinted from Ref. 17 with permission from Elsevier.

hybridize with the graphene IPSs and play an essential role in the formation of peculiar interface states with anisotropic m^* in naphthalene on graphene. Here I stress that low-lying IPSs are well-described by vdW-DF owing to the inclusion of nonlocal correlation [23].

3.2 Computational Details

The calculations are carried out using the STATE code [24] with the norm-conserving pseudopotentials [25]. The plane wave basis set is used to expand wave functions (charge density) with cutoff energy of 64 Ry (400 Ry). To investigate the coverage dependence of naphthalene on graphene, I adopt three unit cells of graphene with the periodicity of $(2\sqrt{3} \times 2\sqrt{3})$, $(3\sqrt{3} \times 3\sqrt{3})$ and $(4\sqrt{3} \times 4\sqrt{3})$. Correspondingly, $6 \times 6 \times 1$, $4 \times 4 \times 1$ and $3 \times 3 \times 1$ k-points are sampled in the Brillouin zone, respectively. The dispersion correction is included through the self-consistent [26, 27, 28, 29] vdW-DF method [21, 22] with the rev-vdW-DF2 functional [30, 31, 32, 33, 34, 35]. The lattice constant of graphene obtained with

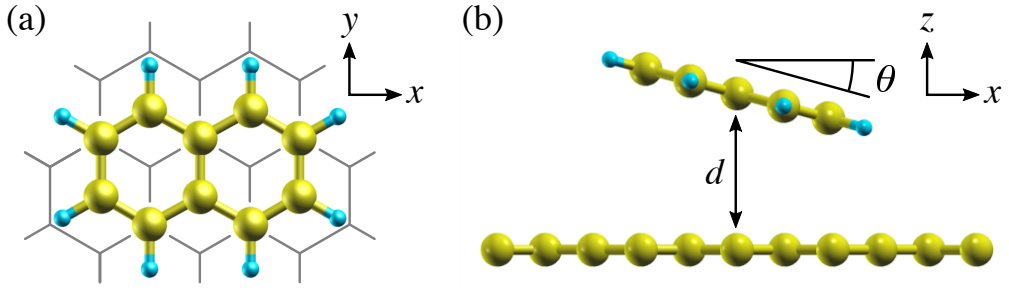

FIGURE 3.2: Schematic views of naphthalene adsorption on graphene. In the top view (a), graphene is represented with its skeleton. In the front view (b), θ and d denote the tilt angle and distance, respectively, between naphthalene and graphene.

the functional is 2.46 Å in good agreement with experiments [36]. As a reference system, the geometry of an isolated naphthalene molecule is relaxeduntil the atomic forces fall below 0.08 nN (5.14×10^{-2} eV/Å). A naphthalene molecule thus obtained is AB-stacked on each unit cell of graphene as shown in Fig. 3.2. To suppress unphysical interactions between the neighboring cells, a vacuum layer of $\simeq$ 26 Å is considered. The constant-current STM image of the system is simulated with a density threshold of 6.76×10^{-5} Å^{-3} based on the Tersoff-Hamann method [37, 38].

3.3 Tilted naphthalene on graphene

To see the role of intermolecular interaction, I first examine the adsorption structure of naphthalene on graphene in three coverage regimes corresponding to the unit cells mentioned above. Stable adsorption structures are explored by varying the distance d and tilt angle θ between naphthalene and graphene (see Fig. 3.2) with each structure unchanged. I here ignore the tilting along the short axis of naphthalene, since its effect turns out much smaller than along the long axis. The interaction energy between naphthalene and graphene is calculated as

$$E_{\mathrm{int}} = E_{\mathrm{nap/GR}} - E_{\mathrm{nap}} - E_{\mathrm{GR}}, \tag{3.1}$$

where $E_{\mathrm{nap/GR}}, E_{\mathrm{nap}}$ and E_{GR} are the total energies of naphthalene on graphene, the isolated naphthalene molecule and pristine graphene, respectively. In Fig. 3.3(a–c), the interaction energy (3.1) is plotted as a function of naphthalene-graphene

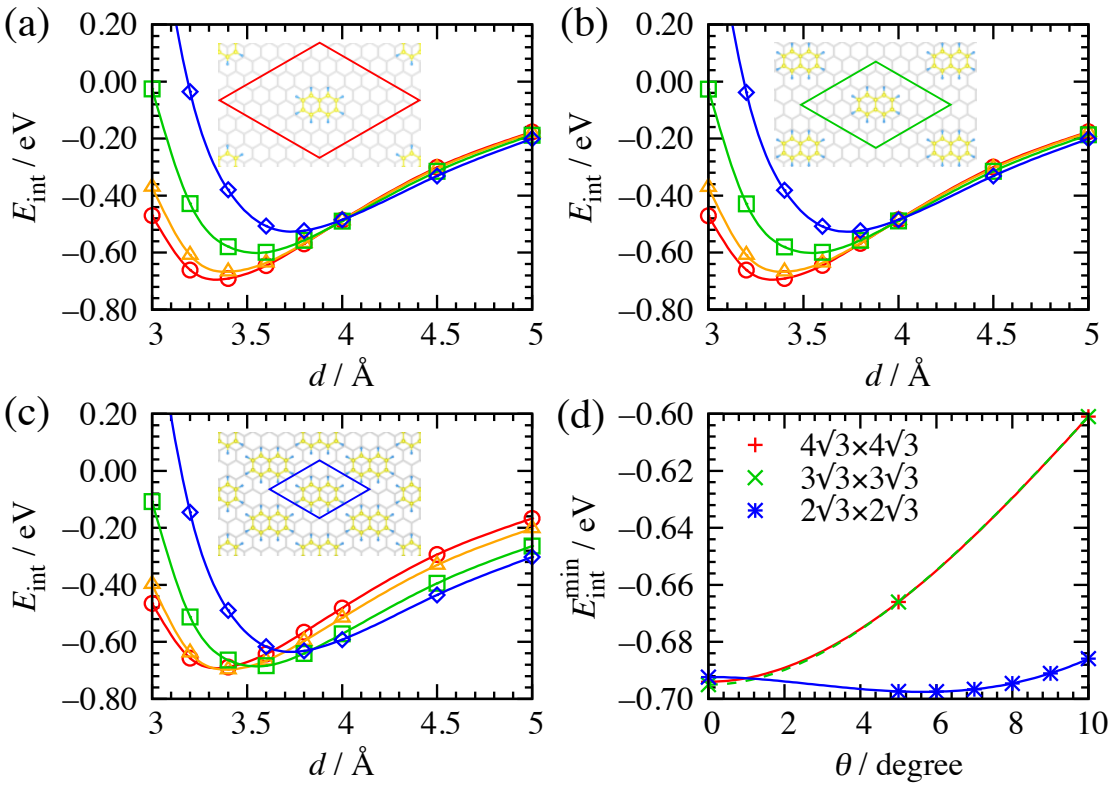

FIGURE 3.3: Interaction energy between naphthalene and graphene. In panels (a), (b) and (c), energy profiles at several tilt angles are plotted as functions of naphthalene-graphene distance for the $(4\sqrt{3}\times 4\sqrt{3})$, $(3\sqrt{3}\times 3\sqrt{3})$ and $(2\sqrt{3}\times 2\sqrt{3})$ unit cells, respectively. Circles ($\circ$), triangles ($\triangle$), squares ($\square$) and diamonds ($\diamond$) correspond to tilt angles $\theta = 0°, 5°, 10°$ and $15°$, respectively. In panel (d), the energy minima extracted from panels (a)–(c) are plotted as a function of the tilt angle.

distance for several tilt angles. The minimal energy $E_{\rm int}^{\rm min}$ is extracted from each energy profile by cubic-spline fitting and plotted as a function of θ as shown in Fig. 3.3(d). For the $(3\sqrt{3}\times 3\sqrt{3})$ and $(4\sqrt{3}\times 4\sqrt{3})$ unit cells, $E_{\rm int}^{\rm min}$ has a unique minimum at $\theta = 0°$, i.e. naphthalene tends to be parallel to graphene at low coverage, which is consistent with the assumption adopted in the previous calculations with large unit cells [39, 33]. On the other hand, the dispersion force between the molecules works attractively for the $(2\sqrt{3}\times 2\sqrt{3})$ unit cell, while the parallel geometry is destabilized by Pauli repulsion. As a result, $E_{\rm int}^{\rm min}$ displays lower minima at $\theta \simeq \pm 6°$, which is roughly 5 meV more stable than at $\theta = 0°$, indicating that

the molecules are stabilized by forming a $(2\sqrt{3} \times 2\sqrt{3})$ superstructure with the tilted adsorption geometry. The formation of the naphthalene superstructure is in good agreement with the STM results on HOPG surfaces [17]. It is confirmed that the tilted adsorption structure is insensitive to addition of another graphene layer, or to a perpendicular electric field applied with the effective screening medium method [40, 41].

3.4 Hybrid image potential states

I next investigate the electronic structure of naphthalene on graphene with a special emphasis on the unoccupied states. To this end, I fully relax the stable structure obtained for the $(2\sqrt{3} \times 2\sqrt{3})$ unit cell, although its influence on the adsorption geometry and energy turns out to be negligibly small. I then calculate the energy bands as shown in Fig. 3.4(a), where the solid (red) and dashed (blue) curves correspond to the band structures along paths $\Gamma M_1 K_1 \Gamma$ and $\Gamma M_2 K_2 \Gamma$, respectively, in the folded Brillouin zone (see the inset). The difference between the two band structures reflects the fact that the six-fold symmetry of pristine graphene is broken by the adsorption of naphthalene. For clues about the IPSs of the adsorbed system, I here take the LIPS of pristine graphene, the band bottom of which is 2.84 eV from the Fermi level at the Γ point (see Fig. A.1).[1] Interestingly, a similar quasi-parabolic band can also be found in Fig. 3.4(a), where the band bottom slightly shifts downwards to 2.79 eV. Apparently, the latter is

[1] Recently, Hamada *et al.* [23] reported that vdW-DF reproduces the low-lying IPS levels of graphene obtained using the LDA+image potential correction [4].

consistent with the 2PPE results of naphthalene on HOPG [18], in which the band dispersion of the LIPS seems unaffected by the molecular adsorption. However, the large amplitudes of the graphene LIPS near the naphthalene adsorption height $d \simeq 3.44$ Å suggest possible hybridization with the molecular orbitals (MOs) of naphthalene.

In order to gain insight into the interaction between the graphene LIPS and the naphthalene MOs, I inspect the wave functions of unoccupied states labeled U_1–U_4 at the Γ point, as shown in the lower panels of Fig. 3.4. From the comparison with the naphthalene MOs, U_1 (U_3) can be assigned to a state mainly derived from the LUMO+1 (LUMO+2) of naphthalene.[2] Note that the positive (negative) dispersions near Γ result from the overlap between adjacent wave functions in an in- (out-of-) phase configuration. In sharp contrast to the localized MO-like states, the wave functions of U_2 and U_4 are extended both around naphthalene and graphene. Thus these states are no longer simple graphene IPSs, despite the presence of the quasi-parabolic dispersions. Rather, the extended behavior of U_2 recalls interlayer states realized between graphene LIPSs [3], suggesting that the naphthalene overlayer mimics graphene in the formation of U_2.

To identify the origin of the peculiar nature of U_2, I calculate the energy bands of the naphthalene monolayer without graphene as shown in Fig. 3.4(b). Here the geometry of naphthalene is fixed to the adsorption structure in the $(2\sqrt{3} \times 2\sqrt{3})$ unit cell. One readily notices that there appear quasi-parabolic dispersions with band minima of 2.77 and 3.80 eV at Γ, which are analogous to the two lowest

[2]DFT in general underestimates the LUMO level, while it also lacks dynamical surface polarization [42, 43, 44]. This cancellation enables one to describe the LUMO level of molecules on solid surfaces reasonably well.

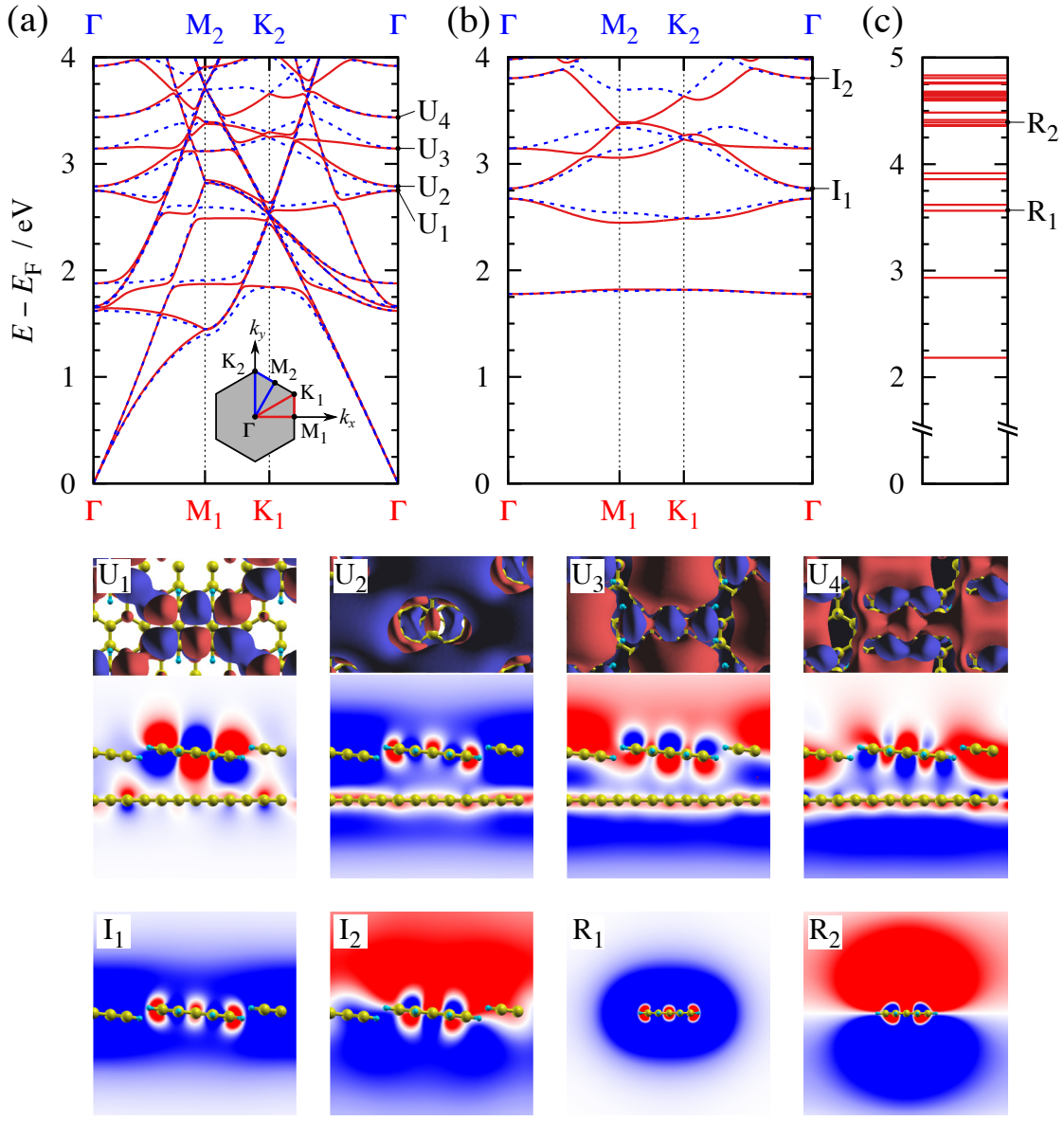

FIGURE 3.4: Band structures above the Fermi level (E_F) of (a) naphthalene on graphene and (b) the naphthalene monolayer calculated with the $(2\sqrt{3} \times 2\sqrt{3})$ unit cell. The energy levels of the isolated naphthalene molecule is shown in panel (c) for comparison. In panels (b) and (c), the origin of energy is determined so that the vacuum level coincides with that in the adsorbed system (a). The solid (red) and dashed (blue) curves denote the energy dispersions along paths $\Gamma M_1 K_1 \Gamma$ and $\Gamma M_2 K_2 \Gamma$, respectively, in the folded Brillouin zone shown in the inset of panel (a). In the lower panels, the top (front) views of the wave functions for several unoccupied states are represented by isosurfaces (color plots). We show only the real parts of the wave functions, where the red and blue colors correspond to e.g. positive and negative amplitudes, respectively.

IPSs of graphene. The similarity becomes even clearer from the wave functions of the IPS-like state labeled I_1 (I_2) in Fig. 3.4(b), which is roughly symmetric (anti-symmetric) with respect to the naphthalene layer, corresponding to the LIPS of graphene with even (odd) parity [4]. Unlike the isotropic effective mass of the graphene IPSs $m^*/m_e = 1.02$, the IPS-like states of the naphthalene layer exhibit a strong anisotropy in m^* as shown in Table 3.1. For example, I_1 behaves like the graphene LIPS along the long axis of naphthalene, while it gets heavier along the short axis. I_2 also shows a similar anisotropy but it is nearly twice heavier than I_1. As the intermolecular separation increases, the IPS-like states lose the energy dispersions and convert to the Rydberg states [45] of the isolated naphthalene molecule labeled R_1 and R_2 in Fig. 3.4(c). From this, it is clear that the odd (even) parity of I_1 (I_2) originates from the *s*- (*p*-) like orbital of R_1 (R_2).

I also examine how the wave functions evolve as the naphthalene layer approaches graphene. To describe one by one the formation of the states, I show in Fig. 3.5 the energy bands and wave functions at several distances between naphthalene and graphene. It should be noted that labels U_1, U_2, U_3 and U_4 at each distance do not exactly denote the same states as those obtained at the equilibrium distance $d = 3.44$ Å, because these states are in general hybridized with each other as naphthalene approaches graphene.

At $d = 9.79$ Å, the interaction between naphthalene and graphene is still weak, and thus IPS-like states can be easily distinguished from MO-like states in terms of the wave functions as shown in Fig. 3.5(a). Here, it is clear that U_1 (U_3) is analogous to LUMO+1 (LUMO+2) as mentioned above. Namely, U_2 (U_4) displays a weak

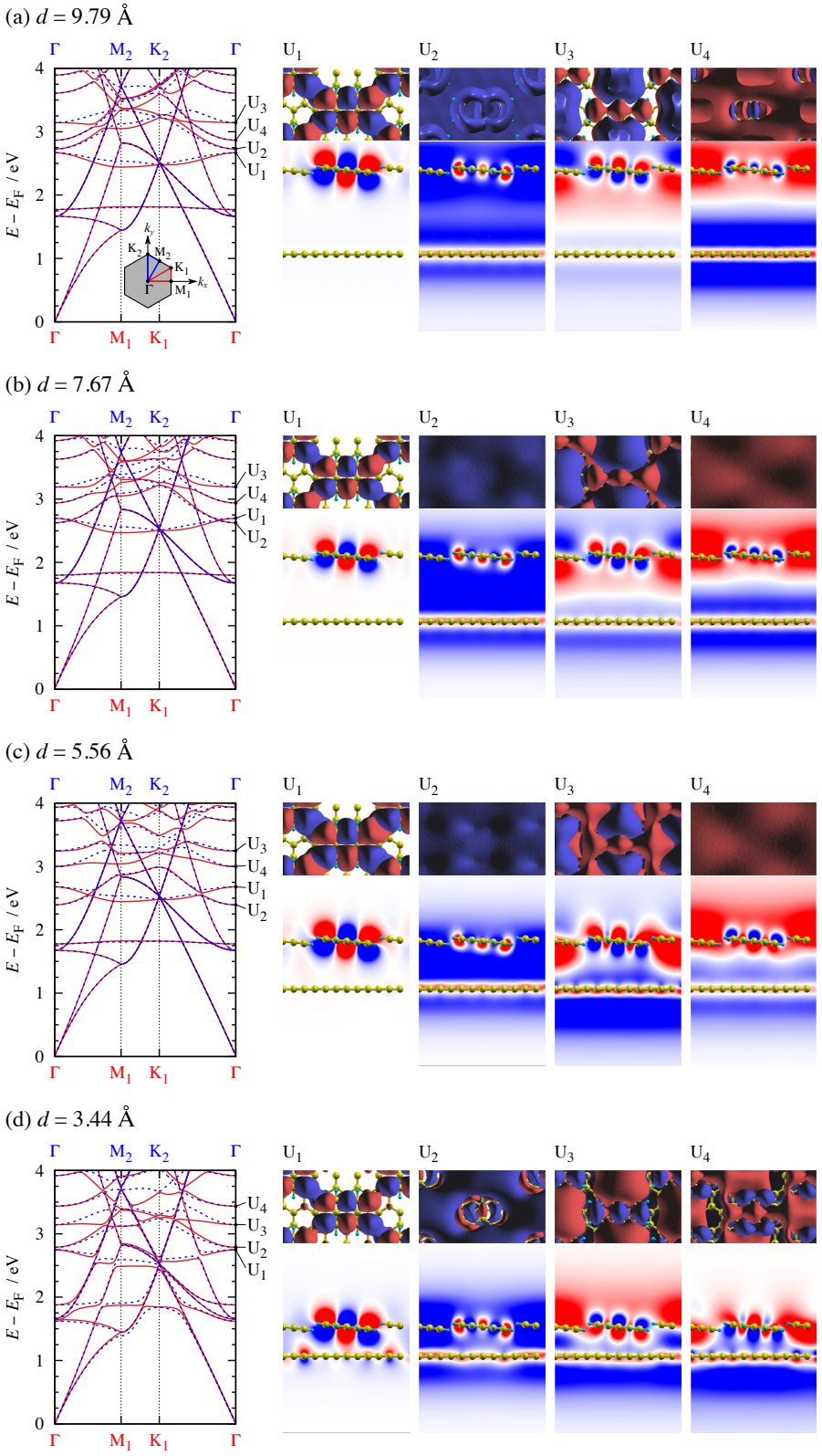

FIGURE 3.5: The band structures and wave functions of unoccupied states at several distances d between naphthalene and graphene. Note that labels U_1, U_2, U_3 and U_4 at each distance do not exactly denote the same states as those obtained at the equilibrium distance $d = 3.44$ Å.

bonding (anti-bonding) hybridization between the LIPS of graphene (1^+) and the IPS-like state of naphthalene (I_1). Such hybridization between IPSs (hybrid IPSs) is also reflected in the band structure, where one can find two parabolic bands near 2.8 eV at Γ, which are quite similar to each other. In addition, one also notices the parabolic band at 3.6 (3.9) eV, which corresponds to the bonding (anti-bonding) state between 1^- and I_2. As naphthalene approaches graphene, U_2 is initially stabilized by the bonding hybridization between the IPSs and becomes more stable than U_1 [see Figs. 3.5(b) and (c)]. However, when the naphthalene-graphene distance is further decreased, the stabilization is canceled out by Pauli repulsion, and as a result U_2 behaves like the graphene LIPS at $d = 3.44$ Å as shown in Fig. 3.5(d), although U_2 has a small anisotropy in the effective mass reflecting the molecular structure of naphthalene. Note that the band dispersions and wave functions of U_1 and U_2 remain almost unchanged during this process. The small hybridization between them is due to the fact that the wave function of U_1 (U_2) is roughly symmetric (anti-symmetric) with respect to the naphthalene (graphene) plane.

On the other hand, both U_3 and U_4 have roughly anti-symmetric wave functions at $d = 9.79$ Å, which leads to strong hybridization between them as U_4 is destabilized monotonically. Indeed, U_3 displays a slightly IPS-like character around graphene even at $d = 7.67$ Å as shown in Fig. 3.5(b). This tendency is increased at $d = 5.56$ Å [Fig. 3.5(c)], where U_3 has larger amplitude than U_4 near graphene, which indicates that U_3 and U_4 cannot be clearly assigned to the LUMO+2-like state or the anti-bonding hybrid IPS. This picture is also supported by the band

TABLE 3.1: Effective masses of the IPS-like states in naphthalene on graphene and the naphthalene monolayer estimated from Fig. 3.4. The results are obtained in four directions from the Γ point in the Brillouin zone.

	$\Gamma \rightarrow M_1$	$\Gamma \rightarrow K_1$	$\Gamma \rightarrow M_2$	$\Gamma \rightarrow K_2$
U_2	1.00	1.07	1.27	1.43
U_4	3.13	2.70	2.10	1.89
I_1	0.98	1.05	1.23	1.36
I_2	1.90	1.97	2.13	2.23

structure, where the dispersions of U_3 and U_4 show intermediate behaviors between the graphene LIPS and the naphthalene MO. At the equilibrium distance $d = 3.44$ Å [Fig. 3.5(d)], however, the MO- (IPS-) like dispersion of U_3 (U_4) as in Fig. 3.5(a) is recovered, although the corresponding wave functions are more complicated than in Fig. 3.5(a) as a result of the hybridization. From Table 3.1, one notices that the hybrid IPS U_2 retains the anisotropic m^* of I_1 even after the hybridization. For the hybrid IPS U_4, the effective mass becomes roughly twice heavier than the graphene LIPS and the IPS-like states of naphthalene. More importantly, U_4 displays an inverse anisotropy in m^* as compared with U_2, which derives from the hybridization between adjacent LUMO+2 states along the short axis of naphthalene.

The wave functions of unoccupied states in Fig. 3.4(a) have been used as a clue to the origins of the IPS-like states of naphthalene on graphene. Since IPS-like states are characterized by wave functions extended around the surface, e.g. U_2 can be readily attributed to the bonding hybridization between the graphene LIPS and the IPS-like state of naphthalene with even parity. The anti-bonding state between them, however, also hybridizes with naphthalene LUMO+2, and the interpretation of the resulting wave functions leaves some ambiguities. To distinguish more

clearly the MO- and IPS-like features of such wave functions, I plot in Fig. 3.6 the planar averages of charge density ($\overline{|\Psi|^2}$) for the unoccupied states as functions of height z from graphene. For comparison, the results for the graphene IPSs and IPS-like states of the naphthalene monolayer are also shown.

I first examine the averaged charge density for symmetric (anti-symmetric) IPS 1^+ (1^-) of graphene shown in Fig. 3.6(a). IPS 1^+ (1^-) is characterized by main peaks at $z = \pm 2.0$ (± 2.8) Å with long tails, as well as a small single (double) peak around

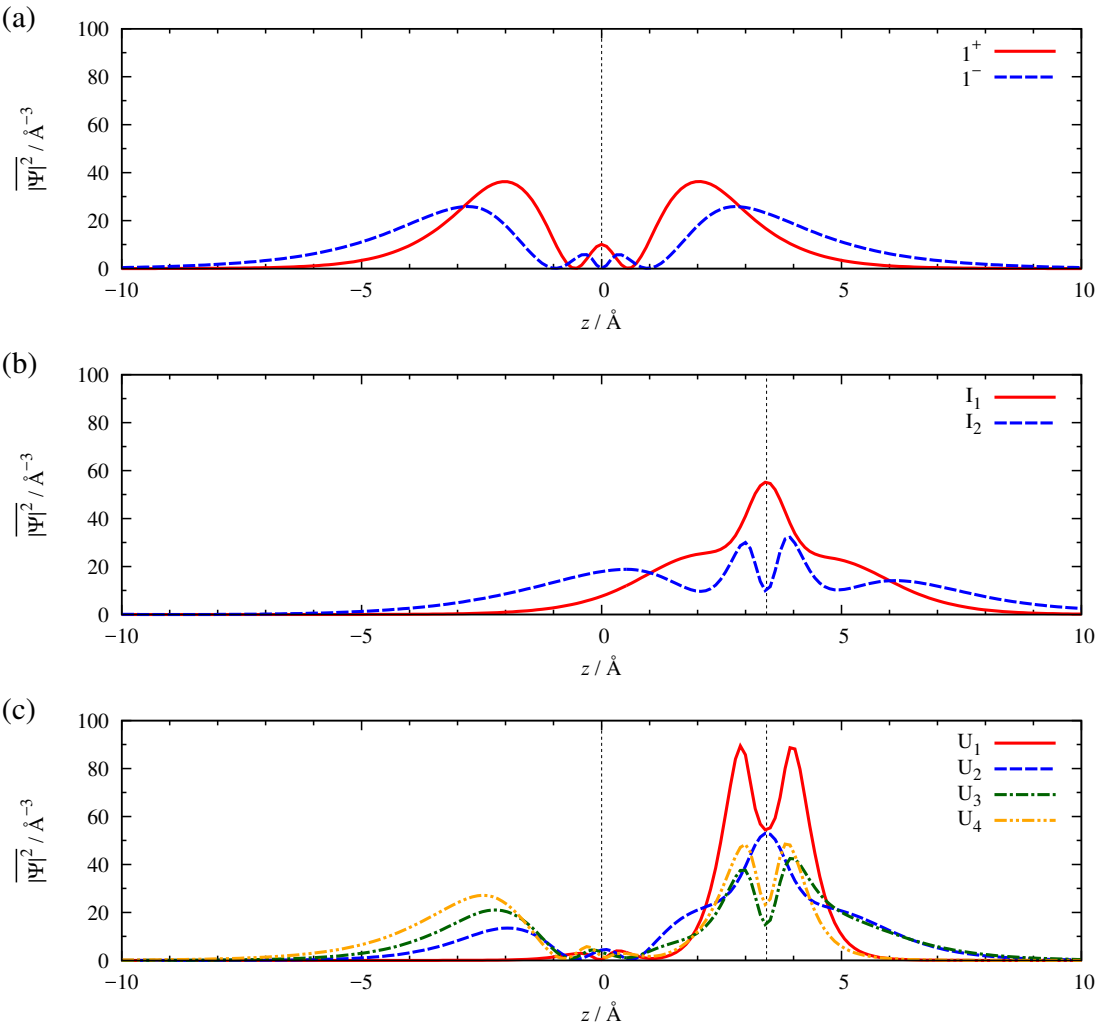

FIGURE 3.6: Planer averages of charge density for (a) the graphene IPSs, (b) the IPS-like states of naphthalene and (c) the unoccupied states of naphthalene on graphene.

graphene. Similar long-tail structures are also seen in $\overline{|\Psi|^2}$ for IPS-like states I_1 and I_2 of the naphthalene monolayer as shown in Fig. 3.6(b). Note that I_1 and I_2 behave like graphene IPSs in terms of the parabolic bands, but differ qualitatively from the latter in that $\overline{|\Psi|^2}$ has a largest amplitude near the naphthalene monolayer. I now analyze the averaged charge densities for the unoccupied states U_1, U_2, U_3 and U_4 of naphthalene on graphene shown in Fig. 3.6(c). From the exponentially decaying large double peak of U_1 localized near naphthalene, one can confirm that U_1 derives essentially from naphthalene LUMO+1. A similar localized behavior is also observed for U_4 near naphthalene, whereas its $\overline{|\Psi|^2}$ behaves like an IPS around graphene. This suggests that the IPS-like character of the roughly isotropic parabolic dispersions of U_4 essentially derives from graphene IPSs, and its large effective mass is due to naphthalene MOs. On the other hand, $\overline{|\Psi|^2}$ for U_2 behaves like 1^+ (I_1) around graphene (naphthalene), which clearly indicates that U_2 is formed by the hybridization between these two IPSs. U_3 also displays long-tail structures both around graphene and naphthalene, but its $\overline{|\Psi|^2}$ has a double peak similar to U_1 near naphthalene.

3.5 STM simulation

Finally, I simulate the STM images of naphthalene on graphene using the relaxed geometry and charge density obtained for the $(2\sqrt{3}\times 2\sqrt{3})$ unit cell. For simplicity, I neglect the shift in the energy bands due to the electric field from the tip. The simulated STM images are obtained at several sample bias voltages V_S as shown in Fig. 3.7, where the results at negative (positive) V_S probe occupied

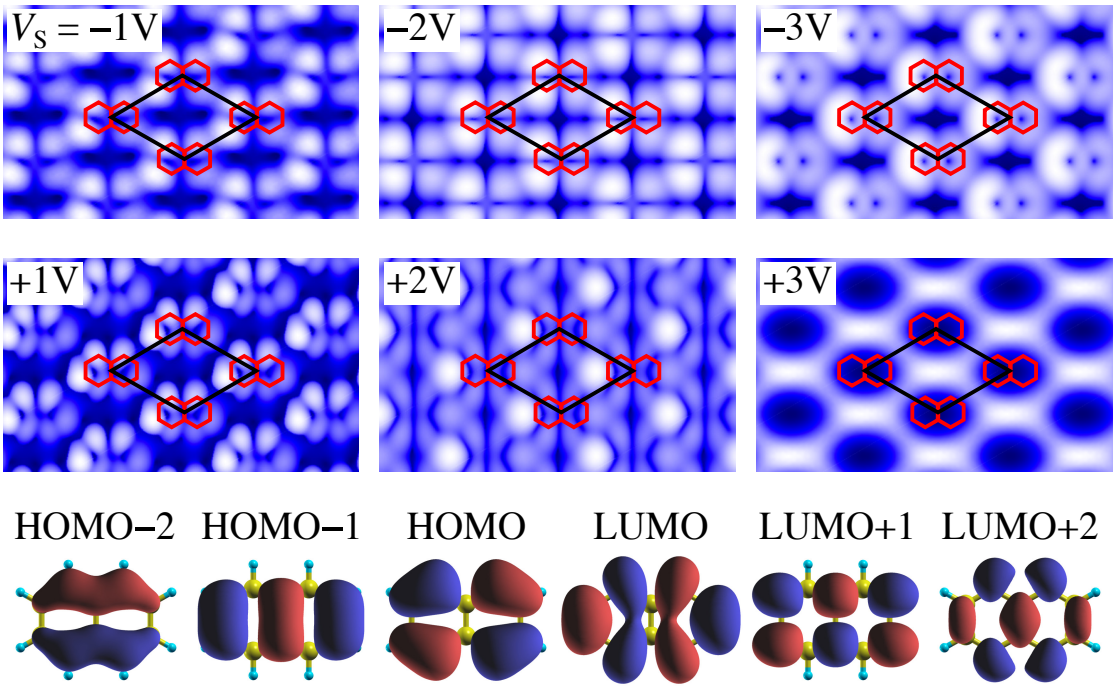

FIGURE 3.7: (Color online) Simulated STM images of naphthalene on graphene with the $(2\sqrt{3} \times 2\sqrt{3})$ periodicity. The results are obtained at sample bias voltages $V_S = \pm 1, \pm 2$ and ± 3 V. The bright (dark) regions correspond to protrusions (depressions), and the rhombus and hexagons denote the $(2\sqrt{3} \times 2\sqrt{3})$ unit cell and the benzene rings of naphthalene, respectively. Several MOs of naphthalene are depicted for comparison in the lower panels.

(unoccupied) states. The image at $V_S = -1$ V is characterized by four bright spots on each naphthalene molecule, which are asymmetric with respect to the long axis of naphthalene. The bright spots correspond to the carbon atoms of naphthalene not stacking with those of graphene in analogy to HOPG surfaces [46], detecting the hybridization between the HOMO of naphthalene and the π-bands of graphene. The contribution from the HOMO becomes more prominent at $V_S = -2$ V, where neighboring bright spots merge into dumbbell-like protrusions with two orientations, which is similar to the experimental image at $V_S = -3.1$ V [17] in that the pattern consists of two types of bright spots. At $V_S = -3$ V, the contribution from the HOMO-1 state is superposed, and as a result the obtained image resembles the benzene rings of naphthalene molecules.

At positive sample biases, on the other hand, the simulated STM images reflect the characteristics of unoccupied states including the IPS-like states. As in the case of $V_S = -1$ V, the absence of the mirror symmetry is also seen at $V_S = +1$ V, where the π-orbitals of graphene now hybridize with the LUMO of naphthalene. At $V_S = +2$ V, protrusions analogous to the naphthalene LUMO merge with those of neighboring molecules, and the bright spots corresponding to higher carbon atoms form a triangular lattice. Intriguingly, the STM image obtained at $V_S = +3$ V displays oval protrusions at the interstitial regions between the molecules, which are quite unlike any naphthalene MOs. This indicates that the hybrid IPS (U_2) predominantly contributes to the STM image. Our results explain the origin of the elongated eval protrusions observed experimentally, which have previously been attributed to the LUMO of naphthalene [17]. This also suggests that the hybrid IPSs can be imaged experimentally with STM.

3.6 Conclusions

I have theoretically investigated the naphthalene adsorption on graphene using the vdW-DF method. The results show that the molecular adsorption is stabilized by the formation of the $(2\sqrt{3}\times 2\sqrt{3})$ superstructure with a tilted adsorption geometry, in good agreement with the STM results on HOPG surfaces. More importantly, the intermolecular interaction induces IPS-like states on the naphthalene overlayer, which hybridize with the graphene IPSs in the bonding and anti-bonding manners. The impact of the naphthalene adsorption appear most prominently in the anisotropic effective mass of the resultant hybrid IPSs, which strongly reflects

the molecular structure of naphthalene. It is expected that similar hybrid IPSs widely exist at interfaces of molecular overlayers and solid surfaces.

References

[1] M. W. Cole and M. H. Cohen, "Image-potential-induced surface bands in insulators," *Phys. Rev. Lett.*, vol. 23, pp. 1238–1241, Nov 1969.

[2] P. M. Echenique and J. B. Pendry, "The existence and detection of Rydberg states at surfaces," *J. Phys. C: Solid State Phys.*, vol. 11, no. 10, p. 2065, 1978.

[3] M. Posternak, A. Baldereschi, A. J. Freeman, E. Wimmer, and M. Weinert, "Prediction of electronic interlayer states in graphite and reinterpretation of alkali bands in graphite intercalation compounds," *Phys. Rev. Lett.*, vol. 50, p. 761, Mar 1983.

[4] V. M. Silkin, J. Zhao, F. Guinea, E. V. Chulkov, P. M. Echenique, and H. Petek, "Image potential states in graphene," *Phys. Rev. B*, vol. 80, p. 121408, Sep 2009.

[5] B. E. Granger, P. Král, H. R. Sadeghpour, and M. Shapiro, "Highly extended image states around nanotubes," *Phys. Rev. Lett.*, vol. 89, p. 135506, Sep 2002.

[6] M. Feng, J. Zhao, and H. Petek, "Atomlike, hollow-core–bound molecular orbitals of C_{60}," *Science*, vol. 320, no. 5874, p. 359, 2008.

[7] M. Zamkov, H. S. Chakraborty, A. Habib, N. Woody, U. Thumm, and P. Richard, "Image-potential states of single and multiwalled carbon nanotubes," *Phys. Rev. B*, vol. 70, p. 115419, Sep 2004.

[8] M. Zamkov, N. Woody, B. Shan, H. S. Chakraborty, Z. Chang, U. Thumm, and P. Richard, "Time-resolved photoimaging of image-potential states in carbon nanotubes," *Phys. Rev. Lett.*, vol. 93, p. 156803, Oct 2004.

[9] A. Thess, R. Lee, P. Nikolaev, H. Dai, P. Petit, J. Robert, C. Xu, Y. H. Lee, S. G. Kim, A. G. Rinzler, D. T. Colbert, G. E. Scuseria, D. Tománek, J. E. Fischer, and R. E. Smalley, "Crystalline ropes of metallic carbon nanotubes," *Science*, vol. 273, no. 5274, pp. 483–487, 1996.

[10] S. Okada, A. Oshiyama, and S. Saito, "Nearly free electron states in carbon nanotube bundles," *Phys. Rev. B*, vol. 62, p. 7634, Sep 2000.

[11] S. Saito and A. Oshiyama, "Cohesive mechanism and energy bands of solid C_{60}," *Phys. Rev. Lett.*, vol. 66, p. 2637, May 1991.

[12] J. Zhao, M. Feng, J. Yang, and H. Petek, "The superatom states of fullerenes and their hybridization into the nearly free electron bands of fullerites," *ACS Nano*, vol. 3, no. 4, p. 853, 2009.

[13] S. Okada, S. Saito, and A. Oshiyama, "Energetics and electronic structures of encapsulated C_{60} in a carbon nanotube," *Phys. Rev. Lett.*, vol. 86, pp. 3835–3838, Apr 2001.

[14] G. Csányi, P. B. Littlewood, A. H. Nevidomskyy, C. J. Pickard, and B. D. Simons, "The role of the interlayer state in the electronic structure of superconducting graphite intercalated compounds," *Nat. Phys.*, vol. 1, p. 42, Oct. 2005.

[15] C. Bondi, P. Baglioni, and G. Taddei, "Structure of the monolayers of aromatic molecules adsorbed on graphite," *Chem. Phys.*, vol. 96, no. 2, p. 277, 1985.

[16] U. Bardi, S. Magnanelli, and G. Rovida, "Leed study of benzene and naphthalene monolayers adsorbed on the basal plane of graphite," *Langmuir*, vol. 3, no. 2, p. 159, 1987.

[17] T. Yamada, Y. Takano, M. Isobe, K. Miyakubo, and T. Munakata, "Growth and adsorption geometry of naphthalene overlayers on HOPG studied by low-temperature scanning tunneling microscopy," *Chem. Phys. Lett.*, vol. 546, p. 136, 2012.

[18] T. Yamada, M. Isobe, M. Shibuta, H. S. Kato, and T. Munakata, "Spectroscopic investigation of unoccupied states in nano- and macroscopic scale: Naphthalene overlayers on highly oriented pyrolytic graphite studied by combination of scanning tunneling microscopy and two-photon photoemission," *J. Phys. Chem. C*, vol. 118, no. 2, p. 1035, 2014.

[19] F. Sojka, M. Meissner, T. Yamada, T. Munakata, R. Forker, and T. Fritz, "Naphthalene's six shades on graphite: A detailed study on the polymorphism of an apparently simple system," *J. Phys. Chem. C*, vol. 120, no. 40, p. 22972, 2016.

[20] G. Grosso and G. P. Parravicini, *Solid State Physics*. Academic Press, 2000.

[21] M. Dion, H. Rydberg, E. Schröder, D. C. Langreth, and B. I. Lundqvist, "Van der Waals density functional for general geometries," *Phys. Rev. Lett.*, vol. 92, p. 246401, Jun 2004.

[22] K. Berland, V. R. Cooper, K. Lee, E. Schröder, T. Thonhauser, P. Hyldgaard, and B. I. Lundqvist, "Van der Waals forces in density functional theory: a review of the vdw-df method," *Rep. Prog. Phys.*, vol. 78, no. 6, p. 066501, 2015.

[23] I. Hamada, Y. Hamamoto, and Y. Morikawa, "Image potential states from the van der Waals density functional," *J. Chem. Phys.*, vol. 147, no. 4, p. 044708, 2017.

[24] Y. Morikawa, K. Iwata, and K. Terakura, "Theoretical study of hydrogenation process of formate on clean and Zn deposited Cu(111) surfaces," *Appl. Surf. Sci.*, vol. 169-170, p. 11, 2001.

[25] N. Troullier and J. L. Martins, "Efficient pseudopotentials for plane-wave calculations," *Phys. Rev. B*, vol. 43, p. 1993, Jan 1991.

[26] T. Thonhauser, V. R. Cooper, S. Li, A. Puzder, P. Hyldgaard, and D. C. Langreth, "Van der Waals density functional: Self-consistent potential and the nature of the van der Waals bond," *Phys. Rev. B*, vol. 76, p. 125112, Sep 2007.

[27] G. Román-Pérez and J. M. Soler, "Efficient implementation of a van der Waals density functional: Application to double-wall carbon nanotubes," *Phys. Rev. Lett.*, vol. 103, p. 096102, Aug 2009.

[28] J. Wu and F. Gygi, "A simplified implementation of van der Waals density functionals for first-principles molecular dynamics applications," *J. Chem. Phys.*, vol. 136, p. 224107, June 2012.

[29] Y. Hamamoto, I. Hamada, K. Inagaki, and Y. Morikawa, "Self-consistent van der Waals density functional study of benzene adsorption on Si(100)," *Phys. Rev. B*, vol. 93, p. 245440, Jun 2016.

[30] I. Hamada, "Van der Waals density functional made accurate," *Phys. Rev. B*, vol. 89, p. 121103, Mar 2014.

[31] I. Lončarić and V. Despoja, "Benchmarking van der Waals functionals with noncontact RPA calculations on graphene-Ag(111)," *Phys. Rev. B*, vol. 90, p. 075414, Aug 2014.

[32] P. Han, K. Akagi, F. Federici Canova, H. Mutoh, S. Shiraki, K. Iwaya, P. S. Weiss, N. Asao, and T. Hitosugi, "Bottom-up graphene-nanoribbon fabrication reveals chiral edges and enantioselectivity," *ACS Nano*, vol. 8, no. 9, p. 9181, 2014.

[33] F. Huttmann, A. J. Martínez-Galera, V. Caciuc, N. Atodiresei, S. Schumacher, S. Standop, I. Hamada, T. O. Wehling, S. Blügel, and T. Michely, "Tuning the van der Waals interaction of graphene with molecules via doping," *Phys. Rev. Lett.*, vol. 115, p. 236101, Dec 2015.

[34] B. Yang, J. Björk, H. Lin, X. Zhang, H. Zhang, Y. Li, J. Fan, Q. Li, and L. Chi, "Synthesis of surface covalent organic frameworks via dimerization and cyclotrimerization of acetyls," *J. Am. Chem. Soc.*, vol. 137, no. 15, p. 4904, 2015.

[35] M. Callsen and I. Hamada, "Assessing the accuracy of the van der Waals density functionals for rare-gas and small molecular systems," *Phys. Rev. B*, vol. 91, p. 195103, May 2015.

[36] Y. Baskin and L. Meyer, "Lattice constants of graphite at low temperatures," *Phys. Rev.*, vol. 100, p. 544, Oct 1955.

[37] J. Tersoff and D. R. Hamann, "Theory of the scanning tunneling microscope," *Phys. Rev. B*, vol. 31, p. 805, Jan 1985.

[38] J. Tersoff and D. R. Hamann, "Theory and application for the scanning tunneling microscope," *Phys. Rev. Lett.*, vol. 50, p. 1998, Jun 1983.

[39] S. D. Chakarova-Käck, E. Schröder, B. I. Lundqvist, and D. C. Langreth, "Application of van der Waals density functional to an extended system: Adsorption of benzene and naphthalene on graphite," *Phys. Rev. Lett.*, vol. 96, p. 146107, Apr 2006.

[40] M. Otani and O. Sugino, "First-principles calculations of charged surfaces and interfaces: A plane-wave nonrepeated slab approach," *Phys. Rev. B*, vol. 73, p. 115407, Mar 2006.

[41] I. Hamada, M. Otani, O. Sugino, and Y. Morikawa, "Green's function method for elimination of the spurious multipole interaction in the surface/interface slab model," *Phys. Rev. B*, vol. 80, p. 165411, Oct 2009.

[42] J. B. Neaton, M. S. Hybertsen, and S. G. Louie, "Renormalization of molecular electronic levels at metal-molecule interfaces," *Phys. Rev. Lett.*, vol. 97, p. 216405, Nov 2006.

[43] K. S. Thygesen and A. Rubio, "Renormalization of molecular quasiparticle levels at metal-molecule interfaces: Trends across binding regimes," *Phys. Rev. Lett.*, vol. 102, p. 046802, Jan 2009.

[44] J. M. Garcia-Lastra, C. Rostgaard, A. Rubio, and K. S. Thygesen, "Polarization-induced renormalization of molecular levels at metallic and semiconducting surfaces," *Phys. Rev. B*, vol. 80, p. 245427, Dec 2009.

[45] A. B. F. Duncan, *Rydberg Series in Atoms and Molecules.* Academic Press, 1971.

[46] D. Tománek, S. G. Louie, H. J. Mamin, D. W. Abraham, R. E. Thomson, E. Ganz, and J. Clarke, "Theory and observation of highly asymmetric atomic structure in scanning-tunneling-microscopy images of graphite," *Phys. Rev. B*, vol. 35, p. 7790, May 1987.

Chapter 4

Platinum Single-atom Adsorption on Graphene

4.1 Background

High-performance electrocatalysts are highly desired for electrochemical energy conversion devices, such as photovoltaic cells and fuel cells. Platinum (Pt) is widely used as an electrocatalyst, as it exhibits high catalytic activity not only for hydrogen oxidation but also for oxygen reduction at low temperatures [1, 2]. Nevertheless, there are still urgent needs to address the high cost of Pt and to search for alternative catalysts, which use small amount of Pt or no Pt with earth-abundant materials. Tremendous efforts have been devoted to achieve these goals, including the use of non-precious metals for Pt-metal alloys [3, 4, 5, 6, 7, 8, 9], or the use of noble metal-free catalyst [10, 11, 12, 13]. Particularly interesting are Pt clusters supported by graphitic materials, such as carbon black, carbon nanotubes, and graphene, which have been extensively studied both experimentally [14, 15, 16, 17, 18, 19, 20] and theoretically [21, 22, 23, 24, 25, 26, 27, 28, 29, 30, 31,

32, 33, 34]. A better catalytic activity of small Pt clusters supported by graphene sheet has been demonstrated experimentally [16, 17]. These results lead to the hypothesis that downsizing the Pt clusters to single atoms is able to enhance the catalytic activity. Recently, Sun *et al.* have successfully deposited single Pt atoms on graphene nanosheet using the atomic layer deposition and then demonstrated a significant improvement of the catalytic activity for methanol oxidation reaction [35]. Cheng *et al.* also showed that Pt single-atom catalyst deposited on nitrogen doped graphene nanosheet exhibits enhanced catalytic activity for the hydrogen evolution reaction [36]. The vacancies usually formed during preparation are expected to have strong interactions with the Pt atoms as demonstrated in several theoretical studies [23, 31, 32]. Back *et al.* have predicted the great potential of single atom catalyst supported on defective graphene for CO_2 electroreduction applications [37]. However, the dispersion of the single Pt atoms on graphene is limited to the number of the point defects. On the other hand, graphene edge might offer more space for depositing single Pt atoms. Kong *et al.* have theoretically investigated Pt single-atom adsorption at the edges of graphite nanofibers and found that the atoms are tightly bound to the edges due to the existence of active dangling bonds [38]. By employing transmission electron microscopy, structure and dynamics of Au [39], Fe [40], Cu [41], and Pt[41, 42] atoms at the edges have been studied. Some experimental studies also observed that Pt nano-clusters at the graphene edges are stable at high-temperatures [43, 44, 45]. However, the adsorption state and the catalytic activities of single Pt atoms are not yet fully understood.

In this work, I investigate the Pt single-atom adsorption on graphene by means of density functional theory (DFT) that includes the van der Waals forces. I perform systematic calculations to determine the adsorption state of single Pt atom on graphene, including defective graphene structures and graphene edges. Special emphasis is devoted to the graphene edges, as they are abundant in realistic conditions. I consider both zigzag and armchair edges, including the dependence on hydrogen termination. I examine their stability by taking into account the environmental effects, via DFT based thermodynamics [46]. I find that the single Pt atom adsorbs preferentially at the edge rather than on graphene, and the substitutional carbon site is the most stable one in a condition relevant to experiments. Furthermore, the core level shift (CLS) of Pt atom are calculated for each structure, which is used to validate the predicted structure against the experiment.

4.2 Computational Details

All the DFT calculations are carried out by using STATE code [47, 48] with ultrasoft pseudopotentials [49]. A plane-wave basis set is used to expand wave functions and augmentation charge with cutoff energies of 36 Ry and 400 Ry, respectively. I use rev-vdW-DF2 [50] exchange correlation functional as implemented [51] in the code with an efficient algorithm [52, 53]. Pseudopotentials are generated using the Perdew-Burke-Ernzerhof (PBE) [54] functional and the use of PBE pseudopotentials in rev-vdW-DF2 calculations is validated in Ref. 55. I use a (6×6) supercell to simulate Pt single-atom adsorption on pristine (GR), mono-carbon vacancy (V_1),

and di-carbon vacancy (V_2) of graphene structures. I introduce the 7575 member rings of graphene as a boundary between zigzag and armchair as observed in Ref. 56, denoted as grain-boundary graphene (GB-GR). I place the GB-GR at 17.23 Å × 14.03 Å rectangular lattice. I also construct disorder graphene (DisGR) reported in Ref. 57, and place it in a 20.37 Å × 24.67 Å rectangular lattice. Brillouin zone integration is performed for all structures using the Γ-centered 4 × 4 k-point mesh for pristine, mono-carbon vacancy, and di-carbon vacancy graphenes; 2×3 k-point mesh for GB-GR; and the Γ-point for DisGR. To investigate the edge effect in the Pt adsorption, I employ the graphene nanoribbons (GNR) with zigzag (zGNR) and armchair (aGNR) edges with different terminations, including nonhydrogenated, mono-hydrogenated, and di-hydrogenated ones, as shown in Figs. 4.1 and 4.2 for zGNR and aGNR, respectively. I follow the convention used in Ref. 58, i.e., z_n denotes zGNR with n hydrogen atoms at the edge carbon site, and a_n for aGNR with n hydrogen atoms. Spin polarization is taken into account for all the system.

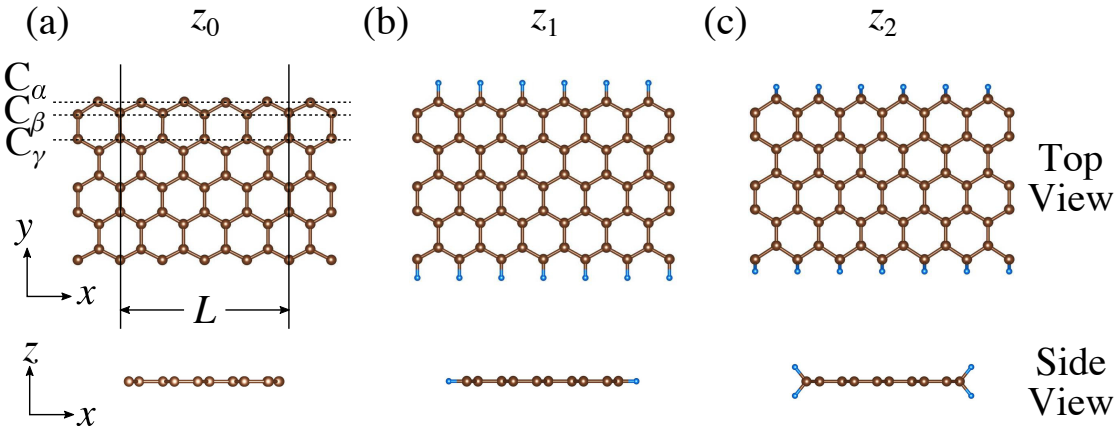

FIGURE 4.1: Structures of nonhydrogenated zGNR (a), mono-hydrogenated zGNR (b), and di-hydrogenated zGNR (c). Brown (blue) spheres represent carbon (hydrogen) atoms. The first, second, and third outermost carbon atoms are denoted as C_α, C_β, and C_γ, respectively. L indicates the periodicity of the ribbons along the edge direction.

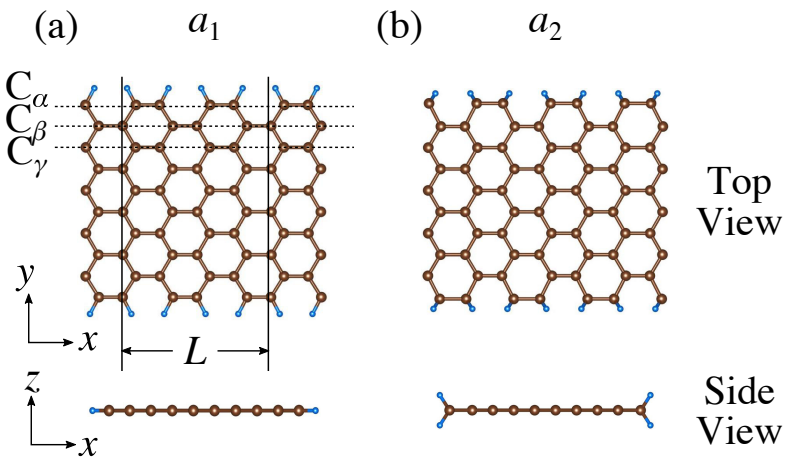

FIGURE 4.2: Structures of mono-hydrogenated aGNR (a), and di-hydrogenated aGNR (b). Brown (blue) spheres represent carbon (hydrogen) atoms. The first, second, and third outermost carbon atoms are denoted as C_α, C_β, and C_γ, respectively. L indicates the periodicity of the ribbons along the edge direction.

The zGNR has the localized spin with ferromagnetic order along the edge and antiparallel orientation between the edges as reported in Refs. 59 and 60, while such localized spin does not appears at the edge of aGNR. GNRs are modeled using periodic supercell along the edges, having the same configurations on both edges. Following the conventional notation, the width of GNR is specified by the number of zigzag chain and dimer lines for zGNR and aGNR, respectively, and I use 5-zGNR and 10-aGNR in this work. I use supercells containing 4 hexagons for both zGNR and aGNR, and resulting supercells contain 40 carbon atoms. Supercells in the graphene plane directions correspond to $(4\times 6\sqrt{3})$ and $(2\sqrt{3}\times 12)$ supercells of graphene for zGNR and aGNR, respectively, and graphene planes are separated by a vacuum layer of $\sim$15 Å thickness. Resulting vacuum thickness between edges are 16.48 Å and 18.70 Å for zGNR and aGNR, respectively. Brillouin zone integration is performed using the Γ-centered 6×2 k-points for both zGNR and aGNR. All the graphene based structures considered in this work are constructed using the lattice constant of graphene obtained using rev-vdW-DF2 (2.46 Å) [61], which is in good

agreement with the experimental value for graphite (2.4589 ± 0.0005 Å) [62]. The structures are fully relaxed until the forces acting on the atoms becomes smaller than 5.14×10^{-2} eV/Å (1×10^{-3} Hartree/Bohr). The Pt $4f$ CLS including the final state screening is calculated as the difference between the core level binding energy of Pt adsorbed GNR and bulk Pt [63, 64, 65].

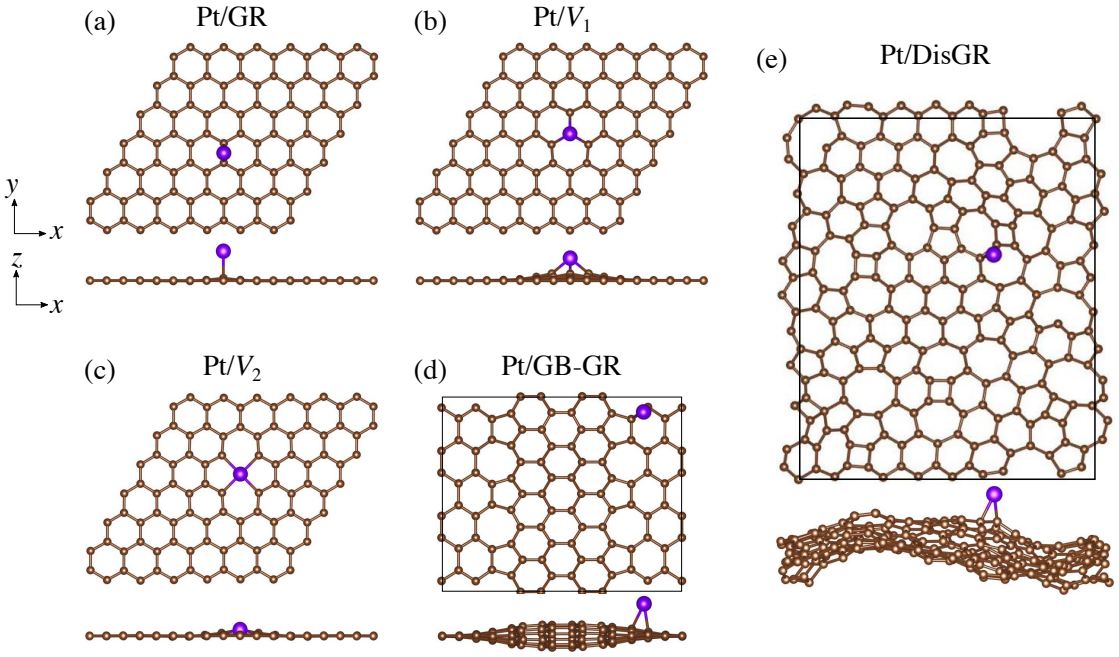

FIGURE 4.3: Optimized structures of Pt atom adsorption on (a) pristine graphene (GR), (b) graphene with carbon mono-vacancy (V_1), (c) graphene with carbon di-vacancy (V_2), (d) grain-boundary graphene (GB-GR), and (e) disorder graphene (DisGR).

4.3 Results and Discussion

4.3.1 Pt adsorption on pristine and defective graphene structures

I first consider pristine and defective graphene structures and adsorption of single Pt atom on them as shown in Fig. 4.3. I calculate the binding energy defined by

$$E_b = E_{\mathrm{Pt/G}} - E_{\mathrm{G}} - \mu_{\mathrm{Pt}}, \tag{4.1}$$

where $E_{\mathrm{Pt/G}}$, E_{G}, and μ_{Pt} are the total energy of the adsorption system, the total energy of substrate, and the chemical potential of Pt, respectively. I use the total energy of single Pt atom for μ_{Pt}. In Table 4.1, I summarize the calculated binding energies of single Pt atom on pristine and defective graphene structures. The binding energy for the pristine graphene is slightly larger than those reported in Ref. 26 because of the exchange-correlation functionals used (see Table 4.1 for the binding energies calculated using the PBE [54] functional). The Pt single-atom adsorption on graphene with vacancy is significantly stable, because the Pt atom terminates dangling bonds associated with the C vacancy. However, the energies necessary to create the C vacancies (formation energies for C vacancy with respect to the C atom in graphene) are 7.77 eV and 7.86 eV for V_1 and V_2, respectively, and the effective binding energies are +0.07 eV and +0.29 eV, respectively. Thus I conclude that the Pt single-atom adsorption at the C vacancy site is thermodynamically less favorable. The binding energies of single Pt atom

TABLE 4.1: Binding energy (E_b) of Pt single-atom adsorption for several graphene based structures, calculated using rev-vdW-DF2 and PBE functionals.

Structure	E_b / eV	
	rev-vdW-DF2	PBE
Pt/GR	−1.97	−1.61
Pt/V_1	−7.70	−7.35
Pt/V_2	−7.57	−7.29
Pt/GB-GR	−2.55	−2.20
Pt/DisGR	−2.99	−2.69

for GB-GR and DisGR are apparently much larger than that for pristine graphene. However, this is because GB-GR and DisGR are less stable and thus more reactive than the pristine one. They are less stable than pristine graphene by 0.17 and 0.39 eV per C atom, respectively.

4.3.1.1 Pristine GNR

I then investigate the most stable GNR by calculating the formation energy defined by

$$E_{\text{form}} = \frac{1}{2L}\left(E_{\text{GNR}} - N_{\text{C}}E_{\text{GR}} - \frac{N_{\text{H}}}{2}\mu_{\text{H}_2}\right), \tag{4.2}$$

where E_{GNR}, E_{GR}, μ_{H_2}, are the total energy of GNR, total energy of C atom in the bulk graphene (total energy of graphene per atom), and chemical potential of H_2 molecule, respectively; N_{C} (N_{H}) is the number of C (H) atom in GNR; and L is the length of the unit cell along the edge. Figure 4.4 shows the calculated formation energy as a function of H_2 chemical potential. It is found that at high H_2 chemical potential, aGNR (a_2) is stable, whereas zGNRs are more stable under low H_2 chemical potential, and non-hydrogenated GNR is unstable in a wide range of H_2 chemical potential, in good agreement with the previous study [58]. The

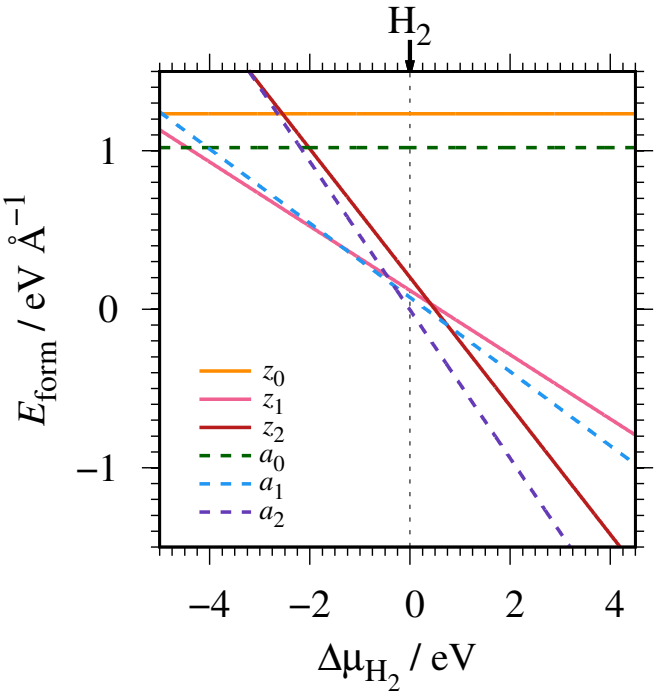

FIGURE 4.4: Formation energy of GNR as a function of H_2 chemical potential. $\Delta\mu_{H_2} = \mu_{H_2} - E_{H_2}$, where E_{H_2} is the total energy of a gas-phase H_2 molecule at 0 K.

positions of the intersections differ from those reported in Ref. 58, because the exchange-correlation functionals used are different (see Fig. 4.5 for comparison of the results obtained using rev-vdW-DF2 and PBE). In addition, I also confirm that the stability is insensitive to the GNR width as shown in Fig. 4.6.

To compare the stability of the GNRs with the defective graphene structures, I calculate the formation energy per C atom (replace $2L$ in Eq. 4.2 with N_C). At $\mu_{H_2} = E_{H_2}$, the formation energy per C atom of z_0, z_1, z_2, a_0, a_1, and a_2 are 0.61, 0.06, 0.10, 0.44, 0.03, and $\sim$ 0.00 eV, respectively. Thus, although most GNRs considered here are less stable than pristine graphene (i.e. most GNRs have positive E_{form} at $\mu_{H_2} = E_{H_2}$), hydrogenated GNRs are more stable than defective graphene structures.

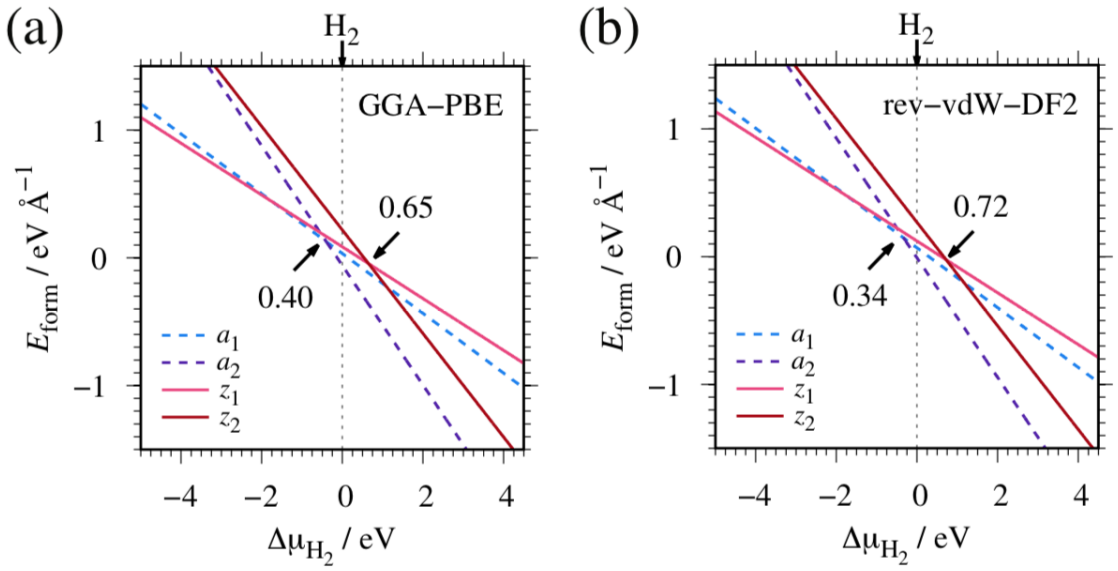

FIGURE 4.5: Formation energies (E_{form}) of armchair and zigzag graphene nanoribbon as a function of chemical potential of hydrogen molecule μ_{H_2}, calculated using (a) PBE and (b) rev-vdW-DF2. 20-aGNR and 10-zGNR are used.

4.3.2 Pt single-atom adsorption on zGNRs

I consider the Pt single-atom adsorption on non-hydrogenated zGNR (z_0). I systematically construct the adsorption configurations with and without defects, and

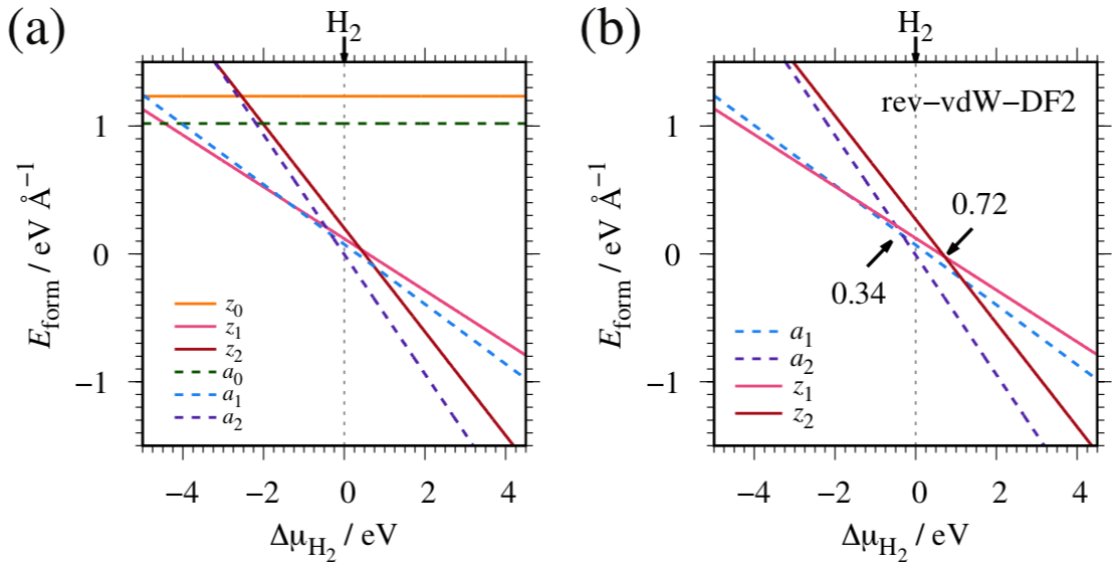

FIGURE 4.6: Formation energies (E_{form}) of armchair and zigzag graphene nanoribbon as a function of chemical potential of hydrogen molecule μ_{H_2}, calculated with (a) 10-aGNR and 5-zGNRand (b) 20-aGNR and 10-zGNR.

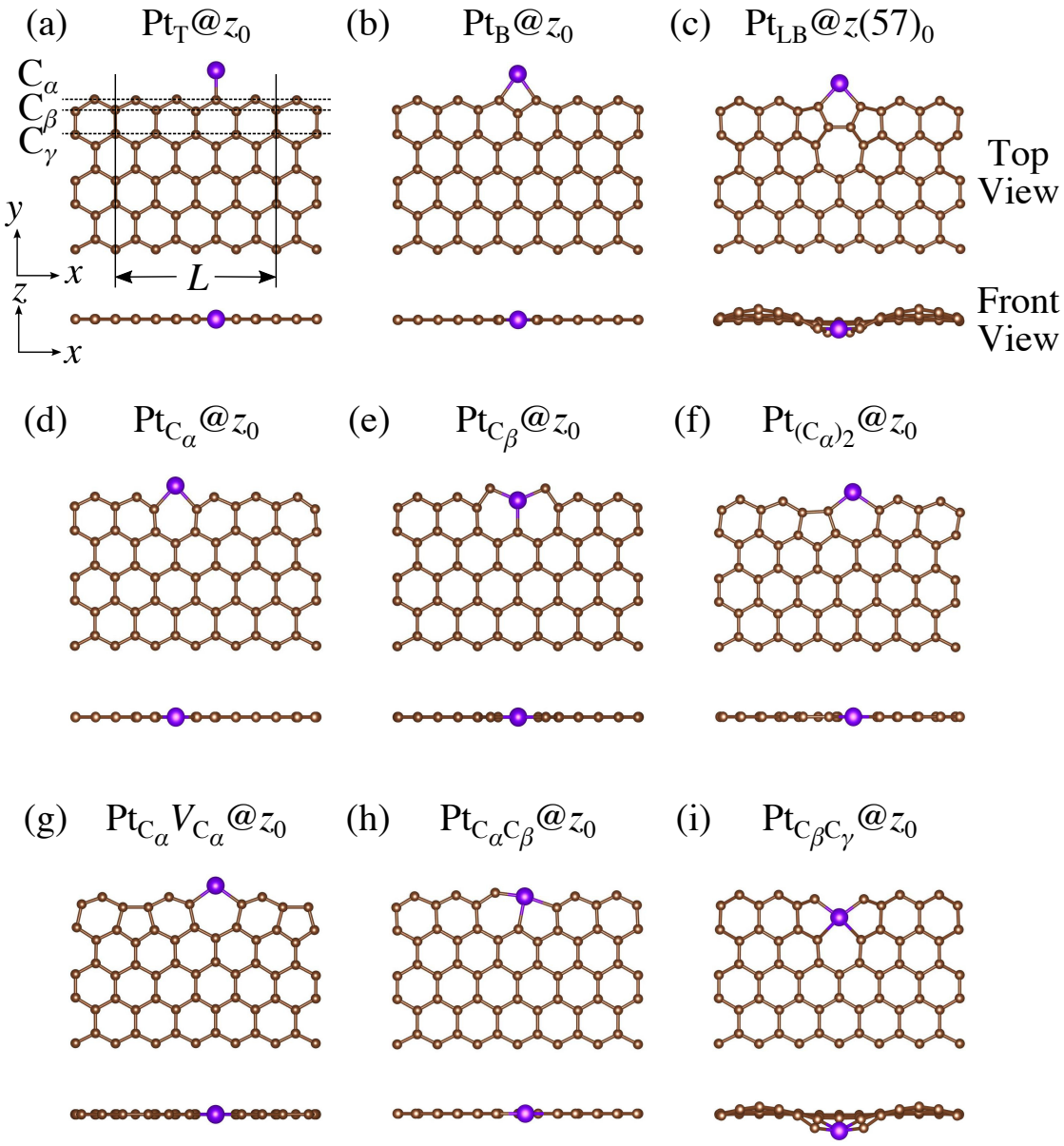

FIGURE 4.7: Optimized structures of Pt single-atom adsorption at the edge of non-hydrogenated zGNRs. Purple (brown) spheres represent of Pt (H) atoms. The first, second, and third outermost carbon atoms are denoted as C_α, C_β, and C_γ, respectively. L indicates the periodicity of the ribbons along the edge direction.

label them according to the Kröger-Vink notation [66], as shown in Fig. 4.7. I first consider the Pt single-atom adsorption at the top- and bridge-site of perfect z_0, denoted as $Pt_T@z_0$ [Fig. 4.7(a)] and $Pt_B@z_0$ [Fig. 4.7(b)], respectively. Second, I introduce a Stone-Wales (SW) defect at the edge of z_0, denoted as $z(57)_0$, and a Pt atom adsorbed at the long-bridge (LB) site of the SW defect, denoted as $Pt_{LB}@z(57)_0$ [Fig. 4.7(c)]. I introduce substitutional Pt with single edge carbon atoms (C_α, C_β) denoted as $Pt_{C_\alpha}@z_0$ [Fig. 4.7(d)] and $Pt_{C_\beta}@z_0$ [Fig. 4.7(e)], respectively. I also consider two outermost carbon vacancies (V_C), and obtained the Pt substituted with two V_C's, $Pt_{(}C_\alpha)_2@z_0$ [Fig. 4.7(f)], and a complex of a substitutional Pt and V_C, $Pt_{C_\alpha}V_{C_\alpha}@z_0$ [Fig. 4.7(g)]. Finally I consider Pt configurations with a divacancy formed with outermost and second outermost and that with second and third outermost C atoms, $Pt_{C_\alpha C_\beta}@z_0$ [Fig. 4.7(h)] and $Pt_{C_\beta C_\gamma}@z_0$ [Fig. 4.7(i)], respectively.

For the optimized structures with single Pt atom at the edge of z_0, I calculate the Gibbs free energy defined by

$$\Delta\Omega(\mu_C) = E_{Pt@GNR} - E_{ref} - \mu_{Pt} - \Delta N_C \mu_C, \tag{4.3}$$

where $E_{Pt@GNR}$ and E_{ref} are the total energies of adsorbed and reference systems, respectively; ΔN_C is the difference of the number of C atoms from the reference system; μ_{Pt} and μ_C are chemical potentials of Pt and C, respectively. Here the pristine graphene is chosen as the reference ($E_{ref} = E_{GR} \times N_C$, where N_C is the number of C atoms in perfect GNR). μ_{Pt} is chosen to be the total energy of single Pt atom (E_{Pt}) and μ_C is varied around the chemical potential of graphene.

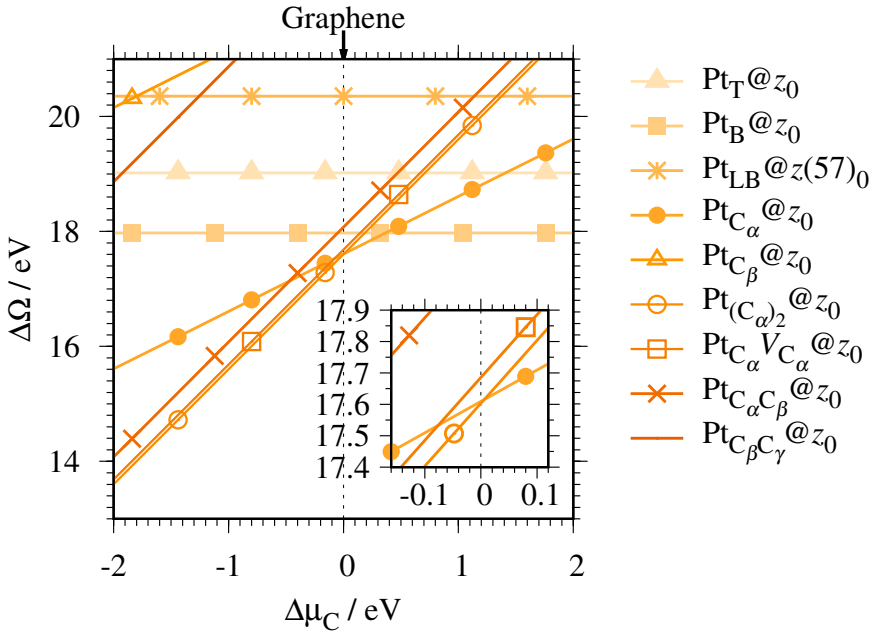

FIGURE 4.8: The Gibbs free energy for the pristine GNRs as a function of C chemical potentials. $\Delta\mu_C = \mu_C - E_{GR}$ is C chemical potential referenced to the total energy of graphene at 0 K (E_{GR}).

Figure 4.8 shows the Gibbs free energy as a function of C chemical potential for nine structures considered in this work, and those at $\mu_C = E_{GR}$ (the system is in equilibrium with graphene) are summarized in Table 4.2. We can see that all the structures have large positive Gibbs free energies at $\mu_C = E_{GR}$, suggesting that Pt single-atoms adsorption at the edges of z_0 is thermodynamically unstable. Among the Pt adsorption structures on z_0, $Pt_{C_\alpha}@z_0$ is the most favorable configuration. However, the calculated CLS for $Pt_{C_\alpha}@z_0$ is too small compared with the experimental value of (+2.0 ± 0.4) eV [42], suggesting this adsorption configuration is unlikely. On the other hand, $Pt_{C_\beta}@z_0$ and $Pt_{C_\beta C_\gamma}@z_0$ show relatively large CLS of +1.44 and +1.67 eV, respectively. However, their Gibbs free energies are significantly large, ruling out these configurations. Thus, it is concluded that Pt single-atom adsorption on the non-hydrogenated GNR is unlikely in the equilibrium condition.

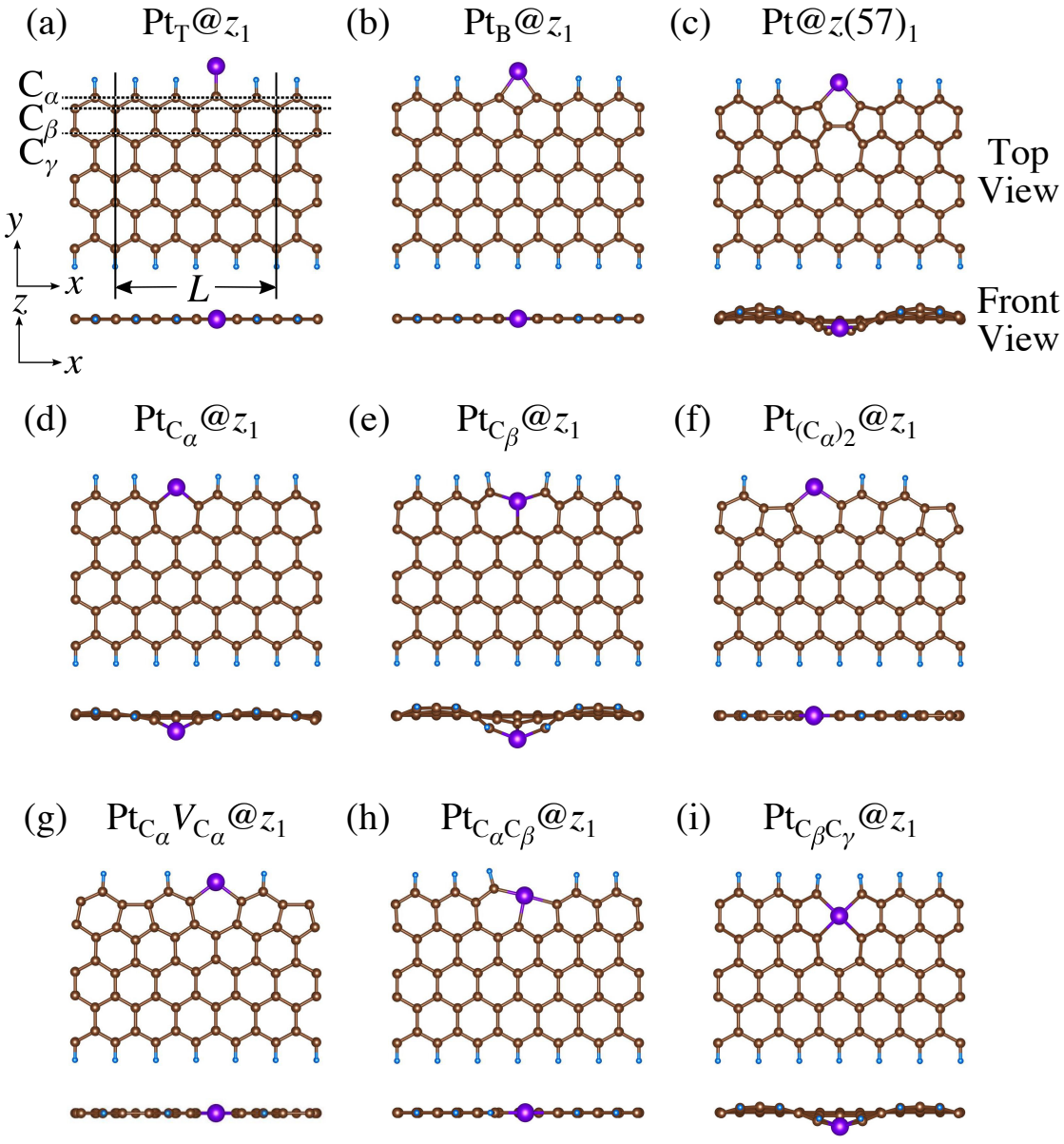

FIGURE 4.9: Optimized structures of Pt single-atom adsorption at the edges of mono-hydrogenated zGNRs. Purple, brown, and light blue spheres represent of Pt, C, H atoms, respectively. The first, second, and third outermost C atoms are denoted as C_α, C_β, and C_γ, respectively. L indicates the periodicity of the ribbons along the edge direction.

TABLE 4.2: Gibbs free energy ($\Delta\Omega$) and core level shift (CLS) of Pt atom@zGNRs at $\mu_C = E_{GR}$ and $\mu_H = E_{H_2}$.

	$\Delta\Omega(E_{GR}, E_{H_2})$ / eV			CLS / eV		
	z_0	z_1	z_2	z_0	z_1	z_2
Pt_T	+19.02	+0.15	+1.61	−0.56	−0.93	−1.30
Pt_B	+17.98	+1.57	+2.57	+0.44	+0.35	+0.35
Pt_{LB}[a]	+20.35	+3.88	+4.86	+0.44	+0.44	+0.29
Pt_{C_α}	+17.61	−0.25	+1.92	+0.50	+1.43	+1.20
Pt_{C_β}	+22.16	+1.89	+0.51	+1.44	+1.37	+1.42
$Pt_{(C_\alpha)_2}$	+17.60	+1.79	+2.98	−0.29	+0.24	+0.48
$Pt_{C_\alpha}V_{C_\alpha}$	+17.69	+2.02	+3.33	−0.42	+0.54	+0.88
$Pt_{C_\alpha C_\beta}$	+18.08	+0.14	+1.62	+0.81	+0.81	+0.52
$Pt_{C_\beta C_\gamma}$	+22.87	+2.11	+1.21	+1.67	+0.82	+1.11
Expt.	—	—	—		+2.0±0.4[b]	

[a] Pt_{LB} should be adsorbed at the edge of $z(57)_n$
[b] Taken from Ref. 42.

I then investigate the stability of Pt single-atom adsorption on mono- and di-hydrogenated zGNRs (z_1 and z_2). The structures are similar to those adopted for non-hydrogenated zGNRs as shown in Figs. 4.9 and 4.10 for z_1 and z_2, respectively. I optimized all the structures and calculated the Gibbs free energy given by

$$\Delta\Omega(\mu_C, \mu_{H_2}) = E_{Pt@GNR} - E_{ref} - \mu_{Pt} - \Delta N_C \mu_C - \frac{\Delta N_H}{2}\mu_{H_2}, \tag{4.4}$$

where $E_{Pt@GNR}$ (E_{ref}) is the total energy of adsorbed system (reference system), $\mu_{Pt} = E_{Pt}$, ΔN_C, and ΔN_H are the difference of numbers of C and H atoms from the reference system, respectively, and μ_C and μ_{H_2} are chemical potentials of C atom and H_2 molecule, respectively. As in the case of z_0, pristine graphene is chosen as the reference. I calculate $\Delta\Omega$ for z_0, z_1, and z_2 as a function of μ_{H_2} and μ_C and generate the phase diagram as shown in Fig. 4.11. I also calculate $\Delta\Omega$ at $\mu_C = E_{GR}$ and $\mu_{H_2} = E_{H_2}$ for the structures considered, where E_{H_2} is the total energy of an isolated H_2 molecule. The results are summarized in Table 4.2 along

with the calculated CLSs for each structure. As expected, single Pt atom adsorbed non-hydrogenated zGNR is unstable and does not appear in the phase diagram. I find that $\mathrm{Pt}_{\mathrm{C}_\alpha}@z_1$ only exhibits negative $\Delta\Omega$ at $\mu_{\mathrm{C}} = E_{\mathrm{GR}}$ and $\mu_{\mathrm{H}_2} = E_{\mathrm{H}_2}$, suggesting that this structure is thermodynamically stable under these conditions. Furthermore, the calculated CLS for this structure is in reasonable agreement with the experiment. Among the hydrogenated GNR structures, calculated CLSs for $\mathrm{Pt}_{\mathrm{C}_\beta}@z_1$ and $\mathrm{Pt}_{\mathrm{C}_\alpha}@z_2$ are also reasonable. However, they shows positive $\Delta\Omega$'s, implying these structures are less likely than $\mathrm{Pt}_{\mathrm{C}_\alpha}@z_1$.

4.3.3 Pt single-atom adsorption on aGNRs

I investigate the Pt single-atom adsorption at the edge of mono- and di-hydrogenated aGNRs. I do not consider non-hydrogenated aGNRs as the non-hydrogenated structures are unstable as observed in the case of zGNR. I consider the following structures: Pt adsorbed at short-bridge (SB) and long-bridge (LB) sites [Figs. 4.12(a) and 4.12(b), respectively]; substitutional Pt with single C atom respectively [Figs. 4.12(c)-(e)]; substitutional Pt with two C atoms [Figs. 4.12(f)-(i)]. I construct similar structures for dihydrogenated aGNR (Fig. 4.13). The structures are fully optimized and the Gibbs free energies are calculated according to Eq. (4.4). The phase diagram for aGNR is shown in Fig. 4.14, and $\Delta\Omega$'s at $\mu_{\mathrm{C}} = E_{\mathrm{GR}}$ and $\mu_{\mathrm{H}_2} = E_{\mathrm{H}_2}$ for different adsorption configurations are summarized in Table 4.3. I find that $\mathrm{Pt}_{\mathrm{C}_\alpha}@z_2$ is the most stable at $\mu_{\mathrm{C}} = E_{\mathrm{GR}}$ and $\mu_{\mathrm{H}_2} = E_{\mathrm{H}_2}$ with reasonable CLS, suggesting this structure is the most likely candidate in this condition. Furthermore, absolute value of calculated $\Delta\Omega$ is much larger than that

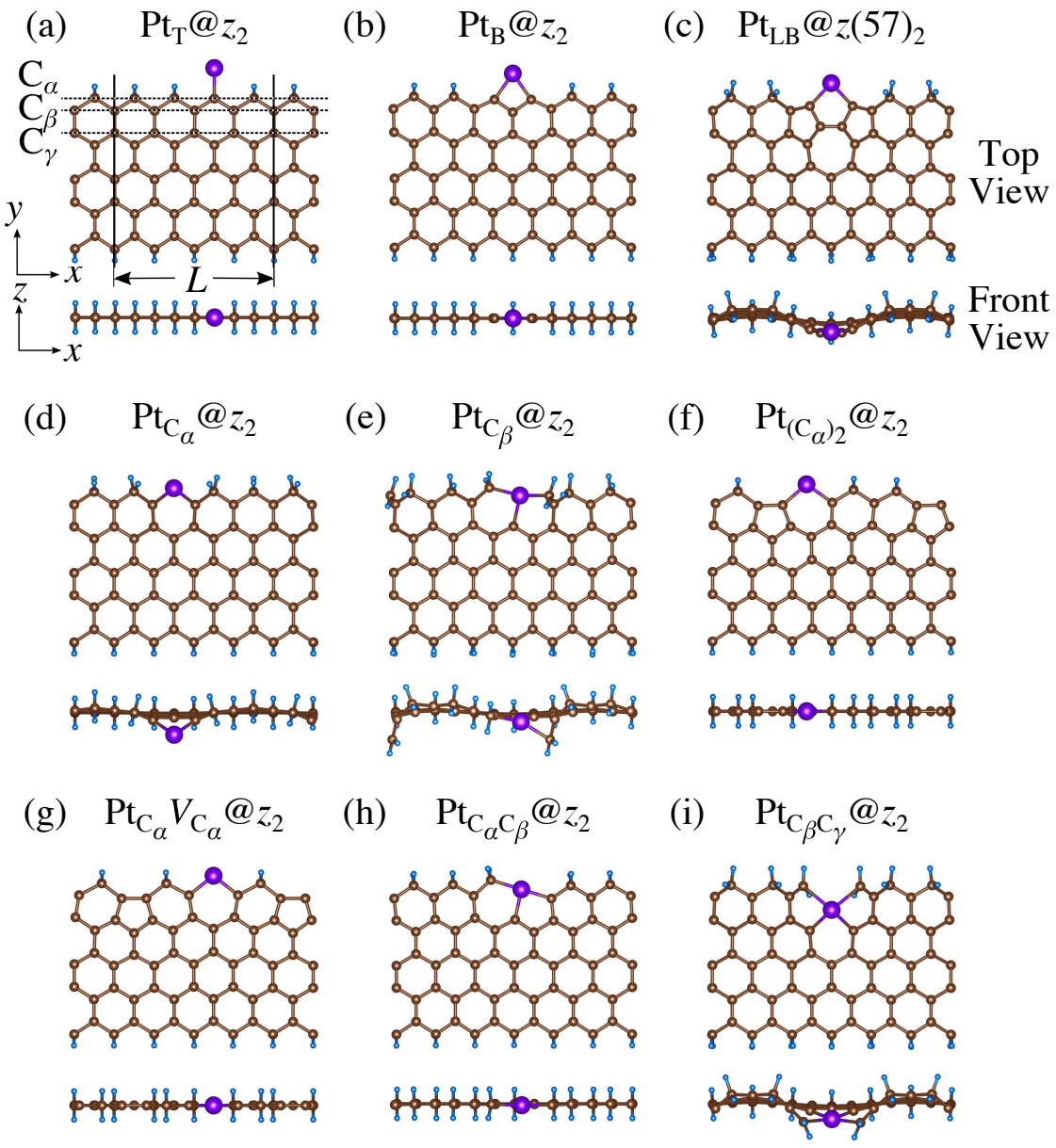

FIGURE 4.10: Optimized structures of Pt single-atom adsorption at the edges of di-hydrogenated zGNRs. Purple, brown, and light blue spheres represent of Pt, C, H atoms, respectively. The first, second, and third outermost C atoms are denoted as C_α, C_β, and C_γ, respectively. L indicates the periodicity of the ribbons along the edge direction.

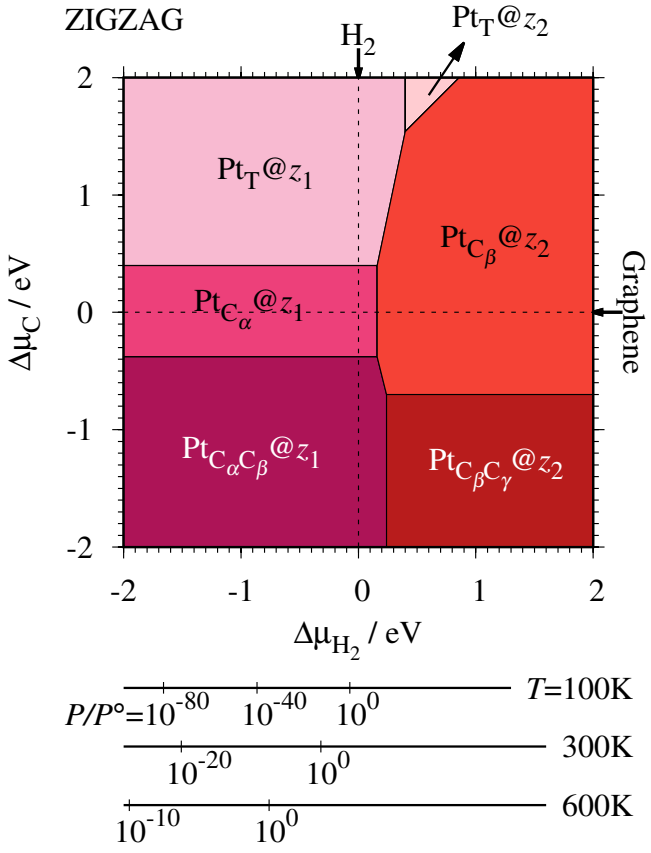

FIGURE 4.11: The Gibbs free energy for Pt single-atom adsorption at the edge of zGNRs as a function of C and H_2 chemical potentials. $\Delta\mu_C = \mu_C - E_{GR}$ and $\Delta\mu_{H_2} = \mu_{H_2} - E_{H_2}$ are C and H_2 chemical potentials referenced to the total energies of gas-phase H_2 and graphene, respectively. The bottom axes show the corresponding H_2 chemical potentials at the absolute temperature T and partial pressure P (with $P^\circ = 1$ atm), $\mu_{H_2} = H^\circ(T) - H^\circ(0) - TS^\circ(T) + k_B T \ln(P/P^\circ)$, where the enthalpy H° and the entropy S° are obtained from Ref. 67.

of the most stable zGNR, suggesting that Pt adsorbed at aGNR is thermodynamically more stable than Pt adsorbed zGNR. I also find that $Pt_{C_\beta}@a_1$, $Pt_{C_\gamma}@a_1$, and $Pt_{C_\gamma}@a_2$ show relatively large positive CLSs. However, they show large positive $\Delta\Omega$ at $\mu_C = E_{GR}$ and $\mu_{H_2} = E_{H_2}$ and therefore appear in the phase diagram (Fig. 4.14). In particular the latter two show large positive $\Delta\Omega$ and are less likely.

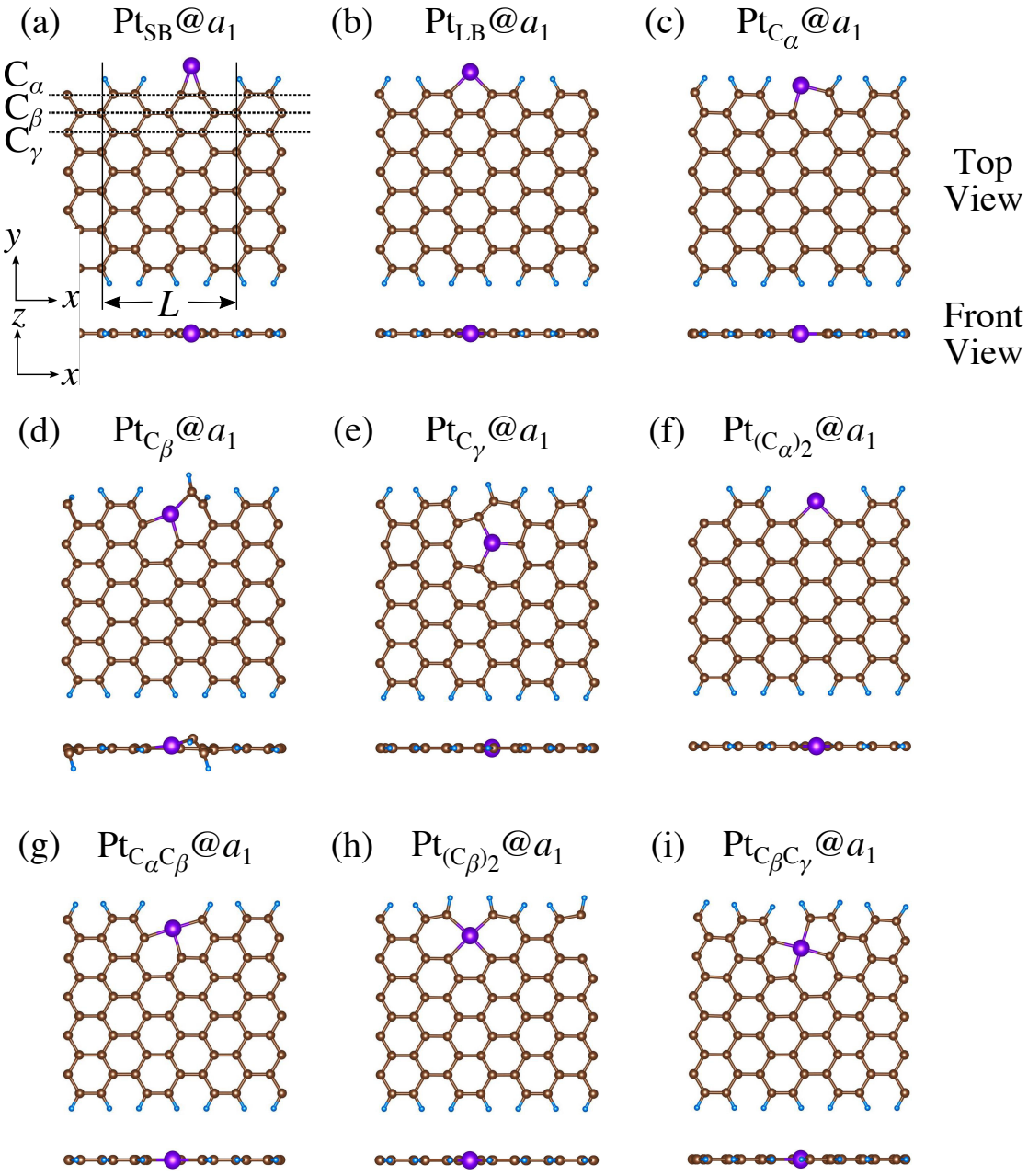

FIGURE 4.12: Optimized structures of Pt single-atom adsorption at the edges of mono-hydrogenated aGNRs. Purple, brown, and light blue spheres represent of Pt, C, H atoms, respectively. The first, second, and third outermost C atoms are denoted as C_α, C_β, and C_γ, respectively. L indicates the periodicity of the ribbons along the edge direction.

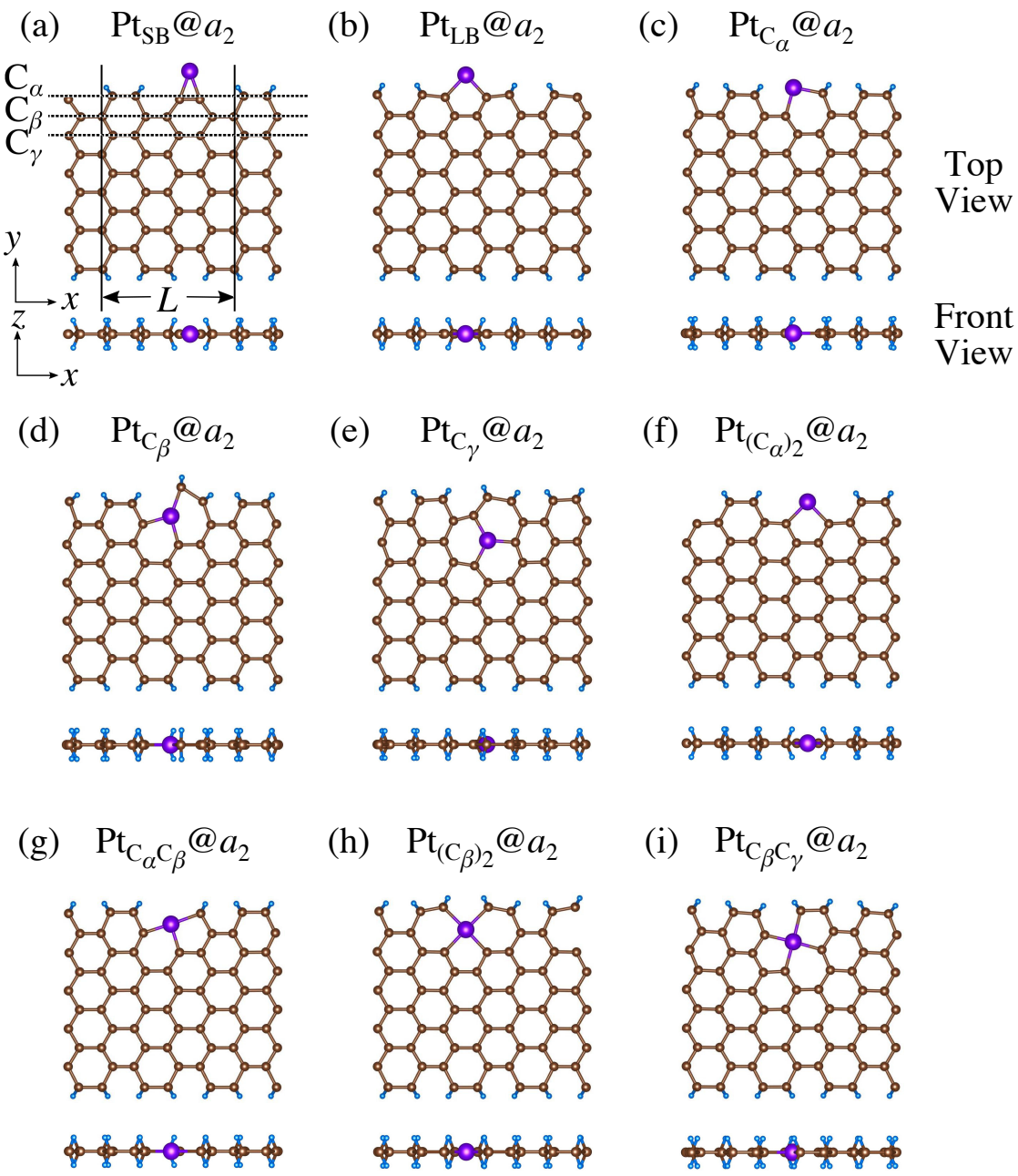

FIGURE 4.13: Optimized structures of Pt single-atom adsorption at the edges of di-hydrogenated aGNRs. Purple, brown, and light blue spheres represent of Pt, C, H atoms, respectively. The first, second, and third outermost C atoms are denoted as C_α, C_β, and C_γ, respectively. L indicates the periodicity of the ribbons along the edge direction.

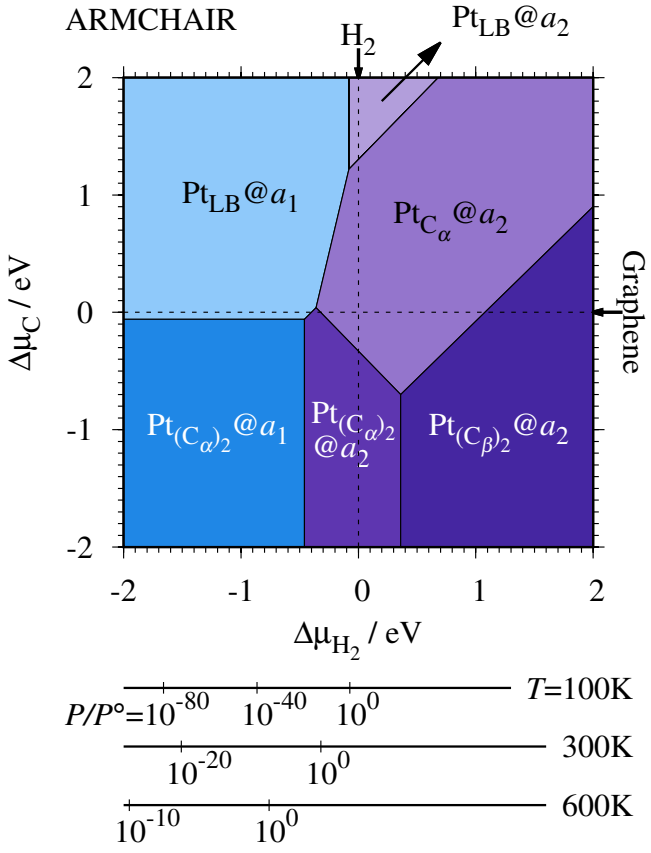

FIGURE 4.14: The Gibbs free energy for Pt single-atom adsorption at the edges of aGNRs as a function of C and H_2 chemical potentials. $\Delta\mu_C = \mu_C - E_{GR}$ and $\Delta\mu_{H_2} = \mu_{H_2} - E_{H_2}$ are C and H_2 chemical potentials referenced to the total energies of gas-phase H_2 and graphene, respectively. The bottom axes show the corresponding H_2 chemical potentials at the absolute temperature T and partial pressure P (with $P^\circ = 1$ atm), $\mu_{H_2} = H^\circ(T) - H^\circ(0) - TS^\circ(T) + k_B T \ln(P/P^\circ)$, where the enthalpy H° and the entropy S° are obtained from Ref. 67.

4.3.4 Impact of the substrate

Here I examine the effect of the substrate, as in the experiment [42], Pt single-atom adsorption has been observed at the step edge of graphite, and the graphene underneath may play some role. I perform the structural optimization with graphene substrate and calculate CLS of Pt single-atom at the edge of zGNR. I adopt the adsorption structures with z_1 and introduced graphene underneath as show in

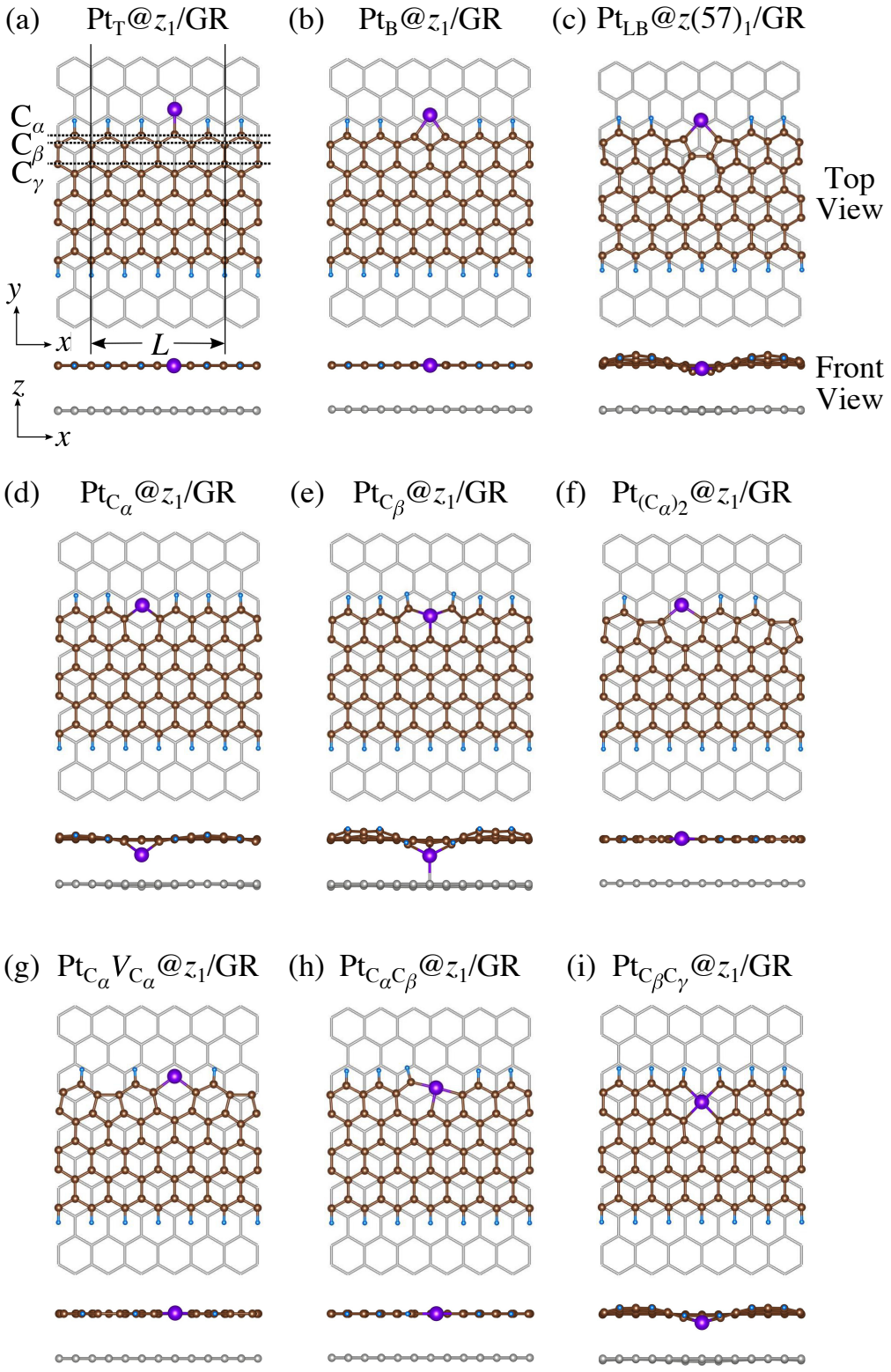

FIGURE 4.15: Optimized structures of Pt single-atom adsorption at the edges of mono-hydrogenated zGNRs with a graphene substrate. Purple, brown, and light blue spheres represent of Pt, C, H atoms, respectively and grey honeycomb corresponds to the graphene layer. The first, second, and third outermost C atoms are denoted as C_α, C_β, and C_γ, respectively. L indicates the periodicity of the ribbons along the edge direction.

Fig. 4.15. I optimize the structures and calculate the binding energy defined by

$$E_b = E_{\mathrm{Pt@}z\mathrm{GNR}} - E_{\mathrm{ref}} - E_{\mathrm{Pt}} - \Delta N_{\mathrm{C}} E_{\mathrm{GR}} - \frac{\Delta N_{\mathrm{H}}}{2} E_{\mathrm{H_2}}, \tag{4.5}$$

where $E_{\mathrm{Pt@}z\mathrm{GNR}}$ is the total energies of Pt adsorbed at zGNR (with and without graphene substrate) and E_{ref} is the total energy of the reference system, where I use perfect z_1 and perfect z_1 on graphene (z_1/GR) as references for the binding energies for Pt single-atom at z_1 and at z_1/GR, respectively. Calculated binding energies and corresponding CLSs are summarized in Table 4.4. We can see that difference of the binding energies with and without the substrate is insignificant, and in most cases, the substrate plays a role to stabilize the Pt single-atom adsorption, except for $\mathrm{Pt}_{\mathrm{C}_\beta}@z_1$. The most stable adsorption structure ($\mathrm{Pt}_{\mathrm{C}_\alpha}@z_1$) is unchanged and the binding energy difference is 0.16 eV upon inclusion of the substrate. The substrate does have an insignificant impact on the calculated core level shift, especially for the most stable $\mathrm{Pt}_{\mathrm{C}_\alpha}@z_1$. The change is −0.19 eV and

TABLE 4.3: The Gibbs free energy ($\Delta\Omega$) for Pt atom adsorption at aGNRs at $\mu_{\mathrm{C}} = E_{\mathrm{GR}}$ and $\mu_{\mathrm{H}} = E_{\mathrm{H_2}}$ and the corresponding core level shift (CLS).

	$\Delta\Omega(E_{\mathrm{GR}}, E_{\mathrm{H_2}})$ / eV		CLS / eV	
	a_1	a_2	a_1	a_2
$\mathrm{Pt}_{\mathrm{SB}}$	+0.67	−0.32	+0.63	+0.60
$\mathrm{Pt}_{\mathrm{LB}}$	−0.69	−0.94	+0.44	+0.77
$\mathrm{Pt}_{\mathrm{C}_\alpha}$	−0.35	−2.24	+1.33	+1.33
$\mathrm{Pt}_{\mathrm{C}_\beta}$	+0.91	−0.02	+1.56	+0.82
$\mathrm{Pt}_{\mathrm{C}_\gamma}$	+4.15	+3.00	+2.36	+2.33
$\mathrm{Pt}_{(\mathrm{C}_\alpha)_2}$	−0.57	−1.90	+0.17	+0.51
$\mathrm{Pt}_{\mathrm{C}_\alpha\mathrm{C}_\beta}$	+0.33	−1.40	+0.53	+0.77
$\mathrm{Pt}_{(\mathrm{C}_\beta)_2}$	+0.51	−1.17	−0.11	−0.74
$\mathrm{Pt}_{\mathrm{C}_\beta\ \mathrm{C}_\gamma}$	+1.48	−0.44	+0.05	−0.03
Expt.	—	—	+2.0±0.4[a]	

[a] Taken from Ref. 42.

TABLE 4.4: The binding energy (E_b) and the core level shift (CLS) of Pt single-atom adsorption at the edges of z_1 with and without substrate graphene (GR).

	E_b / eV		CLS / eV	
	w/o GR	w/ GR	w/o GR	w/ GR
$Pt_T@z_1$	−2.19	−2.32	−0.93	−0.94
$Pt_B@z_1$	−0.77	−0.88	+0.35	+0.34
$Pt_{LB}@z(57)_1$	+1.55	+1.70	+0.44	+0.51
$Pt_{C_\alpha}@z_1$	−2.58	−2.74	+1.43	+1.24
$Pt_{C_\beta}@z_1$	−0.44	−0.33	+1.37	+1.99
$Pt_{(C_\alpha)_2}@z_1$	−0.54	−0.58	+0.24	+0.21
$Pt_{C_\alpha V_{C_\alpha}}@z_1$	−0.32	−0.36	+0.54	−0.50
$Pt_{C_\alpha C_\beta}@z_1$	−2.19	−2.17	+0.81	+0.81
$Pt_{C_\beta C_\gamma}@z_1$	−0.22	−0.01	+0.82	+0.78
Expt.	—	—	+2.0±0.4[a]	

[a] Taken from Ref. 42.

TABLE 4.5: The binding energies (E_b) of the favorable Pt single-atom adsorption configurations at $\mu_C = E_{GR}$ and $\mu_H = E_{H_2}$.

Configuration	E_b/ eV
$Pt_T@z_1$	−2.19
$Pt_{C_\alpha}@z_1$	−2.58
$Pt_{C_\alpha C_\beta}@z_1$	−2.19
$Pt_T@z_2$	−0.72
$Pt_{C_\beta}@z_2$	−1.82
$Pt_{C_\beta C_\gamma}@z_2$	−1.13
$Pt_{LB}@a_1$	−0.61
$Pt_{(C_\alpha)_2}@a_1$	−0.49
$Pt_{(C_\alpha)_2}@a_2$	−1.82

the conclusion is unaltered.

4.3.5 Discussion

Experimentally, both zigzag and armchair edges coexist depending on the environment. Thus, it is desirable to compare the stability of single Pt atom adsorbed at the edges of zGNR and aGNR on the same footing, and investigate the favorable adsorption site when both edges are exposed. For this purpose, I define the

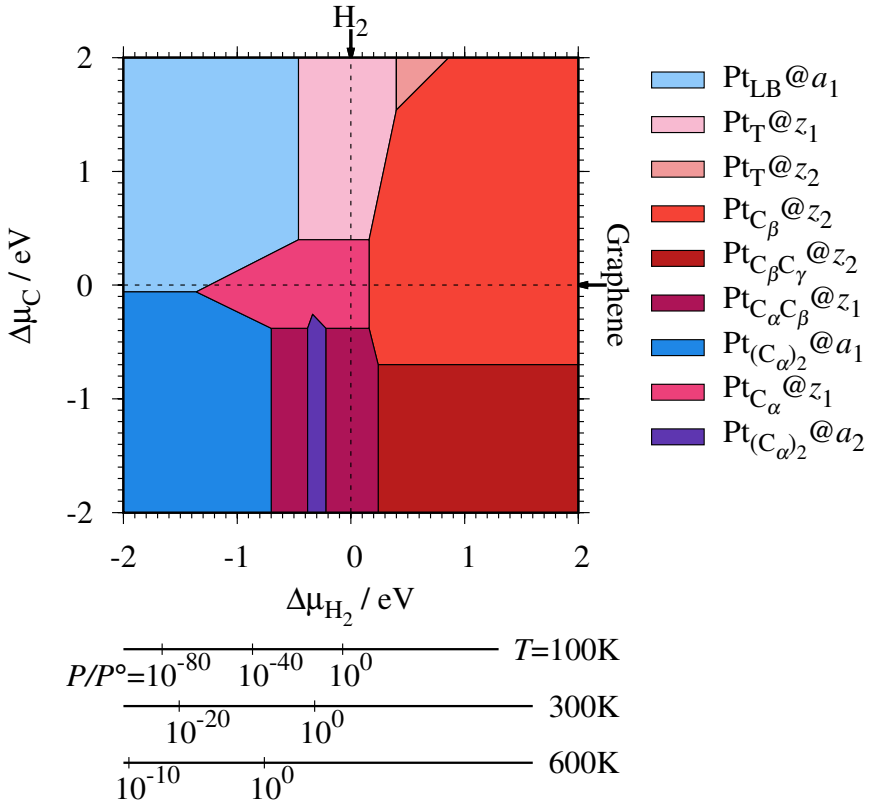

FIGURE 4.16: The binding energy for Pt single-atom adsorption at the edge of GNRs as a function of C and H_2 chemical potentials. The chemical potentials of C ($\Delta\mu_C$) and H_2 ($\Delta\mu_{H_2}$) are referenced to the total energies of graphene and gas-phase H_2 molecule at 0 K, respectively. The bottom axes show the corresponding H_2 chemical potentials at the absolute temperature T and partial pressure P (with $P^\circ = 1$ atm), $\mu_{H_2} = H^\circ(T) - H^\circ(0) - TS^\circ(T) + k_B T \ln(P/P^\circ)$, where the enthalpy H° and the entropy S° are obtained from Ref. 67.

binding energy of single Pt atom as

$$E_b(\mu_C, \mu_{H_2}) = E_{Pt@z(a)GNR} - E_{z(a)GNR} - E_{Pt} - \Delta N_C \mu_C - \frac{\Delta N_H}{2}\mu_{H_2}, \qquad (4.6)$$

where $E_{Pt@z(a)GNR}$ and $E_{z(a)GNR} - E_{Pt}$ are total energies of Pt adsorbed zGNR (aGNR) and pristine zGNR (aGNR), respectively. I note that the total energy of the most stable form of GNR at given μ_{H_2} is used as a reference ($E_{z(a)GNR}$, see also Fig. 4.4). E_b is an indicator of the strength of Pt single-atom adsorption and can be used to discuss the stability of Pt when both zGNR and aGNR are

present. Calculated E_b's as a function of μ_C and μ_{H_2} (phase diagram) are shown in Fig. 4.16 and those at $\mu_C = E_{GR}$ and $\mu_{H_2} = E_{H_2}$ are summarized in Table 4.5. I find that although aGNRs and Pt adsorbed aGNRs are thermodynamically more stable than zGNRs in terms of the Gibbs free energy (see Tables 4.3 and 4.2), Pt adsorption at the edges of zGNRs is more favorable. This suggests that when armchair and zigzag edges coexist, single Pt atoms prefer to adsorb at the zigzag edge. At around $\mu_C = E_{GR}$, $Pt_{C_\alpha}@z_1$ and $Pt_{C_\beta}@z_2$ are the most likely adsorption structures. In particular, the calculated CLS for the former agrees reasonably with the experimental one, and thus, I conclude that $Pt_{C_\alpha}@z_1$ is the most probable structure. Note that at -0.38 eV $\leq \Delta\mu_{H_2} \leq -0.22$ eV, $Pt(C_\alpha)_2@a_2$ appears as a stable structure among $Pt_{C_\alpha C_\beta}@z_1$. This narrow a_2 region corresponds to the region where intersections of formation energies are found (Fig. 4.4) and the stable (unstable) phase is determined by a subtle energy balance. As a result, a_2 becomes unstable, i.e., more reactive, and $Pt(C_\alpha)_2@a_2$ emerges as a stable adsorption structure. To determine the precise stability (boundary) when the different phases compete, however, more accurate and precise calculation of total energy is required. Nevertheless, the stability at around $\mu_C = E_{GR}$ and $\mu_{H_2} = E_{H_2}$ is unaffected, and I leave this a future work. Very recently, Yamazaki *et al.* propose the threefold-coordinated Pt atom at the edges of graphene flake based on x-ray photoelectron spectroscopy and DFT calculations [42]. In this case, the most stable $Pt_{C_\alpha}@z_1$ has twofold-coordinated Pt atom, which contradicts with them. On the other hand, the meta stable $Pt_{C_\beta}@z_1$ in our study, which has threefold-coordinated Pt atom, gives relatively large binding energy and reasonable CLS, and I do not rule out the possibility of the threefold-coordinated Pt atom at the

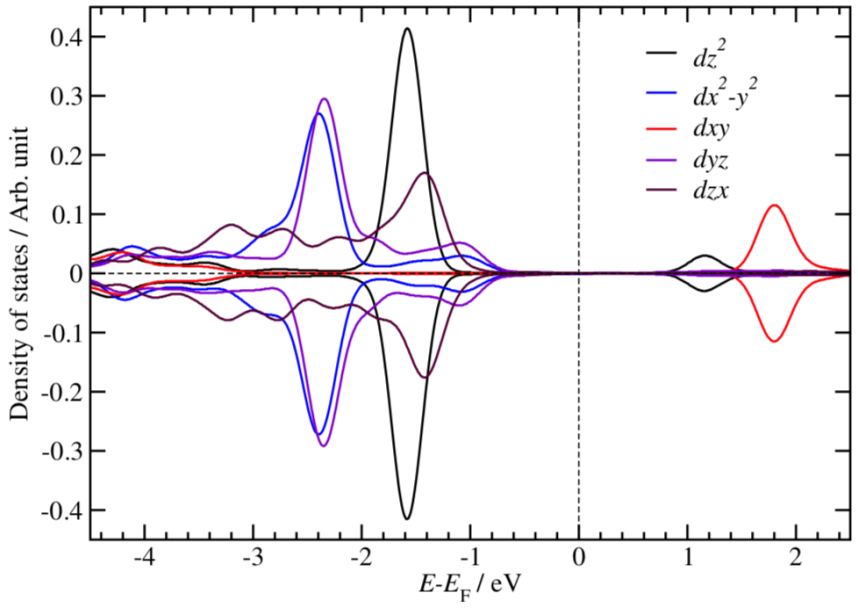

FIGURE 4.17: Densities of states projected onto the Pt d orbitals for $Pt_{C_\alpha}@z_1$. The energy origin is set to the Fermi level (E_F).

edge at this point. To resolve the discrepancy, I may need to employ the state-of-the-art theoretical method to calculate the absolute binding energy [68], and to investigate the models for the graphene edge, because Yamazaki *et al.* and I use different models (GNR and graphene flake, respectively) for the graphene edge. Nevertheless, I can conclude that the Pt single-atom adsorption takes place dominantly at the edge of graphene, and determination of more precise position and CLS will be done in near future.

Here, let us discuss the oxidation state of single Pt atom, as it is crucial to understanding of its catalytic activity. I calculated the density of states projected on the atomic orbitals of Pt for $Pt_{C_\alpha}@z_1$ (Fig. 4.17), which gives CLS in good agreement with the experimental value. I found that the Pt *d* states hybridize with the GNR state. In particular, the Pt d_{xy} state hybridizes strongly with C *sp* state and forms a fully unoccupied antibonding state, resulting in the formal oxidation state

TABLE 4.6: Bader charge (Q_{tot}) of the Pt atom and the deviation from the charge of isolated atom (ΔQ_{tot}) along with the calculated core level shift (CLS).

Structure	Q_{tot}	ΔQ_{tot}	CLS / eV
Pt/GR	9.94	−0.06	
Pt/V_1	9.51	−0.49	
Pt/V_2	9.24	−0.76	
$\mathrm{Pt_T}@z_0$	9.80	−0.20	−0.56
$\mathrm{Pt_B}@z_0$	9.69	−0.31	+0.44
$\mathrm{Pt_{C_\alpha}}@z_0$	9.62	−0.38	+0.50
$\mathrm{Pt_{C_\beta}}@z_0$	9.36	−0.54	+1.44
$\mathrm{Pt_{C_\beta C_\gamma}}@z_0$	9.23	−0.77	+1.67
$\mathrm{Pt_T}@z_1$	10.11	+0.11	−0.93
$\mathrm{Pt_{C_\alpha}}@z_1$	9.72	−0.28	+1.43
$\mathrm{Pt_{C_\beta C_\gamma}}@z_1$	9.45	−0.55	+0.81
$\mathrm{Pt_T}@z_1$	10.17	+0.17	+0.35
$\mathrm{Pt_{C_\beta}}@z_1$	9.59	−0.31	+1.42
$\mathrm{Pt_{C_\beta C_\gamma}}@z_1$	9.56	−0.34	+1.11
$\mathrm{Pt_{LB}}@a_1$	9.75	−0.25	+0.44
$\mathrm{Pt_{(C_\alpha)_2}}@a_1$	9.76	−0.24	+0.17
$\mathrm{Pt_{C_\alpha}}@a_2$	9.74	−0.26	+1.33
$\mathrm{Pt_{(C_\alpha)_2}}@a_2$	9.78	−0.22	+0.51

of 2+. I also performed the Bader charge analysis (Table 4.6), and found that it is not straightforward to assign the oxidation state of Pt only from the Bader charge analysis, especially those at the edges, because of the strong hybridization of Pt *d* states with GNR.

4.4 Conclusions

I present a systematic density functional theory-based thermodynamics study of Pt single-atom adsorption on graphene. I find that single Pt atoms adsorb more preferably at the graphene edge than on the bulk. Although pristine *a*GNR is thermodynamically more stable than *z*GNR under a wide range of hydrogen pressure, single Pt atoms preferably adsorb at the edge of hydrogenated *z*GNR. The

calculated core level shifts for the stable structures are in reasonable agreement with the experiment, supporting our findings. This study will be served as a basis for further investigation of the catalytic activity of single-atom catalysts based on single Pt atoms and graphene based nanostructures.

References

[1] P. Costamagna and S. Srinivasan, "Quantum jumps in the PEMFC science and technology from the 1960s to the year 2000: Part I. Fundamental scientific aspects," *J. Power Sources*, vol. 102, no. 1, pp. 242–252, 2001.

[2] H. Liu, C. Song, L. Zhang, J. Zhang, H. Wang, and D. P. Wilkinson, "A review of anode catalysis in the direct methanol fuel cell," *J. Power Sources*, vol. 155, no. 2, pp. 95–110, 2006.

[3] H. A. Gasteiger, N. M. Marković, P. N. Ross, and E. J. Cairns, "Electro-oxidation of small organic molecules on well-characterized Pt-Ru alloys," *Electrochim. Acta*, vol. 39, no. 11, pp. 1825–1832, 1994.

[4] A. Kabbabi, R. Faure, R. Durand, B. Beden, F. Hahn, J. M. Leger, and C. Lamy, "In situ FTIRS study of the electrocatalytic oxidation of carbon monoxide and methanol at platinum-ruthenium bulk alloy electrodes," *J. Electroanal. Chem.*, vol. 444, no. 1, pp. 41–53, 1998.

[5] B. N. Grgur, N. M. Marković, and P. N. Ross, "Electrooxidation of H_2, CO, and H_2/CO mixtures on a well-characterized Pt_70Mo_30 bulk alloy electrode," *J. Phys. Chem. B*, vol. 102, no. 14, pp. 2494–2501, 1998.

[6] H. A. Gasteiger, N. M. Marković, and P. N. Ross, "Structural effects in electrocatalysis: electrooxidation of carbon monoxide on Pt_3Sn single-crystal alloy surfaces," *Catal. Lett.*, vol. 36, no. 1, pp. 1–8, 1996.

[7] M. Watanabe, Y. Zhu, and H. Uchida, "Oxidation of CO on a Pt-Fe alloy electrode studied by surface enhanced infrared reflection-absorption spectroscopy," *J. Phys. Chem. B*, vol. 104, no. 8, pp. 1762–1768, 2000.

[8] H. Igarashi, T. Fujino, Y. Zhu, H. Uchida, and M. Watanabe, "CO tolerance of Pt alloy electrocatalysts for polymer electrolyte fuel cells and the detoxification mechanism," *Phys. Chem. Chem. Phys.*, vol. 3, pp. 306–314, 2001.

[9] J. Lai, R. Luque, and G. Xu, "Recent advances in the synthesis and electrocatalytic applications of platinum-based bimetallic alloy nanostructures," *ChemCatChem*, vol. 7, no. 20, pp. 3206–3228, 2015.

[10] T. Ozaki, Jun-Ichi andi Anahara, N. Kimura, and A. Oya, "Simultaneous doping of boron and nitrogen into a carbon to enhance its oxygen reduction activity in proton exchange membrane fuel cells," *Carbon*, vol. 44, no. 15, pp. 3358–3361, 2006.

[11] J.-I. Ozaki, N. Kimura, T. Anahara, and A. Oya, "Preparation and oxygen reduction activity of BN-doped carbons," *Carbon*, vol. 45, no. 9, pp. 1847–1853, 2007.

[12] P. H. Matter, E. Wang, M. Arias, E. J. Biddinger, and U. S. Ozkan, "Oxygen reduction reaction activity and surface properties of nanostructured nitrogen-containing carbon," *J. Mol. Catal. A: Chem.*, vol. 264, no. 1, pp. 73–81, 2007.

[13] X. Huang, Y. Wang, W. Li, and Y. Hou, "Noble metal-free catalysts for oxygen reduction reaction," *Sci. China Chem.*, vol. 60, pp. 1494–1507, 2017.

[14] F. Rodríguez-Reinoso, I. Rodríguez-Ramos, C. Moreno-Castilla, A. Guerrero-Ruiz, and J. D. López-González, "Platinum catalysts supported on activated carbons: I. preparation and characterization," *J. Catal.*, vol. 99, no. 1, pp. 171–183, 1986.

[15] T. Yoshitake, Y. Shimakawa, S. Kuroshima, H. Kimura, T. Ichihashi, Y. Kubo, D. Kasuya, K. Takahashi, F. Kokai, M. Yudasaka, and S. Iijima, "Preparation of fine platinum catalyst supported on single-wall carbon nanohorns for fuel cell application," *Phys. B*, vol. 323, no. 1, pp. 124–126, 2002.

[16] E. Yoo, T. Okata, T. Akita, M. Kohyama, J. Nakamura, and I. Honma, "Enhanced electrocatalytic activity of Pt subnanoclusters on graphene nanosheet surface," *Nano Lett.*, vol. 9, no. 6, pp. 2255–2259, 2009.

[17] J. Oh, T. Kondo, D. Hatake, Y. Iwasaki, Y. Honma, Y. Suda, D. Sekiba, H. Kudo, and J. Nakamura, "Significant reduction in adsorption energy of CO on platinum clusters on graphite," *J. Phys. Chem. Lett.*, vol. 1, no. 2, pp. 463–466, 2010.

[18] J. Nakamura, "The effect of a graphene support on the properties of Pt electrode catalysts in fuel cells," *Carbon*, vol. 85, pp. 443 – 444, 2015.

[19] K. Ding, A. Gulec, A. M. Johnson, N. M. Schweitzer, G. D. Stucky, L. D. Marks, and P. C. Stair, "Identification of active sites in CO oxidation and water-gas shift over supported Pt catalysts," *Science*, vol. 350, no. 6257, pp. 189–192, 2015.

[20] L. Xin, F. Yang, S. Rasouli, Y. Qiu, Z.-F. Li, A. Uzunoglu, C.-J. Sun, Y. Liu, P. Ferreira, W. Li, Y. Ren, L. A. Stanciu, and J. Xie, "Understanding Pt nanoparticle anchoring on graphene supports through surface functionalization," *ACS Catal.*, vol. 6, no. 4, pp. 2642–2653, 2016.

[21] H. C. Dam, N. T. Cuong, N. A. Tuan, Y.-T. Kim, H. T. Bao, T. Mitani, T. Ozaki, and H. Nagao, "Electronic structures of Pt clusters adsorbed on (5,5) single wall carbon nanotube," *Chem. Phys. Lett.*, vol. 432, no. 1, pp. 213–217, 2006.

[22] H. C. Dam, N. T. Cuong, A. Sugiyama, T. Ozaki, A. Fujiwara, T. Mitani, and S. Okada, "Substrate-mediated interactions of Pt atoms adsorbed on single-wall carbon nanotubes: Density functional calculations," *Phys. Rev. B*, vol. 79, p. 115426, 2009.

[23] K. Okazaki-Maeda, Y. Morikawa, S. Tanaka, and M. Kohyama, "Structures of Pt clusters on graphene by first-principles calculations," *Surf. Sci.*, vol. 604, no. 2, pp. 144–154, 2010.

[24] T. L. Pham, P. V. Dung, A. Sugiyama, N. D. Duc, T. Shimoda, A. Fujiwara, and D. H. Chi, "First principles study of the physisorption of hydrogen molecule on graphene and carbon nanotube surfaces adhered by Pt atom," *Comput. Mater. Sci.*, vol. 49, pp. S15–S20, 2010.

[25] M. Zhou, A. Zhang, Z. Dai, C. Zhang, and Y. P. Feng, "Greatly enhanced adsorption and catalytic activity of Au and Pt clusters on defective graphene," *J. Chem. Phys.*, vol. 132, no. 19, p. 194704, 2010.

[26] Y. Tang, Z. Yang, and X. Dai, "A theoretical simulation on the catalytic oxidation of CO on Pt/graphene," *Phys. Chem. Chem. Phys.*, vol. 14, pp. 16566–16572, 2012.

[27] I. Fampiou and A. Ramasubramaniam, "Binding of Pt nanoclusters to point defects in graphene: Adsorption, morphology, and electronic structure," *J. Phys. Chem. C*, vol. 116, no. 11, pp. 6543–6555, 2012.

[28] K. E. Hayes and H.-S. Lee, "First principles studies of the electronic properties and catalytic activity of single-walled carbon nanotube doped with Pt clusters and chains," *Chem. Phys.*, vol. 393, no. 1, pp. 96–106, 2012.

[29] J. Russell, P. Zapol, P. Král, and L. A. Curtiss, "Methane bond activation by Pt and Pd subnanometer clusters supported on graphene and carbon nanotubes," *Chem. Phys. Lett.*, vol. 536, pp. 9–13, 2012.

[30] A. Chutia, I. Hamada, and M. Tokuyama, "A theoretical insight on the interaction between Pt nanoparticles and hydroxylated graphene nanoflakes," *Surf. Sci.*, vol. 628, pp. 116–125, 2014.

[31] R. J. Gasper and A. Ramasubramaniam, "Density functional theory studies of the methanol decomposition reaction on graphene-supported Pt_{13} nanoclusters," *J. Phys. Chem. C*, vol. 120, no. 31, pp. 17408–17417, 2016.

[32] H. Shi, S. M. Auerbach, and A. Ramasubramaniam, "First-principles predictions of stucture-function relationships of graphene-supported platinum nanoclusters," *J. Phys. Chem. C*, vol. 120, no. 22, pp. 11899–11909, 2016.

[33] C. R. C. Rêgo, P. Tereshchuk, L. N. Oliveira, and J. L. F. Da Silva, "Graphene-supported small transition-metal clusters: A density functional theory investigation within van der Waals corrections," *Phys. Rev. B*, vol. 95, p. 235422, 2017.

[34] M. Mahmoodinia, P.-O. Åstrand, and D. Chen, "Tuning the electronic properties of single-atom Pt catalysts by functionalization of the carbon support material," *J. Phys. Chem. C*, vol. 121, no. 38, pp. 20802–20812, 2017.

[35] S. Sun, G. Zhang, N. Gauquelin, N. Chen, J. Zhou, S. Yang, W. Chen, X. Meng, D. Geng, M. N. Banis, R. Li, S. Ye, S. Knights, G. A. Botton, T.-K. Sham, and X. Sun, "Single-atom catalysis using Pt/graphene achieved through atomic layer deposition," *Sci. Rep.*, vol. 3, p. 1775, 2013.

[36] N. Cheng, S. Stambula, D. Wang, M. N. Banis, J. Liu, A. Riese, B. Xiao, R. Li, T.-K. Sham, L.-M. Liu, G. A. Botton, and X. Sun, "Platinum single-atom and cluster catalysis of the hydrogen evolution reaction," *Nat. Commun.*, vol. 7, p. 13638, 2016.

[37] S. Back, J. Lim, N.-Y. Kim, Y.-H. Kim, and Y. Jung, "Single-atom catalysts for CO_2 electroreduction with significant activity and selectivity improvements," *Chem. Sci.*, vol. 8, pp. 1090–1096, 2017.

[38] K.-J. Kong, Y. Choi, B.-H. Ryu, J.-O. Lee, and H. Chang, "Investigation of metal/carbon-related materials for fuel cell applications by electronic structure calculations," *Mater. Sci. and Eng. C*, vol. 26, no. 5, pp. 1207–1210, 2006.

[39] H. Wang, K. Li, Y. Cheng, Q. Wang, Y. Yao, U. Schwingenschlögl, X. Zhang, and W. Yang, "Interaction between single gold atom and the graphene edge: A study via aberration-corrected transmission electron microscopy," *Nanoscale*, vol. 4, pp. 2920–2925, 2012.

[40] J. Zhao, Q. Deng, S. M. Avdoshenko, L. Fu, J. Eckert, and M. H. Rümmeli, "Direct in situ observations of single Fe atom catalytic processes and anomalous diffusion at graphene edges," *Proceedings of the National Academy of Sciences*, vol. 111, no. 44, pp. 15641–15646, 2014.

[41] E. Kano, A. Hashimoto, and M. Takeguchi, "Opposite effects of Cu and Pt atoms on graphene edges," *Appl. Phys. Express*, vol. 10, no. 2, p. 025104, 2017.

[42] K. Yamazaki, Y. Maehara, C.-C. Lee, J. Yoshinobu, T. Ozaki, and K. Gohara, "Atomic structure and local electronic states of single Pt atoms dispersed on graphene," *J. Phys. Chem. C*, vol. 122, p. 27292, 2018.

[43] A. Hashimoto and M. Takeguchi, "In situ observation of Pt nanoparticles on graphene layers under high temperature using aberration-corrected transmission electron microscopy," *J. Electron Microsc.*, vol. 61, no. 6, pp. 409–413, 2012.

[44] T. Tomai, Y. Kawaguchi, S. Mitani, and I. Honma, "Pt sub-nano/nanoclusters stabilized at the edge of nanographene sheets and their catalytic performance," *Electrochim. Acta*, vol. 92, pp. 421–426, 2013.

[45] Y. Shen, Z. Zhang, K. Xiao, and J. Xi, "Electrocatalytic activity of Pt sub-nano/nanoclusters stabilized by pristine graphene nanosheets," *Phys. Chem. Chem. Phys.*, vol. 16, pp. 21609–21614, 2014.

[46] K. Reuter and M. Scheffler, "Composition and structure of the $RuO_2(110)$ surface in an o_2 and CO environment: Implications for the catalytic formation of CO_2," *Phys. Rev. B*, vol. 68, p. 045407, 2003.

[47] Y. Morikawa, K. Iwata, and K. Terakura, "Theoretical study of hydrogenation process of formate on clean and Zn deposited Cu(111) surfaces," *Appl. Surf. Sci.*, vol. 169–170, pp. 11–15, 2001.

[48] Y. Morikawa, H. Ishii, and K. Seki, "Theoretical study of n-alkane adsorption on metal surfaces," *Phys. Rev. B*, vol. 69, p. 041403, 2004.

[49] D. Vanderbilt, "Soft self-consistent pseudopotentials in a generalized eigenvalue formalism," *Phys. Rev. B*, vol. 41, pp. 7892–7895, 1990.

[50] I. Hamada, "Van der waals density functional made accurate," *Phys. Rev. B*, vol. 89, p. 121103, Mar 2014.

[51] Y. Hamamoto, I. Hamada, K. Inagaki, and Y. Morikawa, "Self-consistent van der Waals density functional study of benzene adsorption on Si(100)," *Phys. Rev. B*, vol. 93, p. 245440, Jun 2016.

[52] G. Román-Pérez and J. M. Soler, "Efficient implementation of a van der Waals density functional: Application to double-wall carbon nanotubes," *Phys. Rev. Lett.*, vol. 103, p. 096102, Aug 2009.

[53] J. Wu and F. Gygi, "A simplified implementation of van der Waals density functionals for first-principles molecular dynamics applications," *J. Chem. Phys.*, vol. 136, no. 22, p. 224107, 2012.

[54] J. P. Perdew, K. Burke, and M. Ernzerhof, "Generalized gradient approximation made simple," *Phys. Rev. Lett.*, vol. 77, pp. 3865–3868, Oct 1996.

[55] M. Callsen and I. Hamada, "Assessing the accuracy of the van der Waals density functionals for rare-gas and small molecular systems," *Phys. Rev. B*, vol. 91, p. 195103, May 2015.

[56] P. Y. Huang, C. S. Ruiz-Vargas, A. M. van der Zande, W. S. Whitney, M. P. Levendorf, J. W. Kevek, S. Garg, J. S. Alden, C. J. Hustedt, Y. Zhu, J. Park, P. L. McEuen, and D. A. Muller, "Grains and grain boundaries in single-layer graphene atomic patchwork quilts," *Nature*, vol. 469, p. 389, 2011.

[57] F. R. Eder, J. Kotakoski, U. Kaiser, and J. C. Meyer, "A journey from order to disorder atom by atom transformation from graphene to a 2D carbon glass," *Sci. Rep.*, vol. 4, p. 4060, 2014.

[58] T. Wassmann, A. P. Seitsonen, A. M. Saitta, M. Lazzeri, and F. Mauri, "Structure, stability, edge states, and aromaticity of graphene ribbons," *Phys. Rev. Lett.*, vol. 101, p. 096402, 2008.

[59] S. Okada and A. Oshiyama, "Magnetic ordering in hexagonally bonded sheets with first-row elements," *Phys. Rev. Lett.*, vol. 87, p. 146803, Sep 2001.

[60] H. Lee, Y.-W. Son, N. Park, S. Han, and J. Yu, "Magnetic ordering at the edges of graphitic fragments: Magnetic tail interactions between the edge-localized states," *Phys. Rev. B*, vol. 72, p. 174431, Nov 2005.

[61] S. A. Wella, H. Sawada, N. Kawaguchi, F. Muttaqien, K. Inagaki, I. Hamada, Y. Morikawa, and Y. Hamamoto, "Hybrid image potential states in molecular overlayers on graphene," *Phys. Rev. Mater.*, vol. 1, p. 061001, Nov 2017.

[62] Y. Baskin and L. Meyer, "Lattice constants of graphite at low temperatures," *Phys. Rev.*, vol. 100, pp. 544–544, 1955.

[63] E. Pehlke and M. Scheffler, "Evidence for site-sensitive screening of core holes at the Si and Ge (001) surface," *Phys. Rev. Lett.*, vol. 71, pp. 2338–2341, 1993.

[64] Y. Morikawa, T. Hayashi, C. Liew, and H. Nozoye, "First-principles theoretical study of alkylthiolate adsorption on Au(111)," *Surf. Sci.*, vol. 507-510, pp. 46 – 50, 2002.

[65] S. García-Gil, A. García, and P. Ordejón, "Calculation of core level shifts within DFT using pseudopotentials and localized basis sets," *Eur. Phys. J. B*, vol. 85, no. 7, p. 239, 2012.

[66] F. A. Kröger and H. J. Vink in *Relations between the Concentrations of Imperfections in Crystalline Solids* (F. Seitz and D. Turnbull, eds.), vol. 3 of *Solid State Physics*, pp. 307–435, Academic Press, 1956.

[67] M. W. Chase, Jr., C. A. Davies, J. R. Downey ,Jr., D. J. Frurip, R. A. McDonald, and A. N. Syverud, "Janaf thermochemical tables," *J. Phys. Chem. Ref. Data, Supplement I*, vol. 14, 1985.

[68] T. Ozaki and C.-C. Lee, "Absolute binding energies of core levels in solids from first principles," *Phys. Rev. Lett.*, vol. 118, p. 026401, Jan 2017.

Chapter 5

Atomic and Molecular Adsorption on Single Platinum Atom at the Graphene Edge

5.1 Background

As explained in Chapter 4, I have systematically investigated the the adsorption state of the Pt atom at the edge of graphene nanoribbons [1]. Via density functional theory based thermodynamics, I find some favorable adsorption states, while their catalytic activity are yet to be examined. Hence, in recent study, I determine atomic and molecular adsorptions on those structures. Based on these adsorption energies, I examine the catalytic activities of those structure using kinetic models proposed in Ref. 2 for CO electro-oxidation and in Ref. 3 for oxygen reduction reaction.

5.2 Computational Details

All the periodic DFT calculations are performed by using the STATE code [4, 5]. Ultrasoft pseudopotentials [6] are used to describe electron-ion interactions. Wave functions and the augmentation charge are expanded in terms of a plane wave basis set with cutoff energies of 36 Ry and 400 Ry, respectively. A recent van der Waals density functional, rev-vdW-DF2 [7], is used as the exchange-correlation energy functional, which is implemented [8] in the STATE code with an efficient algorithm [9, 10]. The edge of graphene is modeled by using graphene nanoribbon (GNR), and the models of a single Pt atom supported by GNRs are adopted from the previous study [1] with the same computational settings.

Figure 5.1 displays the ten different Pt adsorbed GNR (Pt@GNR) structures considered in this work, which are thermodynamically stable under a range of hydrogen and carbon chemical potentials. In this study, I examine the adsorption of hydrogen (H), oxygen (O), carbon (C), and nitrogen (N) atoms and carbon monooxide (CO), hydroxyl (OH), nitric oxide (NO), and water (H_2O) molecules and evaluate the adsorption energy defined by

$$E_{\mathrm{ads}} = -E_{\mathrm{adsorbate/Pt@GNR}} + E_{\mathrm{adsorbate}} + E_{\mathrm{Pt@GNR}}, \tag{5.1}$$

where $E_{\mathrm{adsorbate/Pt@GNR}}$, $E_{\mathrm{adsorbate}}$, and $E_{\mathrm{Pt@GNR}}$ are the total energies of adsorbed system, gas phase atom/molecule, and Pt@GNR, respectively. With this definition, positive E_{ads} indicates that adsorption state is more stable than the isolated ones.

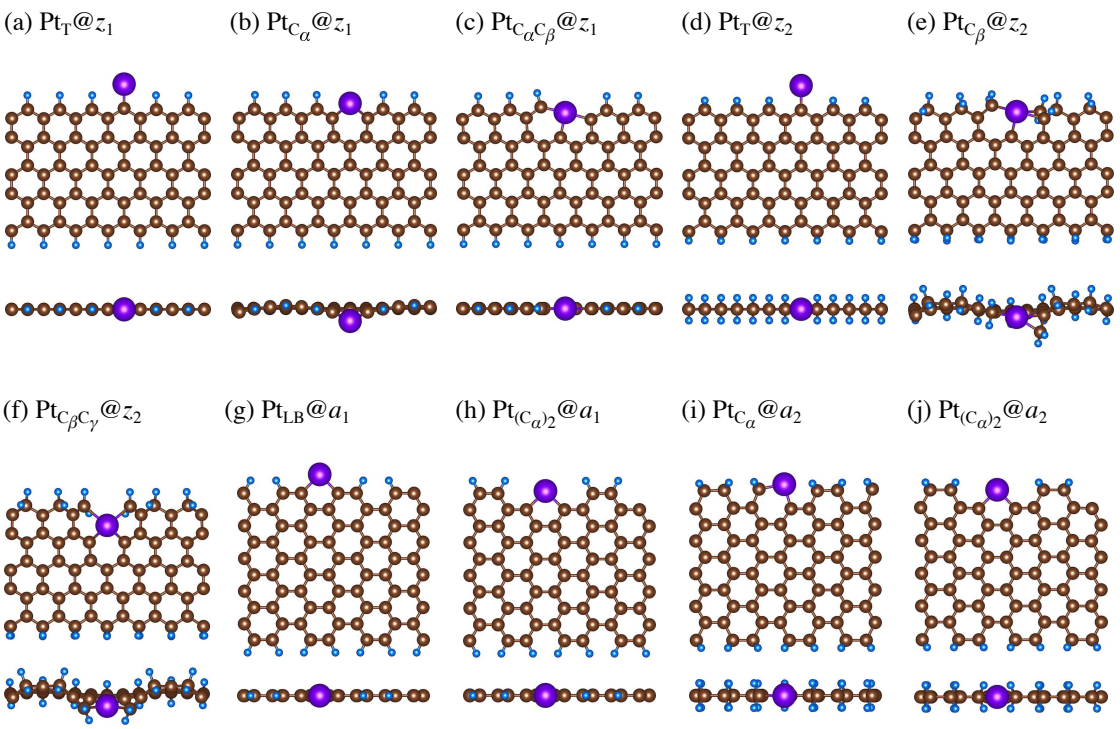

FIGURE 5.1: Structures of Pt@GNRs used in the present work. Adopted from Ref. 1.

For comparison, I also calculate the adsorption energies of all the atoms and molecules considered on a Pt(111) surface. In this case, the Perdew-Burke-Ernzerhof (PBE) [11] generalized gradient approximation (GGA) exchange-correlation functional is also used for comparison with the literature. The Pt(111) surface is modeled by a 6-layer slab with the vacuum thickness of ∼16 Å. Theoretical lattice constant of 3.95 Å (3.93 Å) obtained using the PBE (rev-vdW-DF2) functional, which are in good agreement with the experimental value of 3.92 Å, is used to construct the slab. Brillouin zone integration is performed using a Γ-centered 8×8 k-point set. I investigate the stability of all the adsorbates on high symmetry sites, including atop, hcp hollow, and fcc hollow sites. The structures are fully relaxed until the forces acting on the atoms becomes smaller than 5.14×10^{-2}

eV/Å (1×10^{-3} Hartree/Bohr). The adsorption energy for Pt(111) is defined by

$$E_{\mathrm{ads}} = -E_{\mathrm{adsorbate/Pt}} + E_{\mathrm{adsorbate}} + E_{\mathrm{Pt}}, \tag{5.2}$$

where $E_{\mathrm{adsorbate/Pt}}$, $E_{\mathrm{adsorbate}}$, and E_{Pt} are the total energies of the atom/molecule adsorbed Pt(111), gas phase atom/molecule, and Pt(111), respectively. Spin polarization is taken into account for all the systems. For selected systems, zero-point energy (ZPE) correction is taken into account. Contribution from the substrate is not taken into account in these cases.

5.3 Results and Discussion

5.3.1 Atoms and Molecules Adsorption

I first calculate the adsorption energies of atoms and molecules on Pt(111) to confirm the accuracy of my computational settings. The adsorption energies for high symmetry sites are summarized in Table 5.1. For all the atoms considered, they prefer to adsorb at the three-fold coordination site, namely, the fcc hollow site. The rev-vdW-DF2 tends to give larger adsorption energy than PBE. I note that except for H atom, the atomic adsorption energy difference between atop and (hpc and fcc) hollow sites is large, indicating the importance of the coordination number of the adsorbates to their adsorption energies. In the case of H atom, the most stable adsorption site is the fcc hollow site indeed, but adsorption energy differences among the high symmetry sites are significantly small [$\sim$60 ($\sim$30) meV

TABLE 5.1: Calculated adsorption energies of the atoms and molecules on Pt(111) with PBE and rev-vdW-DF2. The values in bold indicate the largest adsorption energies among the adsorption sites considered. Zero point energy is not considered. The unit of energy is eV.

	PBE			rev-vdW-DF2		
	atop	hpc	fcc	atop	hpc	fcc
H	2.74	2.77	**2.81**	3.00	2.98	**3.02**
O	2.64	3.75	**4.22**	2.95	4.08	**4.56**
C	4.79	7.02	**7.16**	5.41	7.57	**7.71**
N	3.41	5.65	**5.90**	3.85	6.08	**6.33**
CO	**1.70**	1.93	1.93	**1.80**	2.05	2.06
OH	**2.17**	1.64	1.93	**2.42**	1.94	2.22
NO	1.49	1.82	**2.01**	1.72	2.09	**2.28**
H_2O	**0.21**	0.15	0.17	**0.38**	0.36	0.37

from PBE (rev-vdW-DF2)]. This is in line with previous studies [12, 13, 14, 15, 16, 17, 18]. For the CO adsorption on Pt(111), it is well-known that semilocal DFT and vdW-DF fails to predict top site adsorption on Pt(111) as observed in the experiment [19, 14, 20]. Therefore, in spite of the fact that the fcc hollow site is the most favorable site at the PBE and vdW-DF levels of theory, here the atop site is considered as the adsorption site of CO on Pt(111) for comparison. I note that the original vdW-DF and vdW-DF2 predict correct top site adsorption of CO on Pt(111) [21, 22, 23, 24], at the expense of the C-O bond length and presumably of the CO-Pt bond length. For the OH adsorption, the oxygen atom is bound to an atop site, while the OH bond is slightly tilted with respect to the surface. For NO and H_2O molecules, fcc hollow and atop sites become the most favorable sites, respectively. The H_2O has the smallest adsorption energy relative to other atoms and molecules considered here. Overall, PBE and rev-vdW-DF2 predict the same adsorption sites for atoms and molecules, and for the weakly chemisorption system, i.e., H_2O, rev-vdW-DF2 gives larger adsorption energy, as

TABLE 5.2: Calculated adsorption energy (E_{ads}) in eV and site preference of the atomic and molecular adsorption on Pt(111), along with the theoretical values in the literature. For H (O) adsorption, E_{ads} is also calculated by taking a half energy of the gas phase H_2 (O_2) molecule as a reference and provided in square brackets.

	Preferred Site	Present work		Other work
		PBE	rev-vdW-DF2	
H	fcc	2.81	3.02	2.57[u], 2.71[n], 2.74[i]
		[0.54]	[0.51]	[0.48][m], [0.50][h], [0.52][b], [0.53][a], [0.54][r]
O	fcc	4.22	4.56	3.27[u], 3.73[o], 3.87[i], 4.30[c], 4.36[m], 4.61[d]
		[1.92]	[2.09]	[1.29][b], [1.30][r], [1.50][t]
C	fcc	7.16	7.71	6,27[u], 6.75[i], 6.99[v], 7.32[s], 7.34[e]
N	fcc	5.90	6.33	3.91[u], 4.35[i], 4.81[j]
CO	atop	1.70	1.80	1.32[u], 1.52[k], 1.53[l], 1.69[f], 1.71[b], 1.72[i], 1.80[w], 1.81[q], 1.87[t]
OH	atop-tilted	2.23	2.51	1.68[u], 2.09[q], 2.12[o], 2.13[i], 2.21[c], 2.27[p], 2.33[r], 2.62[g]
NO	fcc	2.01	2.28	1.27[u], 1.85[i], 1.93[j]
H_2O	atop	0.21	0.38	0.27[n], 0.33[r]

[a] Ref. 12: 1/4 ML, 5 layers, PBE, STATE
[b] Ref. 14: 1/4 ML, 6 layers, PBE, VASP
[c] Ref. 28: 1/9 ML, 3 layers, PBE, VASP
[d] Ref. 30: 1/4 ML, 7 layers, PBE, VASP
[e] Ref. 32: 1/4 ML, 5 layers, PBE, VASP
[f] Ref. 34: 1/9 ML, 6 layers, PBE, VASP
[g] Ref. 35: 1/9 ML, 4 layers, PBE, DACAPO
[h] Ref. 36: 1/4 ML, 3 layers, PBE, STATE
[i] Ref. 17: 1/4 ML, 5 layers, PW91, DACAPO
[j] Ref. 37: 1/4 ML, 4 layers, PW91, VASP
[k] Ref. 22: 1/9 ML, 5 layers, optB86b, VASP
[l] Ref. 22: 1/9 ML, 5 layers, BEEF, VASP
[m] Ref. 13: 1/4 ML, 5 layers, PW91, VASP
[n] Ref. 15: 1/9 ML, 3 layers, PW91, DACAPO
[o] Ref. 29: 1/9 ML, 3 layers, PW91, DACAPO
[p] Ref. 31: 1/4 ML, 4 layers, PW91, CASTEP
[q] Ref. 33: 1/4 ML, 3 layers, PW91, DACAPO
[r] Ref. 16: 1/4 ML, 5 layers, PW91, VASP
[s] Ref. 32: 1/4 ML, 5 layers, PW91, VASP
[t] Ref. 14: 1/4 ML, 6 layers, optB86b, VASP
[u] Ref. 17: 1/4 ML, 5 layers, RPBE, DACAPO
[v] Ref. 32: 1/4 ML, 5 layers, RPBE, VASP
[w] Ref. 22: 1/9 ML, 5 layers, PBE, VASP

the vdW interaction plays an important role in the water adsorption [25, 26, 27]. All the site preferences, adsorption energies, and comparison with those in the literature are summarized in Table 5.2, and geometries obtained in this work are listed in Table 5.3.

Next, I examine the atomic and molecular adsorptions on all the Pt@GNRs considered in this work. Calculated adsorption energies and geometries are summarized in Table 5.4 and Table 5.5, respectively, and some optimized structures are shown

TABLE 5.3: Geometrical parameters of the atomic and molecular adsorption on Pt(111). $Z_{\mathrm{A-Pt}}$ is the vertical distance between the adsorbate and the Pt atom underneath. ΔZ_{Pt} is the vertical displacement of Pt atom beanth the adsorbate with respect to that of the clean surface. $d_{\mathrm{Pt-Pt}}$ is the average distance between two adjacent Pt atoms beneath the adsorbate. $d_{\mathrm{A-B}}$ is the bond length of the molecule considered. All the values are obtained using PBE (rev-vdW-DF2) functionals. The unit of the length is Å.

	Pt(111)				Gas Phase
	$Z_{\mathrm{A-Pt}}$	ΔZ_{Pt}	$d_{\mathrm{Pt-Pt}}$	$d_{\mathrm{A-B}}$	$d_{\mathrm{A-B}}$
H	0.86 (0.88)	0.05 (0.05)	2.85 (2.83)	-	-
O	1.15 (1.17)	0.13 (0.11)	2.88 (2.87)	-	-
C	0.90 (0.92)	0.18 (0.17)	2.90 (2.89)	-	-
N	1.01 (1.03)	0.16 (0.15)	2.87 (2.85)	-	-
CO	1.83 (1.84)	0.23 (0.20)	2.80 (2.78)	1.16 (1.16)	1.15 (1.15)
OH	1.98 (1.98)	0.15 (0.13)	2.78 (2.77)	0.98 (0.98)	0.99 (0.99)
NO	1.24 (1.22)	0.16 (0.15)	2.85 (2.84)	1.22 (1.26)	1.17 (1.17)
H_2O	2.43 (2.36)	0.03 (0.02)	2.79 (2.78)	0.98 (0.98)	0.97 (0.98)

in Figs. 5.3–5.10. In general, atomic adsorption on Pt@GNRs is weaker than that on Pt(111). It is attributed to the lower coordination number of the adsorbates on Pt@GNRs, which is similar to the case of atomic adsorption on the atop site of Pt(111). In the case of CO on Pt@GNR, weaker adsorption (i.e., smaller adsorption energy) is highly desirable to avoid the CO poisoning, which often occurs at the Pt surfaces. Although CO strongly adsorbs on most Pt@GNRs considered, CO on $\mathrm{Pt}_{\mathrm{C}_\alpha}@z_1$, $\mathrm{Pt}_{\mathrm{C}_\beta}@z_2$, and $\mathrm{Pt}_{\mathrm{C}_\beta\mathrm{C}_\gamma}@z_2$ have smaller adsorption energies than that on Pt(111). For $\mathrm{Pt}_{\mathrm{C}_\beta\mathrm{C}_\gamma}@z_2$ [see Fig. 5.1(f)], the single Pt atom adsorbs more deeply at the edge of GNR. In this case, hydrogen atoms around the Pt atom sterically hinder the adsorbates, making CO adsorption at the Pt atom rather difficult. In addition, deformation of GNR upon adsorption [Fig. 5.7(f)] makes the system less stable, resulting in the smaller adsorption energy.

To better understand the trend in the CO adsorption, I plot the Pt $4f$ core level

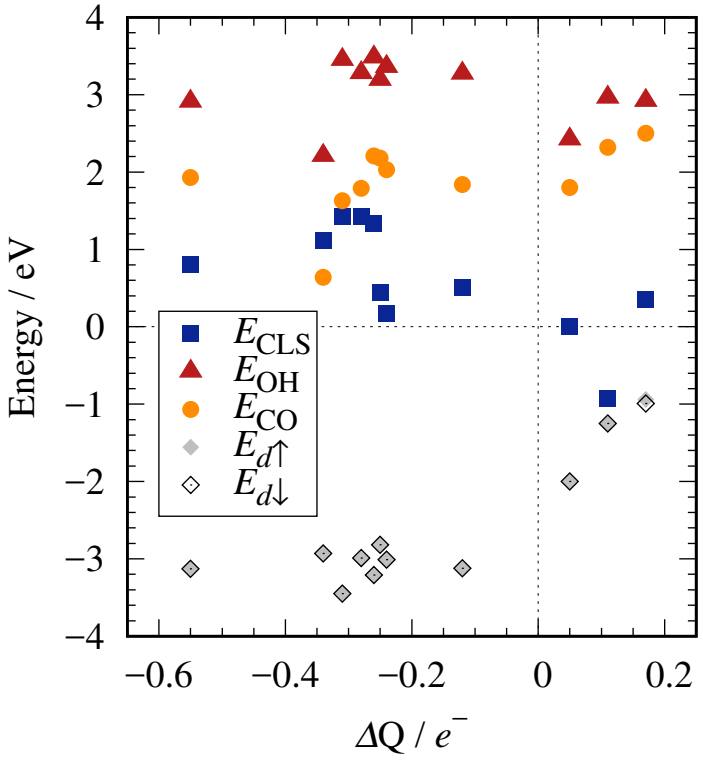

FIGURE 5.2: The Pt $4f$ core level shift (E_{CLS}), the OH adsorption energy (E_{OH}), the CO adsorption energy (E_{CO}), and the d-band center ($E_{d\uparrow}$ and $E_{d\downarrow}$ for spin-up and spin-down states, respectively) as functions of the differential Bader charge (ΔQ) for all the Pt@GNRs considered, including Pt(111). ΔQ is defined as the difference charge with respect to the isolated Pt atom. The ΔQ and E_{CLS} are obtained in our previous work [1].

shift (E_{CLS}), the Pt d band center (E_d), and the adsorption energy of CO (E_{CO}) as functions of charge (Fig. 5.2). It was found that E_{CO} gets stronger as the Pt atom gets more negative (more electron or more positive differential Bader charge ΔQ), because a negatively charged system gives shallower electrostatic potential, resulting in the shallower E_d, and thus, larger E_{CO} [38].

In the case of OH on Pt@GNR, adsorption energies for all the Pt@GNRs considered here are larger than that on Pt(111), except for $\mathrm{Pt}_{\mathrm{C}_\beta\mathrm{C}_\gamma}z_2$ [Fig. 5.8(f)]. For OH adsorption on $\mathrm{Pt}_{\mathrm{C}_\beta\mathrm{C}_\gamma}z_2$, steric hindrance from terminating hydrogen atoms and deformation of graphene upon adsorption make the adsorption less stable, similar

TABLE 5.4: Calculated adsorption energy (E_{ads}), in eV, of the atoms and molecules adsorption on Pt@GNRs calculated only using rev-vdW-DF2. For H (O) adsorption, E_{ads} is also calculated by taking a half energy of the gas phase H_2 (O_2) molecule as a reference. The values are provided in square brackets.

	H	O	C	N	CO	OH	NO	H_2O
$Pt_T@z_1$	2.91 [0.40]	3.72 [1.24]	5.19	4.35	2.32	2.96	2.65	0.88
$Pt_{C_\alpha}@z_1$	2.30 [−0.21]	3.80 [1.33]	4.03	3.82	1.79	3.28	1.58	0.56
$Pt_{C_\alpha C_\beta}@z_1$	2.30 [−0.21]	3.47 [0.99]	4.13	3.74	1.93	2.91	1.69	0.73
$Pt_T@z_2$	3.11 [0.60]	4.33 [1.86]	5.40	4.55	2.50	2.92	2.85	0.77
$Pt_{C_\beta}@z_2$	2.74 [0.23]	3.61 [1.13]	5.22	3.57	1.63	3.45	1.47	0.58
$Pt_{C_\beta C_\gamma}@z_2$	2.70 [0.19]	4.18 [1.70]	4.72	5.52	0.64	2.21	0.92	0.27
$Pt_{LB}@a_1$	1.94 [−0.57]	3.90 [1.43]	5.18	4.33	2.18	3.19	1.93	0.45
$Pt_{(C_\alpha)_2}@a_1$	2.00 [−0.51]	4.00 [1.53]	5.38	4.50	2.03	3.36	2.06	0.37
$Pt_{C_\alpha}@a_2$	2.45 [−0.06]	3.98 [1.51]	4.47	4.22	2.21	3.48	2.08	0.61
$Pt_{(C_\alpha)_2}@a_2$	2.49 [−0.02]	3.91 [1.44]	5.15	4.32	1.84	3.27	1.92	0.41
Pt(111)	3.02 [0.51]	4.56 [2.09]	7.71	6.33	1.80	2.42	2.28	0.38

to CO. Contrary to the CO adsorption, OH adsorption energy decreases as ΔQ increases (Pt gets more negative) (Fig. 5.2). I presume that decrease in OH adsorption energy is due to the repulsive interaction between the occupied OH orbital and Pt 5*d* states. In the case of NO, adsorption energies are smaller on Pt@GNRs. Only NO on $Pt_T@z_1$ and $Pt_T@z_2$ show larger adsorption energies. H_2O adsorption is similar to the OH adsorption on Pt@GNRs: H_2O on most PtGNRs show a tendency of stronger binding than on Pt(111), except for that on $Pt_{C_\beta C_\gamma}@z_2$. Again, its small adsorption energy originates from the steric hindrance with the terminating hydrogen atoms and large deformation of the $Pt_{C_\beta C_\gamma}@z_2$ upon adsorption [Fig. 5.10(f)].

TABLE 5.5: Geometrical parameters of the atomic and molecular adsorption on Pt@GNRs. $d_{\mathrm{A-B}}$ is the bond length between atoms A and B. Geometry optimization was performed using the rev-vdW-DF2 functional.

	H	O	C	N	CO		OH		NO		H_2O	
	$d_{\mathrm{Pt-H}}$	$d_{\mathrm{Pt-O}}$	$d_{\mathrm{Pt-C}}$	$d_{\mathrm{Pt-N}}$	$d_{\mathrm{Pt-C}}$	$d_{\mathrm{C-O}}$	$d_{\mathrm{Pt-O}}$	$d_{\mathrm{O-H}}$	$d_{\mathrm{Pt-N}}$	$d_{\mathrm{N-O}}$	$d_{\mathrm{Pt-O}}$	$d_{\mathrm{O-H}}$
$\mathrm{Pt_T}@z_1$	1.65	1.78	1.73	1.75	1.86	1.17	1.93	0.98	1.78	1.18	2.16	0.97
$\mathrm{Pt_{C_\alpha}}@z_1$	1.66	1.78	1.80	1.74	1.91	1.16	1.94	0.98	1.87	1.19	2.23	0.98
$\mathrm{Pt_{C_\alpha C_\beta}}@z_1$	1.61	1.80	1.78	1.73	1.90	1.16	1.99	0.98	1.84	1.18	2.25	0.98
$\mathrm{Pt_T}@z_2$	1.54	1.77	1.73	1.75	1.85	1.17	1.95	0.98	1.78	1.18	2.12	0.97
$\mathrm{Pt_{C_\beta}}@z_2$	1.64	1.90	1.86	1.90	1.91	1.17	2.02	0.98	2.01	1.21	2.30	0.98
$\mathrm{Pt_{C_\beta C_\gamma}}@z_2$	1.86	2.03	2.07	2.07	1.93	1.17	1.97	0.98	1.94	1.19	3.32	0.99
$\mathrm{Pt_{LB}}@a_1$	1.69	1.76	1.69	1.71	1.91	1.16	1.94	0.98	1.86	1.20	2.25	0.98
$\mathrm{Pt_{(C_\alpha)_2}}@a_1$	1.70	1.77	1.69	1.71	1.85	1.20	1.94	0.98	1.85	1.20	2.30	0.98
$\mathrm{Pt_{C_\alpha}}@a_2$	1.65	1.78	1.76	1.73	1.89	1.17	1.95	0.98	1.83	1.19	2.30	0.98
$\mathrm{Pt_{(C_\alpha)_2}}@a_2$	1.63	1.77	1.69	1.72	1.90	1.17	1.95	0.98	1.84	1.20	2.26	0.98
Pt(111)	1.86	2.02	1.91	1.94	1.84	1.16	1.98	0.98	2.07	1.22	2.36	0.98

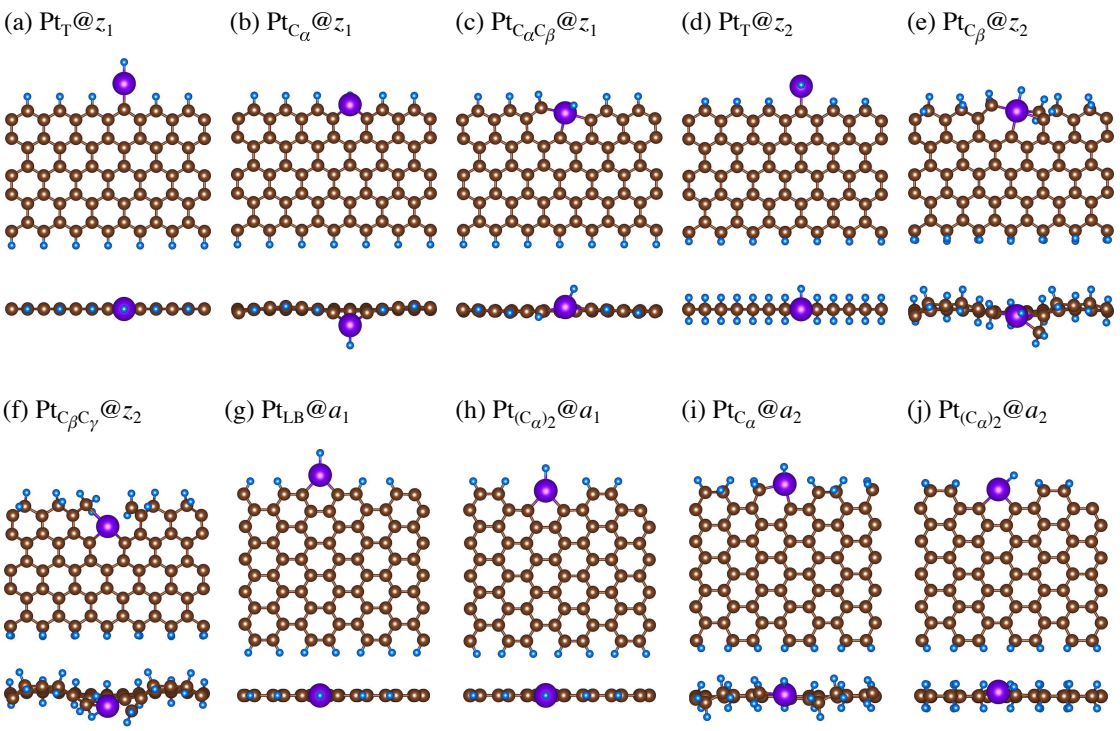

FIGURE 5.3: Optimized structures of H adsorption on Pt@GNRs. Purple, brown, and light blue spheres represent of Pt, C, and H atoms, respectively.

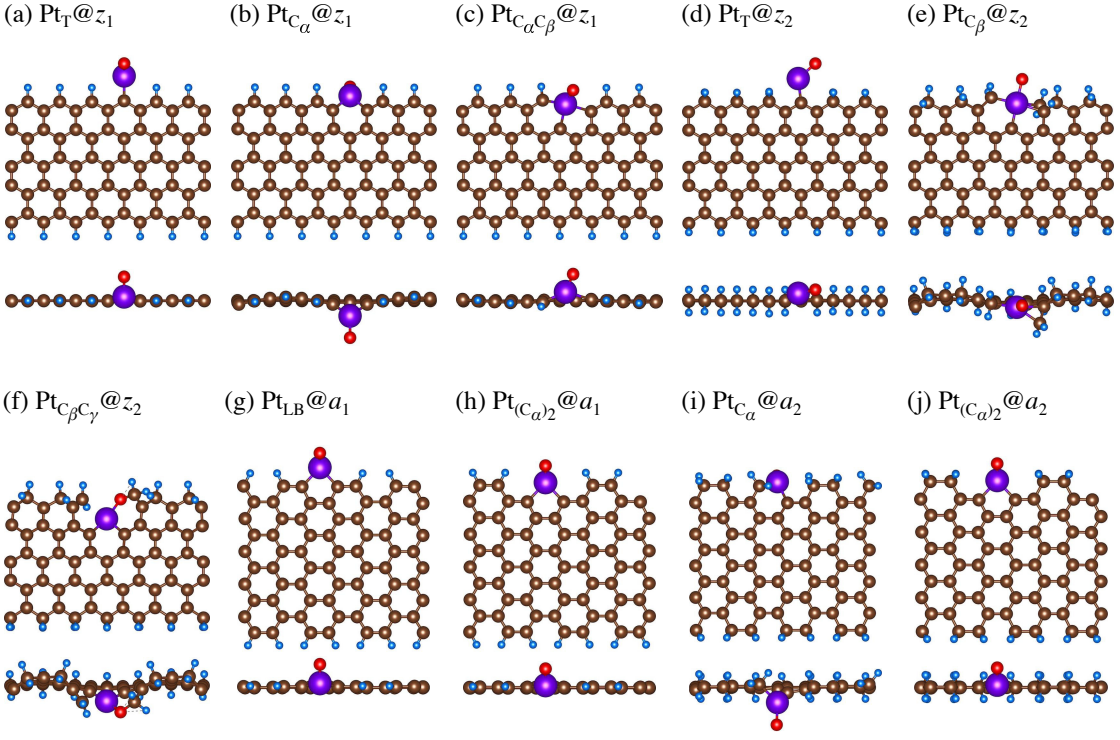

FIGURE 5.4: Optimized structures of O adsorption on Pt@GNRs. Purple, brown, light blue, and red spheres represent of Pt, C, H and O atoms, respectively.

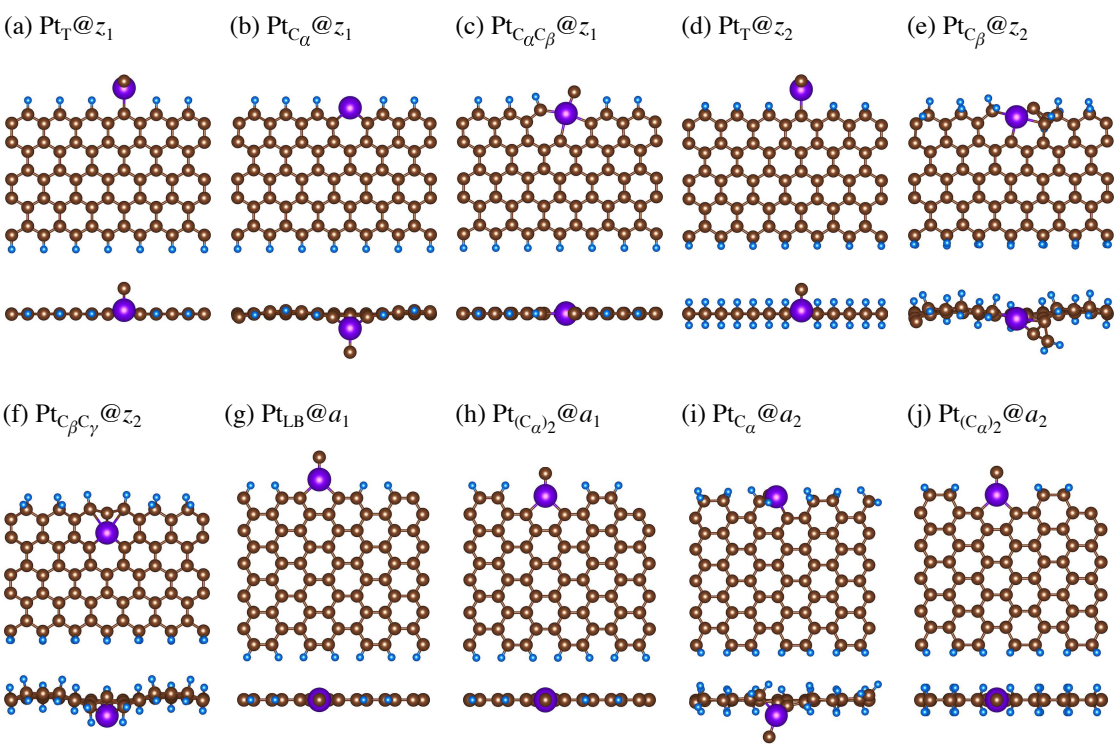

FIGURE 5.5: Optimized structures of C adsorption on Pt@GNRs. Purple, brown, and light blue spheres represent of Pt, C, and H atoms, respectively.

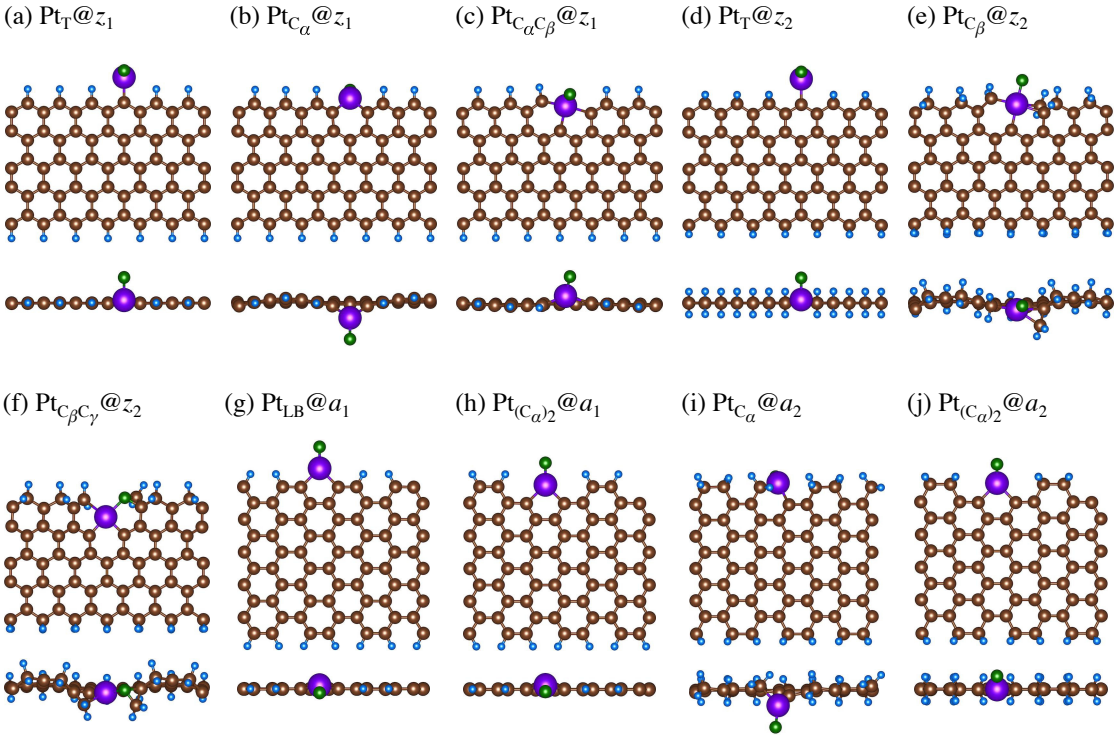

FIGURE 5.6: Optimized structures of N adsorption on Pt@GNRs. Purple, brown, light blue and green spheres represent of Pt, C, H and N atoms, respectively.

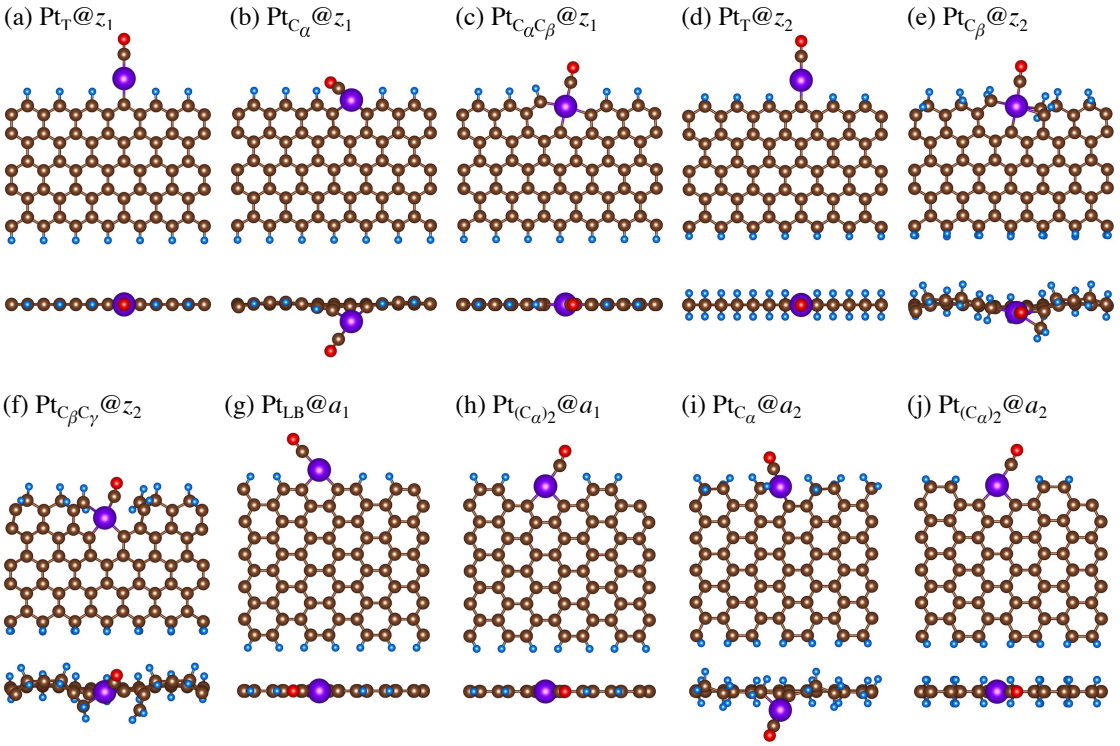

FIGURE 5.7: Optimized structures of CO adsorption on Pt@GNRs. Purple, brown, light blue, and red spheres represent of Pt, C, H and O atoms, respectively.

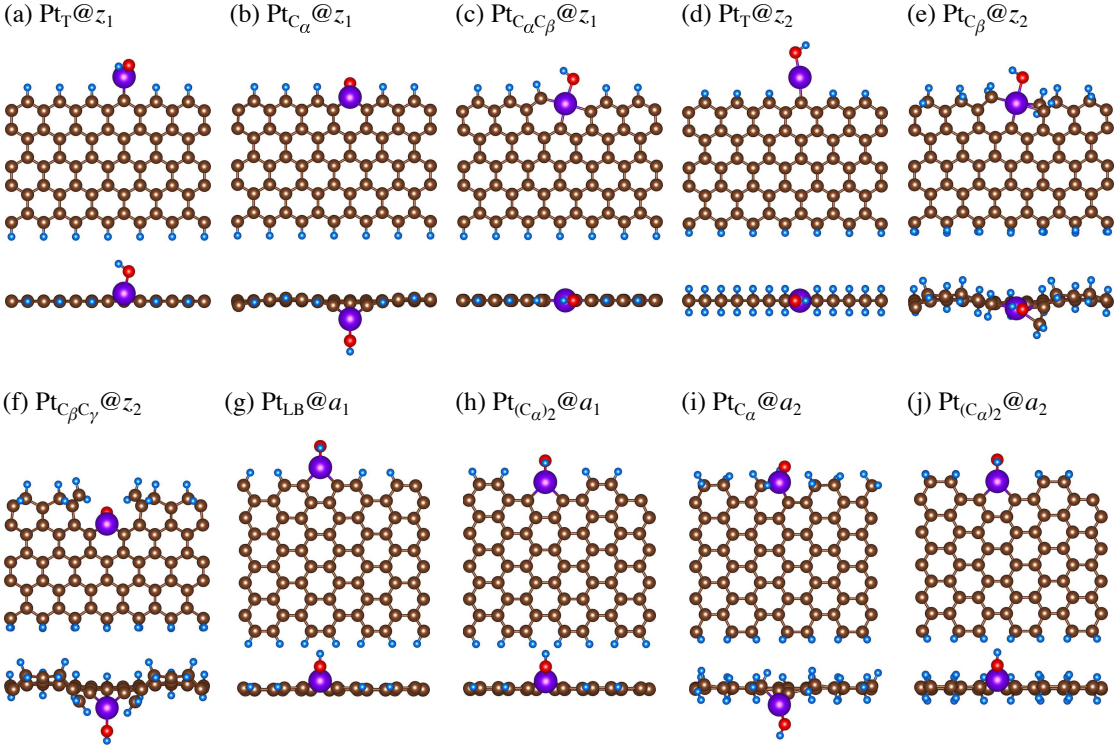

FIGURE 5.8: Optimized structures of OH adsorption on Pt@GNRs. Purple, brown, light blue, and red spheres represent of Pt, C, H and O atoms, respectively.

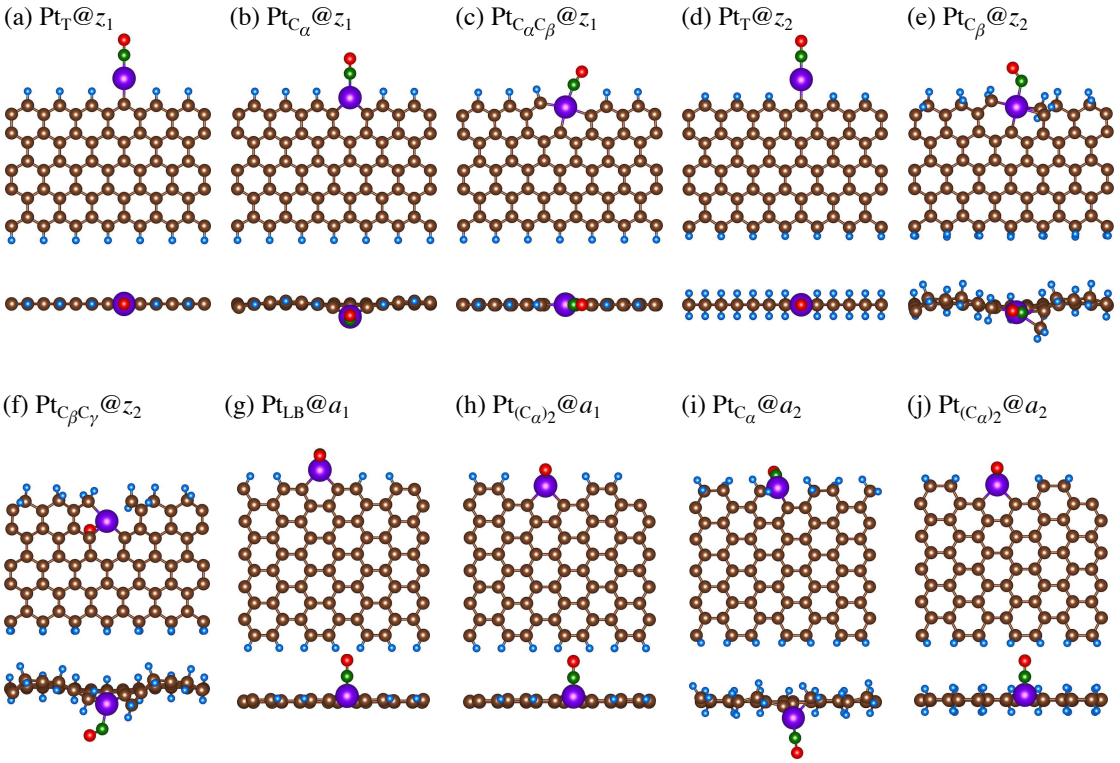

FIGURE 5.9: Optimized structures of NO adsorption on Pt@GNRs. Purple, brown, light blue, green and red spheres represent of Pt, C, H , N and O atoms, respectively.

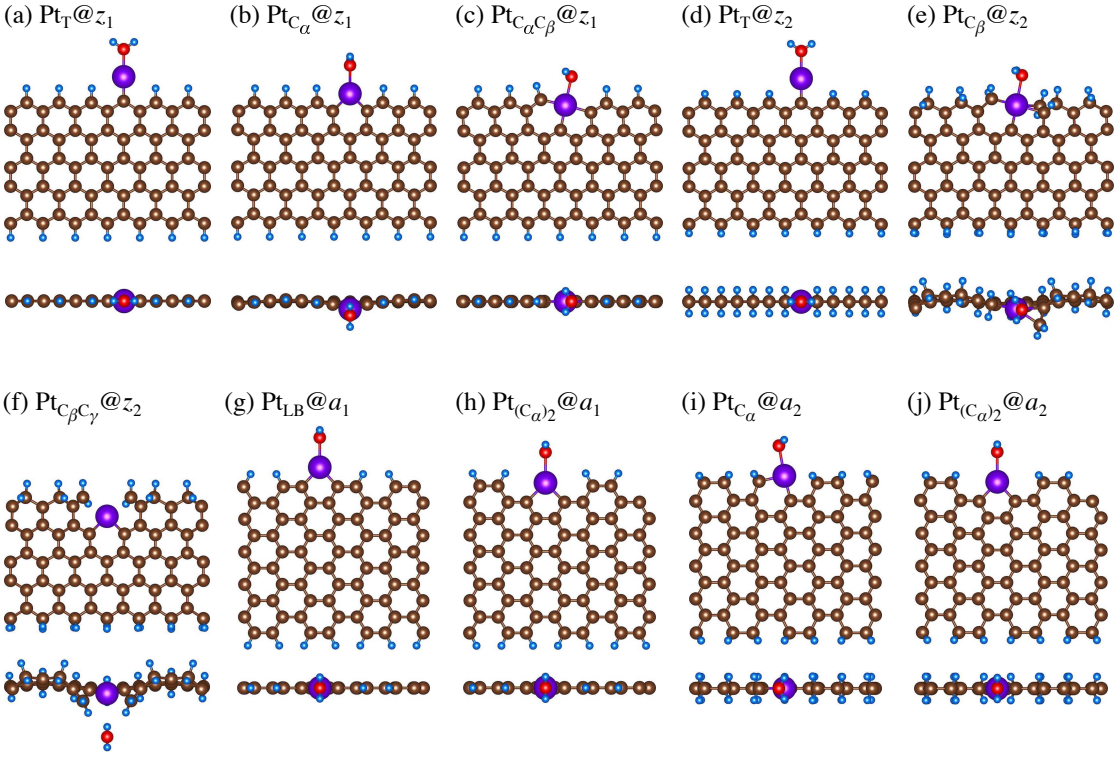

FIGURE 5.10: Optimized structures of H_2O adsorption on Pt@GNRs. Purple, brown, light blue, and red spheres represent of Pt, C, H and O atoms, respectively.

5.3.2 Electronic structure analysis

To gain insight into the adsorption mechanisms for Pt@GNR and to understand the origin of strengthening and weakening of adsorption in more detail, I perform the electronic structure analysis. Here I focus on CO and OH adsorptions as they are relevant to the CO (electro-) oxidation and ORR of our interest. I choose $Pt_T@z_1$, $Pt_{C_\alpha}@z_1$, and $Pt_{C_\alpha C_\beta}@z_1$, as representatives of one-, two-, and three-fold coordinated single Pt atoms at the edge of GNR. Corresponding CO adsorption energies are 2.32, 1.79, and 1.93 eV, respectively, whereas those for OH are 2.96, 3.28, and 2.91 eV, respectively.

Since the systems have different number of atoms, it is important to align the electronic levels among the systems, to understand the electronic origin of their relative stability. To this end, I aligned the energy levels as follows: I first choose one of carbon atoms, which is located at the pristine edge (i.e., the edge opposite to that with adsorbate), and use its $2p$ state as a reference, because it is not affected significantly by the molecular adsorption. Energy levels of the systems considered are aligned by using the $2p$ state of this carbon atom. Then, all the energy levels of the systems are referenced to the Fermi level of pristine GNR, which is located at the midpoint between the valence band maximum and conduction band minimum. Note that the pristine GNR used in this work exhibits a band gap, because of the finite width of the ribbon [39].

Figure 5.11 displays densities of states projected onto atomic orbital (PDOSs), gross populations (GPOPs), and crystal orbital overlap populations (COOPs) for

CO/Pt@GNR [40, 36]. The COOP is a density of states weighed by the overlap between a molecular orbital and substrate (graphene) states, and positive (negative) value indicates their bonding- (antibonding-) type interaction. Overall, CO adsorption is characterized by the antibonding type interaction between CO (4σ+5σ) orbital and Pt $d_{3z^2-r^2}$ (d_{z^2}) orbital, and the bonding type interaction between CO $2\pi^*$ and Pt d_{yz}/d_{zx} orbital, similar to CO adsorption on a Pt atom (see Figs. S7 and S8) and that on Pt(111) surface [36]. The former is due to the Pauli repulsion between the occupied (4σ+5σ) and d_{z^2} orbitals, and the latter, to the back donation to the unoccupied $2\pi^*$ orbitals. In addition, there is antibonding-type interaction between 5σ and extended Pt *sp* orbitals, which originate from the hybridization between Pt and graphene orbitals.

The PDOS of Pt_T is similar to that of the Pt atom. In addition, there is insignificant antibonding interaction between 5σ and Pt orbitals, resulting in relatively large adsorption energy. In the case of $Pt_{C_\alpha}@z_1$, the population of $2\pi^*$ orbitals is relatively small as can be seen in GPOP, and small Pauli repulsion is indicated by COOP, leading to the small adsorption energy. On the other hand, $Pt_{C_\alpha C_\beta}@z_1$ shows larger population of $2\pi^*$ orbitals and larger Pauli repulsion, giving larger adsorption energy as a competition of these two. It is concluded that CO adsorption at Pt@GNR is determined by the balance of the binding through $2\pi^*$ orbital and the Pauli repulsion between 5σ and *sp* orbitals, and as a result $Pt_{C_\alpha}@z_1$ gives weaker adsorption, which is one of desired properties for a better catalyst for the CO electro-oxidation (see below).

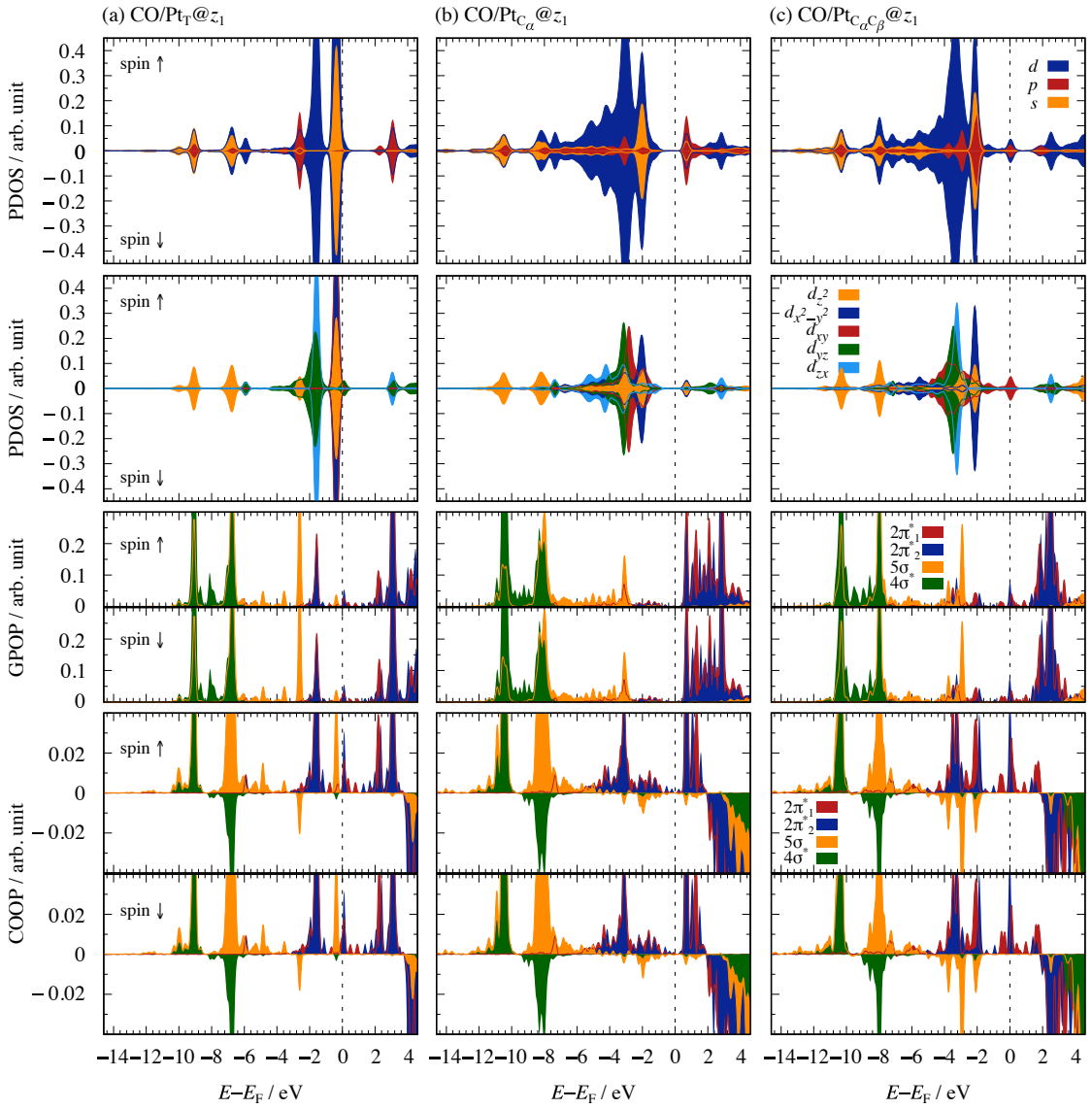

FIGURE 5.11: Density of states projected onto Pt s (orange), p (red), and d (dark-blue) states; m-resolved density of states of Pt atom; GPOPs and COOPs of CO adsorption on (a) Pt$_T$@z_1, (b) Pt$_{C_\alpha}$@z_1, and (c) Pt$_{C_\alpha C_\beta}$@z_1. Energy zero is set to the Fermi level (E_F).

Figure 5.12 shows PDOSs, GPOPs, and COOPs for OH/Pt@GNR. OH adsorption is characterized by antibonding type interaction between OH 3σ orbital and Pt d_{z^2}, and bonding/antibonding type interaction between OH $1\pi_1$ and $1\pi_2$ orbitals and Pt d_{yz} and d_{zx}. In the case of Pt$_T$@z_1 and Pt$_{C_\alpha C_\beta}$@z_1, the antibonding states derived from $1\pi_2$ are mostly unoccupied, suggesting the bonding interaction, whereas $1\pi_1$ derived antibonding-type states are partially occupied, indicating the

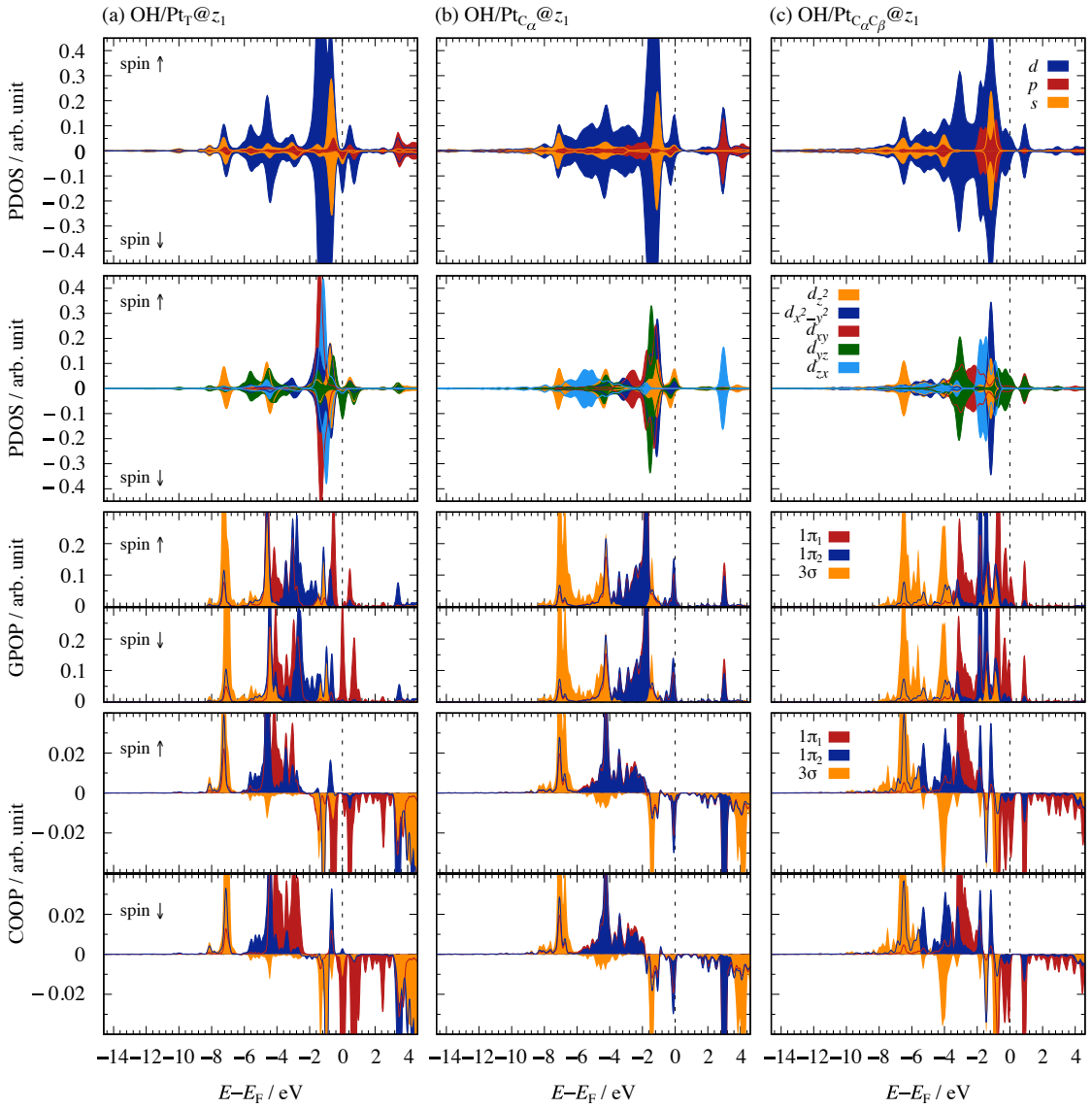

FIGURE 5.12: Density of states projected onto Pt s (orange), p (red), and d (dark-blue) states; m-resolved density of states of Pt atom; GPOPs and COOPs of OH adsorption on (a) Pt$_T$@z_1, (b) Pt$_{C_\alpha}$@z_1, and (c) Pt$_{C_\alpha C_\beta}$@z_1. Energy zero is set to the Fermi level (E_F).

antibonding contribution to the OH adsorption. In the case of Pt$_{C_\alpha}$@z_1, however, although antibonding states derived from 1π_1 and 1π_2 orbitals are partially occupied, their populations and thus the contributions are minor, resulting in smaller Pauli repulsion and the larger adsorption energy than the other two. The degree of bonding and antibonding interactions of 1π_1 and 1π_2 orbitals with Pt d states determines the stability of OH on PtGNR. The strong OH binding is also one of

the desired properties for better CO electro-oxidation catalyst as described below.

5.3.3 Implication to electrocatalysis

Having obtained the adsorption energies of atoms and molecules on Pt@GNR, I examine the catalytic activity of Pt@GNR for selected chemical reactions, namely, CO electro-oxidation and ORR, based on the kinetic models proposed in Refs. 2 and 3 respectively, and discuss the implication to the electrocatalytic reactions.

5.3.3.1 CO Electro-oxidation

Following Ref. 2, I consider the reactions of CO and H_2O through the following processes:

$$\mathrm{CO} + * \overset{K_{\mathrm{CO}}}{\longleftrightarrow} {}^*\mathrm{CO} \tag{5.3}$$

$$\mathrm{H_2O} + * \overset{K_{\mathrm{w}}}{\longleftrightarrow} \mathrm{H_2O}^* \tag{5.4}$$

$$\mathrm{H_2O}^* \overset{k_{\mathrm{OH}}}{\longrightarrow} {}^*\mathrm{OH} + \mathrm{H}^+ + e^- \tag{5.5}$$

$${}^*\mathrm{CO} + {}^*\mathrm{OH} \overset{k_{\mathrm{OX}}}{\longrightarrow} 2* + \mathrm{CO_2} + \mathrm{H}^+ + e^- \tag{5.6}$$

where $*$ indicates a free Pt site on Pt@GNRs. K_{CO} and K_{w} are the equilibrium constants for CO adsorption (5.3) and H_2O adsorption (5.4), respectively. CO and H_2O compete with each other to be deposited on a free Pt site, as represented in the reactions (5.3) and (5.4). The reaction (5.5) is a dissociation process of adsorbed H_2O, and the reaction (5.6) is that of adsorbed OH and adsorbed CO to form CO_2. The reactions (5.5) and (5.6) are characterized by the forward rate

constants k_{OH} and k_{OX}, respectively. For both cases, the reverse reactions are supposed to be slow enough and can be neglected.

The site balance in terms of the coverages of CO, H_2O and Pt free site can be written as

$$\theta_{\mathrm{CO}} + \theta_w + * = 1. \tag{5.7}$$

For the minority species (OH^*), the pseudo-steady state approximation is applied:

$$\frac{d\theta_{\mathrm{OH}}}{dt} = k_{\mathrm{OH}}\theta_w - k_{\mathrm{OX}}\theta_{\mathrm{CO}}\theta_{OH} = 0 \tag{5.8}$$

The reactions (5.5) and (5.6) involve charge transfer, and the current density associated with the CO oxidation can be expressed as:

$$\frac{j}{eM} = k_{\mathrm{OH}}\theta_w + k_{\mathrm{OX}}\theta_{\mathrm{CO}}\theta_{OH} = 2k_{\mathrm{OH}}\theta_w, \tag{5.9}$$

where e is the elementary charge and M is the surface atom density. In this kinetic model, the current density for the system i can be written as

$$\begin{aligned} j_i(U) &= j_{\mathrm{Pt}}(U)\exp(-(\delta E^i + \delta\mu U/d)/k_{\mathrm{B}}T) \\ &= j_{\mathrm{Pt}}(0)\exp(-(\delta E^i + \delta\mu U/d - e\alpha U)/k_{\mathrm{B}}T) \end{aligned} \tag{5.10}$$

with

$$\delta E^i \simeq (E^i_{\mathrm{CO}} - E^{\mathrm{Pt}}_{\mathrm{CO}}) - (E^i_{\mathrm{OH}} - E^{\mathrm{Pt}}_{\mathrm{OH}}) \tag{5.11}$$

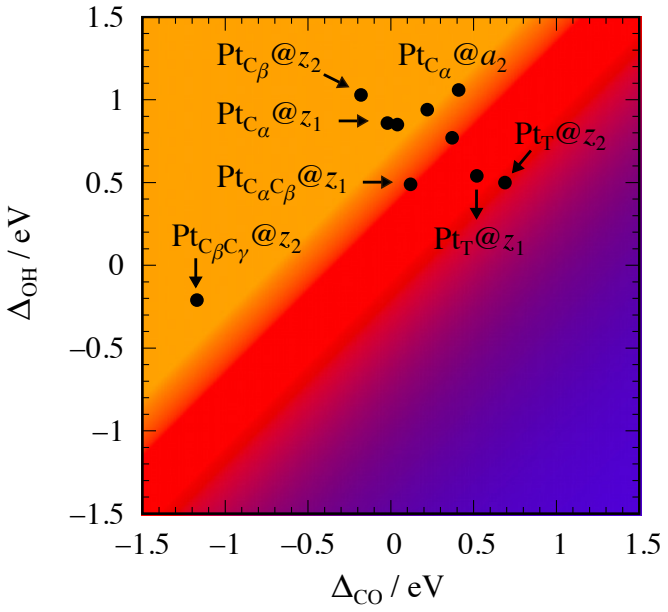

FIGURE 5.13: Comparison between Δ_{CO} and Δ_{OH} for all the Pt@GNRs considered in this work. The contour corresponds to the current density of a catalyst. The orange, red, and dark-blue areas respectively indicate a better, an equal, and a less catalytic activity of a catalyst with respect to Pt(111).

and

$$\delta\mu^i \simeq (\mu^i_{CO} - \mu^{Pt}_{CO}) - (\mu^i_{OH} - \mu^{Pt}_{OH}), \tag{5.12}$$

where j_{Pt} is the current density for CO oxidation on Pt(111); U is the electrode potential, d is the effective distance from the surface, in which the potential drop takes place, and thus, U/d is the field strength; α is transfer coefficient; E^i_{OH} and E^i_{CO} are the adsorption energies of OH and CO on the system i, respectively; μ is the dipole moment of the adsorbate in the gas phase. Here I assume that the dipole moment difference $\delta\mu$ is small and is negligible, and only the adsorption energies are required to estimate the current density.

According to Eq. (5.10), a better catalyst with respect to Pt(111) should has negative δE^i. Ideally, it can be realized if OH adsorption on the system i is stronger than on pure Pt(111) ($\Delta_{OH} = E^i_{OH} - E^{Pt}_{OH} > 0$) and CO adsorption

TABLE 5.6: Adsorption energy of CO (E_{CO}) on Pt@GNRs and adsorption energy difference from Pt(111) (Δ_{CO}) with ZPE correction. Those without ZPE correction are given in the parentheses. The unit of energy is eV.

	E_{CO}	Δ_{CO}
$Pt_T@z_1$	2.28 (2.32)	0.52 (0.52)
$Pt_{C_\alpha}@z_1$	1.74 (1.79)	−0.02 (−0.01)
$Pt_{C_\alpha C_\beta}@z_1$	1.87 (1.93)	0.11 (0.13)
$Pt_T@z_2$	2.46 (2.50)	0.70 (0.70)
$Pt_{C_\beta}@z_2$	1.58 (1.63)	−0.18 (−0.17)
$Pt_{C_\beta C_\gamma}@z_2$	0.59 (0.64)	−1.17 (−1.16)
$Pt_{LB}@a_1$	2.12 (2.18)	0.36 (0.38)
$Pt_{(C_\alpha)_2}@a_1$	1.98 (2.03)	0.22 (0.23)
$Pt_{C_\alpha}@a_2$	2.16 (2.21)	0.40 (0.41)
$Pt_{(C_\alpha)_2}@a_2$	1.79 (1.84)	0.03 (0.04)
Pt(111)	1.76 (1.80)	-

is weaker ($\Delta_{CO} = E^i_{CO} - E^{Pt}_{CO} < 0$), or $\Delta_{OH} > \Delta_{CO}$. In Fig. 5.13 I plot Δ_{OH} and Δ_{CO} for all Pt@GNRs considered. Ideally, a better catalyst with respect to Pt(111) tends to go to the orange area. Otherwise, it will be appear in the blue area. It is found that only $Pt_T@z_2$ appears close to the blue area, indicating that the Pt@GNRs have better catalytic activity than a pure Pt(111). I confirm that the results are unchanged and the trend in the adsorption energies are the same, when ZPE correction is included (Tables 5.6 and 5.7). I also confirm that this conclusion is unchanged when the Pt@GNR is supported by graphene (see Table 5.8 and Fig. 5.14).

5.3.3.2 Oxygen Reduction Reaction

I then consider ORR on Pt@GNRs and Pt(111) as electrocatalysts for fuel cell cathodes. I adopt a kinetic model for the cathodic processes proposed by Nørskov

TABLE 5.7: Adsorption energy of OH (E_{OH}) on Pt@GNRs and adsorption energy difference from Pt(111) (Δ_{OH}) with ZPE correction. Those without ZPE correction are given in the parentheses. The unit of energy is eV.

	E_{OH}	Δ_{OH}
$\mathrm{Pt_T}@z_1$	2.86 (2.96)	0.58 (0.54)
$\mathrm{Pt_{C_\alpha}}@z_1$	3.08 (3.28)	0.80 (0.86)
$\mathrm{Pt_{C_\alpha C_\beta}}@z_1$	2.80 (2.91)	0.52 (0.49)
$\mathrm{Pt_T}@z_2$	2.80 (2.92)	0.52 (0.50)
$\mathrm{Pt_{C_\beta}}@z_2$	3.33 (3.45)	1.05 (1.03)
$\mathrm{Pt_{C_\beta C_\gamma}}@z_2$	2.10 (2.21)	−0.18 (−0.21)
$\mathrm{Pt_{LB}}@a_1$	3.09 (3.19)	0.81 (0.77)
$\mathrm{Pt_{(C_\alpha)_2}}@a_1$	3.26 (3.36)	0.98 (0.94)
$\mathrm{Pt_{C_\alpha}}@a_2$	3.37 (3.48)	1.09 (1.06)
$\mathrm{Pt_{(C_\alpha)_2}}@a_2$	3.16 (3.27)	0.88 (0.85)
Pt(111)	2.28 (2.42)	-

et al. [3]. A dissociative mechanism for ORR at a cathode can be described as

$$\frac{1}{2}\mathrm{O_2} + * \longrightarrow \mathrm{O}^* \tag{5.13}$$

$$\mathrm{O}^* + \mathrm{H}^+ + e^- \longrightarrow \mathrm{HO}^* \tag{5.14}$$

$$\mathrm{HO}^* + \mathrm{H}^+ + e^- \longrightarrow \mathrm{H_2O} + * \tag{5.15}$$

Here, $*$ denotes a free site at the PtGNRs or Pt(111). The adsorption energies of reaction intermediates O^* and OH^* are defined as the reaction energies of the

TABLE 5.8: Adsorption energy of CO (E_{CO}) on Pt@GNRs with graphene substrate and adsorption energy difference from Pt(111). The unit of energy is eV.

	E_{CO}	Δ_{CO}
$\mathrm{Pt_T}@z_1$	2.48	0.68
$\mathrm{Pt_{C_\alpha}}@z_1$	1.61	−0.19
$\mathrm{Pt_{C_\alpha C_\beta}}@z_1$	2.04	0.24
Pt(111)	1.80	-

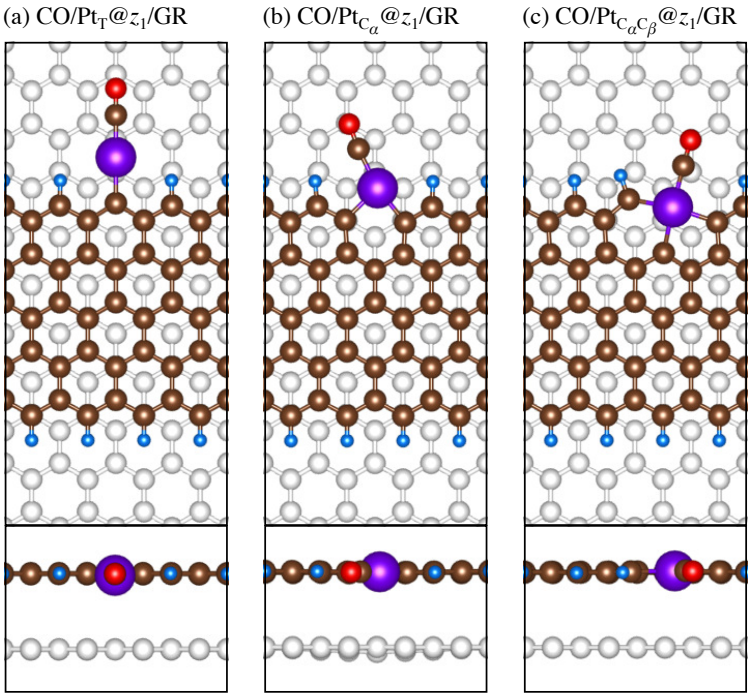

FIGURE 5.14: Optimized structures of CO adsorbed on Pt@GNRs with graphene substrate. Purple, brown, grey, red, and light blue spheres represent Pt, C of GNR, C of graphene substrate, O, and H atoms, respectively.

following reactions

$$H_2O + * \longrightarrow HO^* + \frac{1}{2}H_2 \tag{5.16}$$

$$H_2O + * \longrightarrow O^* + H_2 \tag{5.17}$$

where H_2O and H_2 are the gas phase molecule. By calculating the adsorption energies of the reaction intermediates, we can evaluate the activation free energies for these processes as follows:

$$\Delta G_1(U) = \Delta G_1(U_0) - e\eta \tag{5.18}$$

$$\Delta G_2(U) = \Delta G_2(U_0) - e\eta \tag{5.19}$$

TABLE 5.9: Adsorption energy of O (E_{O}) on Pt@GNRs and adsorption energy difference from Pt(111) (Δ_{O}) with ZPE correction. Those without ZPE correction are given in parentheses. The unit of energy is eV.

	E_{O}	Δ_{O}
$\mathrm{Pt_T}@z_1$	1.12 (1.24)	−0.89 (−0.85)
$\mathrm{Pt_{C_\alpha}}@z_1$	1.20 (1.33)	−0.81 (−0.76)
$\mathrm{Pt_{C_\alpha C_\beta}}@z_1$	0.87 (0.99)	−1.14 (−1.10)
$\mathrm{Pt_T}@z_2$	1.73 (1.86)	−0.28 (−0.23)
$\mathrm{Pt_{C_\beta}}@z_2$	1.02 (1.13)	−0.99 (−0.96)
$\mathrm{Pt_{C_\beta C_\gamma}}@z_2$	1.50 (1.70)	−0.51 (−0.39)
$\mathrm{Pt_{LB}}@a_1$	1.30 (1.43)	−0.71 (−0.66)
$\mathrm{Pt_{(C_\alpha)_2}}@a_1$	1.41 (1.53)	−0.60 (−0.56)
$\mathrm{Pt_{C_\alpha}}@a_2$	1.38 (1.51)	−0.63 (−0.58)
$\mathrm{Pt_{(C_\alpha)_2}}@a_2$	1.31 (1.44)	−0.70 (−0.65)
Pt(111)	2.01 (2.09)	-

where, ΔG_1 and ΔG_2 are the free-energy differences for reactions (5.14) and (5.15), respectively, and $\eta = U - U_0$ is the overpotential. Based on the calculated free energies, we are able to calculate the rate constant of the reaction k in the unit of current density as a function of potential

$$j_{\mathrm{k}}(U) = \tilde{j}_{\mathrm{k}} \exp(-\Delta G_k(U)/k_{\mathrm{B}}T), \tag{5.20}$$

where $\tilde{j}_{\mathrm{k}}$ is the maximum current per surface area. I calculate the rate constant as a function of potential and found that the results are very dependent on the exchange-correlation functionals used. Thus, to investigate the catalytic activity of the PtGNRs, we chose to discuss the difference from Pt(111), not the absolute current density or rate constant for ORR activity.

To this end, I compare the O adsorption energy of Pt@GNR to Pt(111), which is suggested as a good descriptor for ORR. In Table 5.9, O adsorption energy and adsorption energy differences between Pt@GNR and Pt(111) are summarized. As

suggested by Nørskov *et al.*, the metals with adsorption energy lower than that for Pt(111) by ∼0.4 eV should give a higher rate constant for ORR [3]. Although all of the Pt@GNRs considered in this work have lower adsorption energy than Pt(111), only O/Pt_T@z_2 and O/$Pt_{C_\beta C_\gamma}$@z_2 fulfill the criterion proposed in the literature [3]. Pt_T@z_2 and $Pt_{C_\beta C_\gamma}$@z_2 are not the most thermodynamically stable structures. However, they appear as metastable ones depending on the chemical potential (environment) [1],and in the working condition, they could be locally formed in the heterogeneous catalyst. Thus, it is suggested that some of Pt@GNRs considered in the present work are likely candidates for improved ORR catalysts.

5.4 Conclusion

I present a DFT study of atomic and molecular adsorption on a set of Pt@GNRs as a first step to understand their catalytic activity. I provide adsorption geometries, energeitcs, as well as the electronic structure analyses to understand the adsorption mechanism. I further use DFT energetics and simple kinetic models to predict the electrocatalytic activities of Pt@GNRs. I found that at the thermodynamically stable Pt@GNR, in which the Pt atom adsorbs at the edge of GNR, CO electro-oxidation is improved with respect to Pt(111). This is because the CO adsorption is weakened on Pt@GNRs and at the same time OH adsorption is strengthened, which are prerequisites for an enhanced CO electro-oxidation catalyst. Thus, I suggest that thermodynamically stable Pt@GNRs can be better catalysts for the CO electro-oxidation. On the other hand, the enhanced OH adsorption leads to the reduction of ORR activity. However, some metastable Pt@GNRs were found

to be efficient catalysts for ORR. In the heterogeneous catalyst, there are many metastable configurations depending on the environment, and therefore we anticipate that Pt@NGR with metastable structures can be better catalyst for ORR. To assess their catalytic performances more quantitatively, it is desirable to study the kinetics of the reactions of interest, which is underway. Furthermore, effect of the solvent, and electrode potential should be included to assess their performances as electrocatalysts. This may be enabled by the use of the recently developed effective screening medium method [41, 42] with the reference interaction site model [43, 44]. I envisage further study on Pt@GNR will provide deeper insights into the Pt single atom catalyst, which enables one to develop a better Pt single atom catalyst with desired catalytic activities.

References

[1] S. A. Wella, Y. Hamamoto, Suprijadi, Y. Morikawa, and I. Hamada, "Platinum single-atom adsorption on graphene: a density functional theory study," *Nanoscale Adv.*, vol. 1, pp. 1165–1174, 2019.

[2] P. Liu, A. Logadottir, and J. K. Nørskov, "Modeling the electro-oxidation of CO and H_2/CO on Pt, Ru, PtRu and Pt_3Sn," *Electrochim. Acta*, vol. 48, no. 25-26, pp. 3731–3742, 2003.

[3] J. K. Nørskov, J. Rossmeisl, A. Logadottir, L. Lindqvist, J. R. Kitchin, T. Bligaard, and H. Jónsson, "Origin of the overpotential for oxygen reduction at a fuel-cell cathode," *J. Phys. Chem. B*, vol. 108, no. 46, pp. 17886–17892, 2004.

[4] Y. Morikawa, K. Iwata, and K. Terakura, "Theoretical study of hydrogenation process of formate on clean and Zn deposited Cu(111) surfaces," *Appl. Surf. Sci.*, vol. 169–170, pp. 11–15, 2001.

[5] Y. Morikawa, H. Ishii, and K. Seki, "Theoretical study of n-alkane adsorption on metal surfaces," *Phys. Rev. B*, vol. 69, p. 041403, 2004.

[6] D. Vanderbilt, "Soft self-consistent pseudopotentials in a generalized eigenvalue formalism," *Phys. Rev. B*, vol. 41, pp. 7892–7895, 1990.

[7] I. Hamada, "Van der Waals density functional made accurate," *Phys. Rev. B*, vol. 89, p. 121103, Mar 2014.

[8] Y. Hamamoto, I. Hamada, K. Inagaki, and Y. Morikawa, "Self-consistent van der Waals density functional study of benzene adsorption on Si(100)," *Phys. Rev. B*, vol. 93, p. 245440, Jun 2016.

[9] G. Román-Pérez and J. M. Soler, "Efficient implementation of a van der Waals density functional: Application to double-wall carbon nanotubes," *Phys. Rev. Lett.*, vol. 103, p. 096102, Aug 2009.

[10] J. Wu and F. Gygi, "A simplified implementation of van der Waals density functionals for first-principles molecular dynamics applications," *J. Chem. Phys.*, vol. 136, no. 22, p. 224107, 2012.

[11] J. P. Perdew, K. Burke, and M. Ernzerhof, "Generalized gradient approximation made simple," *Phys. Rev. Lett.*, vol. 77, pp. 3865–3868, Oct 1996.

[12] I. Hamada and Y. Morikawa, "Density-functional analysis of hydrogen on Pt(111): Electric field, solvent, and coverage effects," *J. Phys. Chem. C*, vol. 112, no. 29, pp. 10889–10898, 2008.

[13] J. Fearon and G. W. Watson, "Hydrogen adsorption and diffusion on Pt(111) and PtSn(111)," *J. Mater. Chem.*, vol. 16, pp. 1989–1996, 2006.

[14] S. Gautier, S. N. Steinmann, C. Michel, P. Fleurat-Lessard, and P. Sautet, "Molecular adsorption at pt(111). how accurate are dft functionals?," *Phys. Chem. Chem. Phys.*, vol. 17, pp. 28921–28930, 2015.

[15] J. Greeley and M. Mavrikakis, "A first-principles study of methanol decomposition on Pt(111)," *J. Am. Chem. Soc.*, vol. 124, no. 24, pp. 7193–7201, 2002.

[16] A. A. Phatak, W. N. Delgass, F. H. Ribeiro, and W. F. Schneider, "Density functional theory comparison of water dissociation steps on Cu, Au, Ni, Pd, and Pt," *J. Phys. Chem. C*, vol. 113, no. 17, pp. 7269–7276, 2009.

[17] D. C. Ford, Y. Xu, and M. Mavrikakis, "Atomic and molecular adsorption on Pt(111)," *Surf. Sci.*, vol. 587, no. 3, pp. 159–174, 2005.

[18] L. Yan, Y. Sun, Y. Yamamoto, S. Kasamatsu, I. Hamada, and O. Sugino, "Hydrogen adsorption on Pt(111) revisited from random phase approximation," *J. Chem. Phys.*, vol. 149, pp. 164702–8, Oct. 2018.

[19] P. J. Feibelman, B. Hammer, J. K. Nørskov, F. Wagner, M. Scheffler, R. Stumpf, R. Watwe, and J. Dumesic, "The CO/Pt(111) Puzzle †," *J. Phys. Chem. B*, vol. 105, pp. 4018–4025, May 2001.

[20] J. Wellendorff, K. T. Lundgaard, K. W. Jacobsen, and T. Bligaard, "mbeef: An accurate semi-local bayesian error estimation density functional," *J. Chem. Phys.*, vol. 140, no. 14, p. 144107, 2014.

[21] P. Lazić, M. Alaei, N. Atodiresei, V. Caciuc, R. Brako, and S. Blügel, "Density functional theory with nonlocal correlation: A key to the solution of the co adsorption puzzle," *Phys. Rev. B*, vol. 81, p. 045401, Jan 2010.

[22] G. T. K. K. Gunasooriya and M. Saeys, "Co adsorption site preference on platinum: Charge is the essence," *ACS Catal.*, vol. 8, no. 5, pp. 3770–3774, 2018.

[23] G. T. K. K. Gunasooriya and M. Saeys, "Co adsorption on pt(111): From isolated molecules to ordered high-coverage structures," *ACS Catal.*, vol. 8, no. 11, pp. 10225–10233, 2018.

[24] L. K. G, I. Kundappaden, and R. Chatanathodi, "A dft study of co adsorption on pt (111) using van der waals functionals," *Surf. Sci.*, vol. 681, pp. 143–148, 2019.

[25] I. Hamada, K. Lee, and Y. Morikawa, "Interaction of water with a metal surface: Importance of van der Waals forces," *Phys. Rev. B*, vol. 81, p. 115452, Mar 2010.

[26] I. Hamada and S. Meng, "Water wetting on representative metal surfaces: Improved description from van der waals density functionals," *Chem. Phys. Lett.*, vol. 521, pp. 161 – 166, 2012.

[27] J. Carrasco, J. Klimeš, and A. Michaelides, "The role of van der waals forces in water adsorption on metals," *J. Chem. Phys.*, vol. 138, no. 2, p. 024708, 2013.

[28] K. Li, Y. Li, Y. Wang, F. He, M. Jiao, H. Tang, and Z. Wu, "The oxygen reduction reaction on pt(111) and pt(100) surfaces substituted by subsurface cu: a theoretical perspective," *J. Mater. Chem. A*, vol. 3, pp. 11444–11452, 2015.

[29] J. Greeley and M. Mavrikakis, "Competitive paths for methanol decomposition on Pt(111)," *J. Am. Chem. Soc.*, vol. 126, no. 12, pp. 3910–3919, 2004.

[30] Z. Gu and P. B. Balbuena, "Absorption of atomic oxygen into subsurfaces of Pt(100) and Pt(111): A density functional theory study," *J. Phys. Chem. C*, vol. 111, no. 27, pp. 9877–9883, 2007.

[31] A. Michaelides and P. Hu, "A density functional theory study of hydroxyl and the intermediate in the water formation reaction on Pt," *J. Chem. Phys.*, vol. 114, no. 1, pp. 513–519, 2001.

[32] P. Janthon, F. Viñes, J. Sirijaraensre, J. Limtrakul, and F. Illas, "Carbon dissolution and segregation in platinum," *Catal. Sci. Technol.*, vol. 7, pp. 807–816, 2017.

[33] S. Kandoi, A. A. Gokhale, L. C. Grabow, J. A. Dumesic, and M. Mavrikakis, "Why Au and Cu are more selective than Pt for preferential oxidation of CO at low temperature," *Catal. Lett.*, vol. 93, 2004.

[34] P. Janthon, F. Viñes, J. Sirijaraensre, J. Limtrakul, and F. Illas, "Adding pieces to the CO/Pt(111) puzzle: The role of dispersion," *J. Phys. Chem. C*, vol. 121, no. 7, pp. 3970–3977, 2017.

[35] M. D. Arce, P. Quaino, and E. Santos, "Electronic changes at the Pt(111) interface induced by the adsorption of OH species," *Catal. Today*, vol. 202, pp. 120–127, 2013. Electrocatalysis.

[36] H. Aizawa, Y. Morikawa, S. Tsuneyuki, K. Fukutani, and T. Ohno, "A density-functional study of the atomic structures and vibrational spectra of NO/Pt(111)," *Surf. Sci.*, vol. 514, no. 1, pp. 394–403, 2002.

[37] R. B. Getman and W. F. Schneider, "DFT-based characterization of the multiple adsorption modes of nitrogen oxides on Pt(111)," *J. Phys. Chem. C*, vol. 111, no. 1, pp. 389–397, 2007.

[38] B. Hammer, Y. Morikawa, and J. K. Nørskov, "Co chemisorption at metal surfaces and overlayers," *Phys. Rev. Lett.*, vol. 76, pp. 2141–2144, Mar 1996.

[39] Y.-W. Son, M. L. Cohen, and S. G. Louie, "Energy Gaps in Graphene Nanoribbons," *Phys. Rev. Lett.*, vol. 97, p. 216803, Nov. 2006.

[40] R. Hoffmann, "A chemical and theoretical way to look at bonding on surfaces," *Rev. Mod. Phys.*, vol. 60, pp. 601–628, July 1988.

[41] M. Otani and O. Sugino, "First-principles calculations of charged surfaces and interfaces: A plane-wave nonrepeated slab approach," *Phys. Rev. B*, vol. 73, p. 115407, Mar 2006.

[42] I. Hamada, M. Otani, O. Sugino, and Y. Morikawa, "Green's function method for elimination of the spurious multipole interaction in the surface/interface slab model," *Phys. Rev. B*, vol. 80, p. 165411, Oct 2009.

[43] S. Nishihara and M. Otani, "Hybrid solvation models for bulk, interface, and membrane: Reference interaction site methods coupled with density functional theory," *Phys. Rev. B*, vol. 96, p. 115429, Sep 2017.

[44] J. Haruyama, T. Ikeshoji, and M. Otani, "Electrode potential from density functional theory calculations combined with implicit solvation theory," *Phys. Rev. Mater.*, vol. 2, p. 095801, Sep 2018.

Chapter 6

Summary and Future Plan

6.1 Summary

In this dissertation, investigation of functionalizing graphene as a substrate for organic-solid surface interface and also as a support material towards single Pt atom catalyst are shown from theoretical point of views.

Chapter 4 describes the investigation of the naphthalene adsorption on graphene using the vdW-DF method. It is found that the intermolecular interaction drives the molecules to form a well-ordered superstructure with a tilted adsorption geometry. Not only to stabilize the geometry, the intermolecular interaction also induces IPS-like states on naphthalene overlayer, adding the new insight that IPS is not only appears in metal surfaces or in graphitic materials but also in molecule monolayer. Further, these states hybridize with the graphene IPSs to form hybrid IPSs. Another important information that can be extracted from the results is the impact of the naphthalene adsorption appears most prominently in the anisotropic effective mass of the resultant hybrid IPSs, which strongly reflects the molecular

structure of naphthalene. It is expected that similar hybrid IPSs widely exist at interfaces of molecular overlayers and solid surfaces.

Chapter 5 presents a systematic study of Pt single-atom adsorption on graphene. It is found that the single Pt atoms adsorb more preferably at the graphene edge than on the bulk. More specific they preferably adsorb at the edge of hydrogenated zGNR despite the fact that the pristine aGNR is thermodynamically more stable than zGNR under a wide range of hydrogen pressure. From calculated core level shifts and density of states for the stable structures, it is suggested that single Pt atoms and graphene have a strong interaction.

Chapter 6 reports the adsorption of some atoms and molecules on several favorable structures presented in **Chapter 5**. Combine with kinetic models, it is predicted that in comparison with the Pt(111) surface, single Pt atoms supported by graphene nanoribbon show a better activity in CO electro-oxidation. It is presumably the origin for the improved CO tolerance in the anode electrode in direct methanol fuel cell. Some metastable Pt@GNRs are found to be efficient catalysts for ORR. In the heterogeneous catalyst, there are many metastable configurations depending on the environment, and therefore it is anticipated that Pt@GNR with metastable structures could be better catalyst for ORR.

The results which is presented in **Chapters 5 and 6** lead to a basis insight for further investigation of single-atom catalysts based on platinum and graphene related materials.

6.2 Future Plan

Obviously, the present study is not the end of all. The research presented in this dissertation seems need to be improved by some future works. In particular, study about catalytic activity of single Pt atom catalyst supported by graphene nanoribbon is just a qualitative results. As a next challenge, reaction process of a specific oxidation reduction reaction on single Pt atom catalyst supported by graphene nanoribbons is essentially important to be studied. In this issue, I am going to perform the nudge elastic band method to produce the reaction path of a specific reaction. Further, it is able to give a better insight of the single Pt atom catalyst supported by graphene nanoribbons.

Appendix A

Band Structure and IPSs of Graphene (rev-vdW-DF2)

In Chapter 2, I have shown in Fig. 3.4 the band structures of naphthalene on graphene and the naphthalene monolayer, and pointed out the existence of parabolic dispersions at each Γ point, which are analogous to the image-potential states of graphene. In order to understand the analogy, it is instructive to review the electronic structure of graphene, although its IPSs have been studied intensively so far [1, 2]. I show the unoccupied energy bands calculated with the rev-vdW-DF2 functional [3] for the (1×1) and $(2\sqrt{3} \times 2\sqrt{3})$ unit cells in Figs. A.1(a) and (b), respectively. In addition to the well-known linear dispersions at the K point, one also finds two parabolic bands at the Γ point in Fig. A.1(a), whose bottoms appear at 2.84 and 3.68 eV from the Fermi level. These bands are in good agreement with 1^+ and 1^- IPSs of graphene obtained with the local density approximation plus image potential correction of 2.94 and 3.69 eV, respectively [1]. The remarkable agreement is due to the fact that the description of the image potential, especially

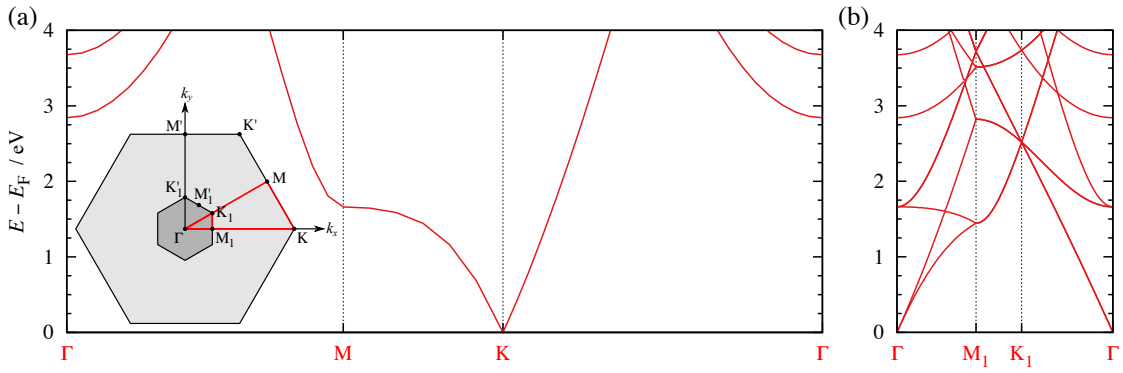

FIGURE A.1: Band structures above the Fermi level (E_F) of graphene for the (a) (1×1) and (b) $(2\sqrt{3} \times 2\sqrt{3})$ unit cells. The large and small hexagons in the inset illustrates the original and folded Brillouin zones corresponding to (a) and (b), respectively.

at short distance ≤ 3 Å, is improved by the nonlocal correlation term in the vdW-DF method [2], although accurate description of higher IPSs are still challenging for vdW-DF. For the $(2\sqrt{3} \times 2\sqrt{3})$ unit cell, the parabolic bands of these IPSs are retained at Γ, while the linear dispersions at K are folded into Γ as shown in Fig. A.1(b). Note that the parabolic bands with their bottoms at 2.84 and 3.69 eV are called the lowest IPSs (LIPSs) with even (1^+) and odd (1^-) parities, respectively, in the main text.

References

[1] V. M. Silkin, J. Zhao, F. Guinea, E. V. Chulkov, P. M. Echenique, and H. Petek, "Image potential states in graphene," *Phys. Rev. B*, vol. 80, p. 121408, Sep 2009.

[2] I. Hamada, Y. Hamamoto, and Y. Morikawa, "Image potential states from the van der Waals density functional," *J. Chem. Phys.*, vol. 147, no. 4, p. 044708, 2017.

[3] I. Hamada, "Van der Waals density functional made accurate," *Phys. Rev. B*, vol. 89, p. 121103, Mar 2014.

Appendix B

PDOS, GPOP, and COOP Analysis

In this Appendix, I provide the densities of states projected onto atomic orbital (PDOSs), gross populations (GPOPs), and crystal orbital overlap populations (COOPs) for several systems: pristine z_1, single Pt atom, selected pristine Pt@GNRs, CO/Pt_1, CO/Pt(111), CO/Pt@GNRs, OH/Pt_1, and OH//Pt@GNRs.

B.1 Pristine z_1

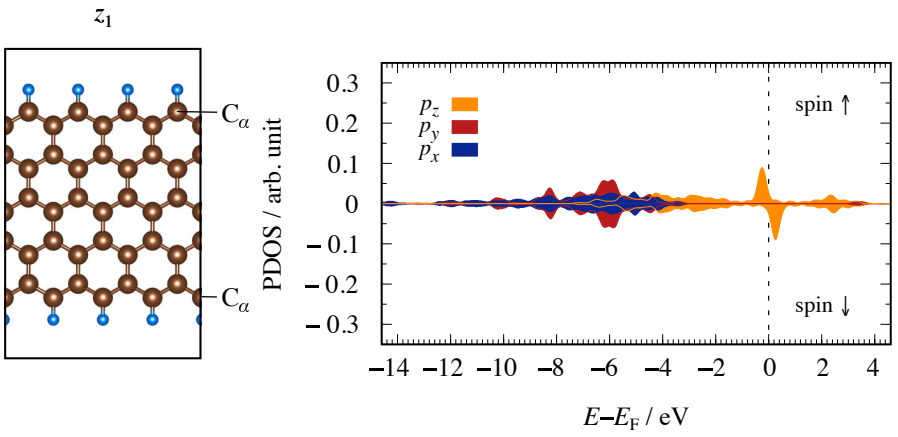

FIGURE B.1: m-resolved density of states for pristine mono-hydrogenated zigzag graphene nanoribbon. Energy zero is set to the Fermi level (E_F)

.

B.2 Single Pt Atom

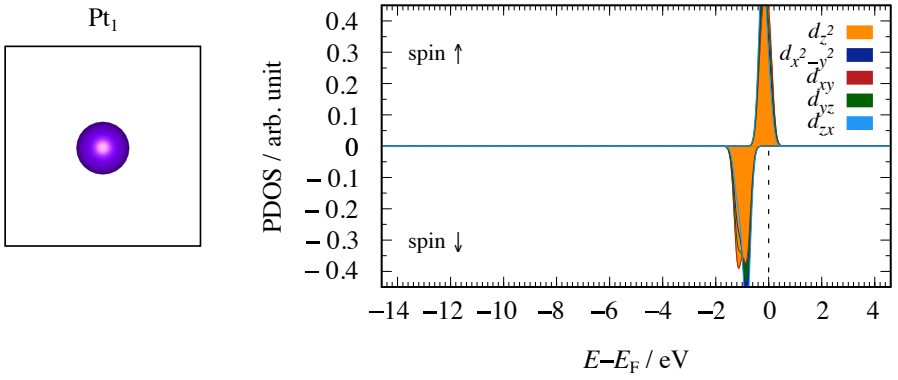

FIGURE B.2: m-resolved density of states for single Pt atom. Energy zero is set to the Fermi level (E_F)

.

B.3 Selected Pristine Pt@GNRs

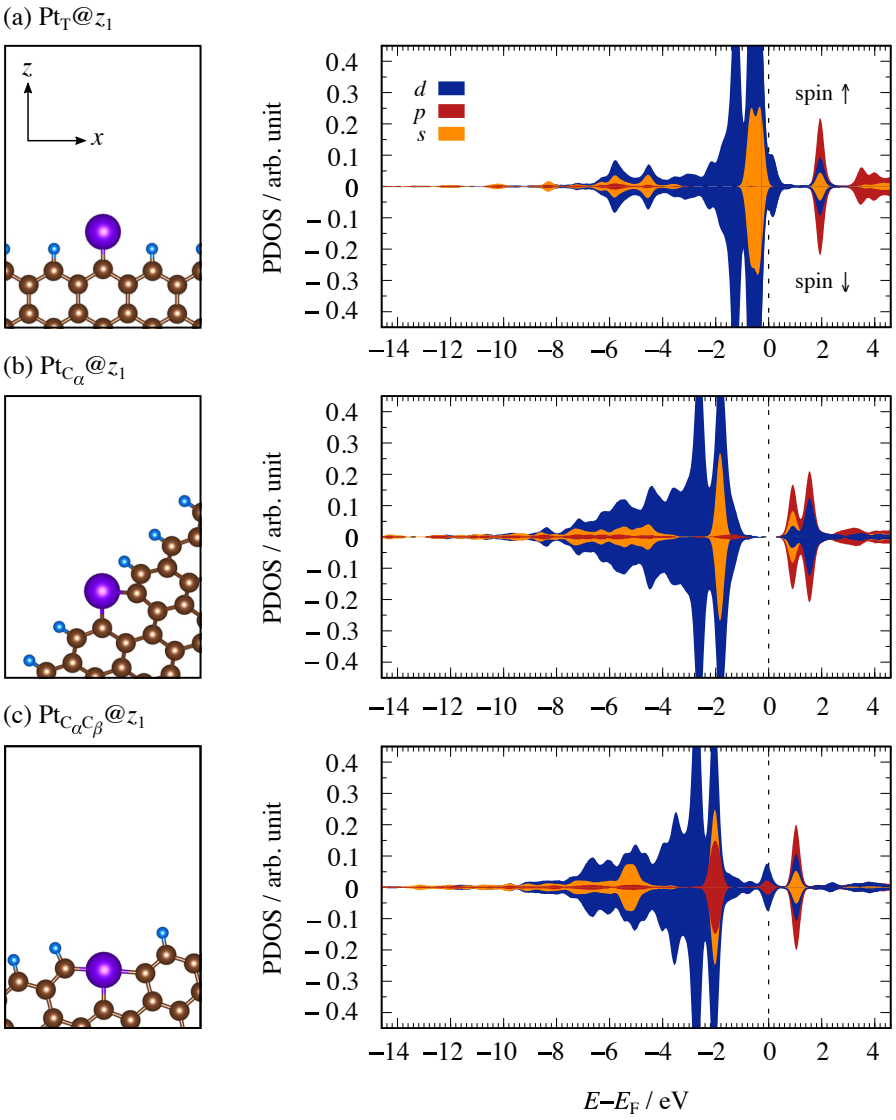

FIGURE B.3: Density of states projected onto Pt s (orange), p (red), and d (dark-blue) states of some pristine single Pt atom at the edge of graphene nanoribbons (Pt@GNRs): (a) $Pt_T@z_1$, (b) $Pt_{C_\alpha}@z_1$, and (c) $Pt_{C_\alpha C_\beta}@z_1$. Energy zero is set to the Fermi level (E_F)

.

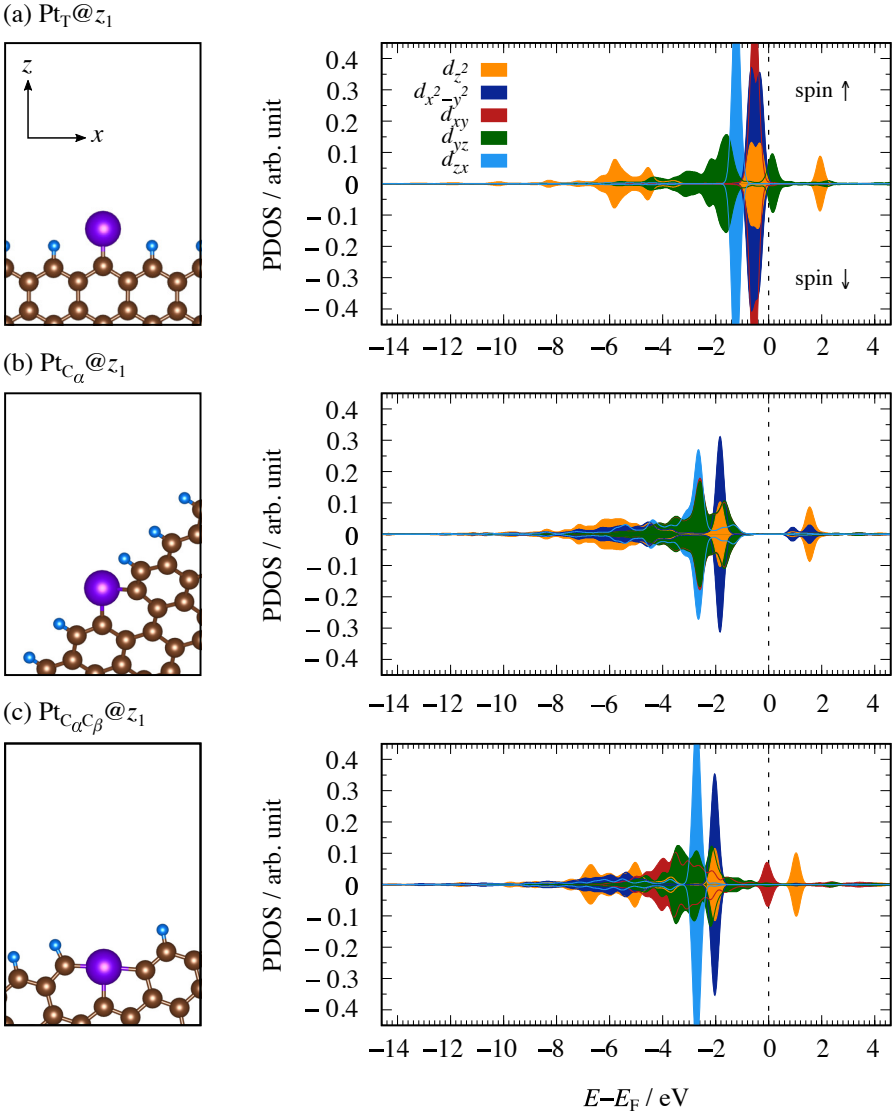

FIGURE B.4: *m*-resolved density of states for some pristine Pt@GNRs: (a) $Pt_T@z_1$, (b) $Pt_{C_\alpha}@z_1$, and (c) $Pt_{C_\alpha C_\beta}@z_1$. Energy zero is set to the Fermi level (E_F)

B.4 CO/Pt$_1$ and CO/Pt(111)

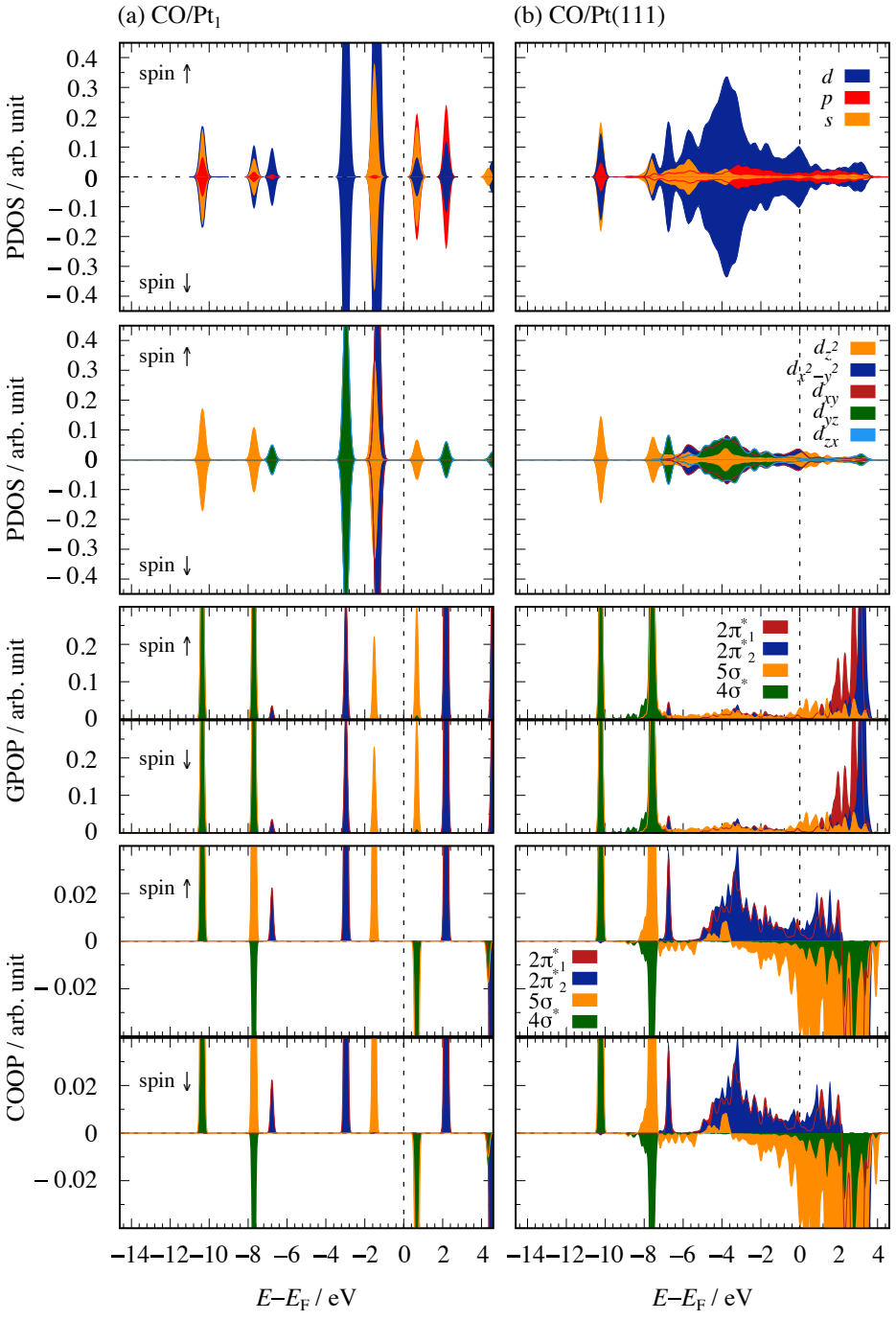

FIGURE B.5: Density of states projected onto Pt s (orange), p (red), and d (dark-blue) states; m-resolved density of states of Pt atom; gross populations (GPOPs) and crystal orbital overlap populations (COOPs) (d) of CO for (a) CO/Pt$_1$ and (b) CO/Pt(111) systems. The $2\pi_1^*$, $2\pi_2^*$, 5σ, and $4\sigma^*$ orbitals are shown in red, dark-blue, orange, and green filled lines, respectively. Energy zero is set to the Fermi level (E_F).

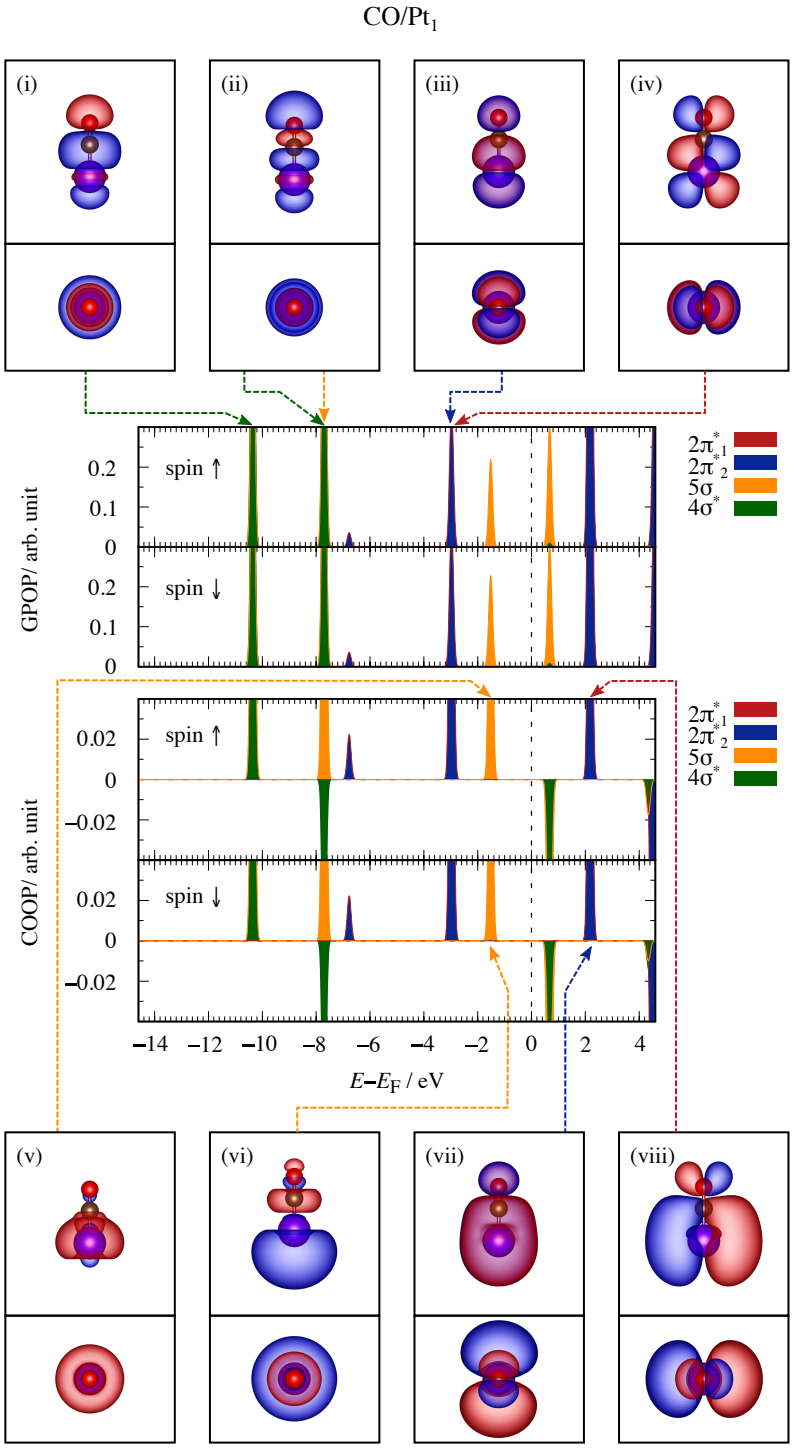

FIGURE B.6: Gross populations (GPOPs) and Crystal orbital overlap populations (COOPs) of CO for the CO/Pt_1 system. The $2\pi_1^*$, $2\pi_2^*$, 5σ, and $4\sigma^*$ orbitals are shown in red, dark-blue, orange, and green filled lines, respectively. Energy zero is set to the Fermi level (E_F). Wave functions which correspond to some peaks are shown.

B.5 CO/Pt@GNRs

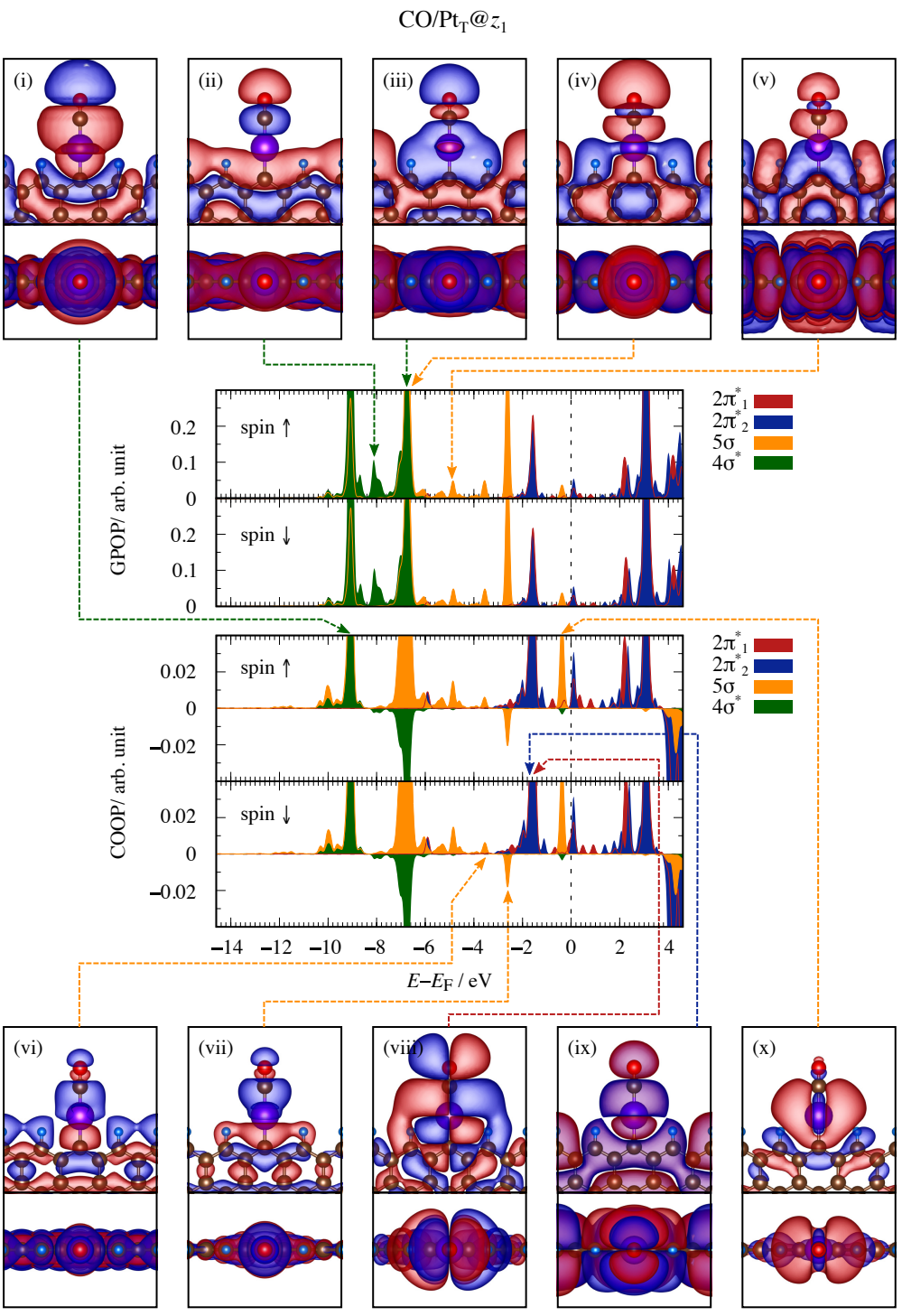

FIGURE B.7: GPOPs and COOPs of CO on Pt$_T$@z_1. The $2\pi^*_1$, $2\pi^*_2$, 5σ, and $4\sigma^*$ orbitals are shown in red, dark-blue, orange, and green filled lines, respectively. Energy zero is set to the Fermi level (E_F). Wave functions which correspond to some peaks are shown.

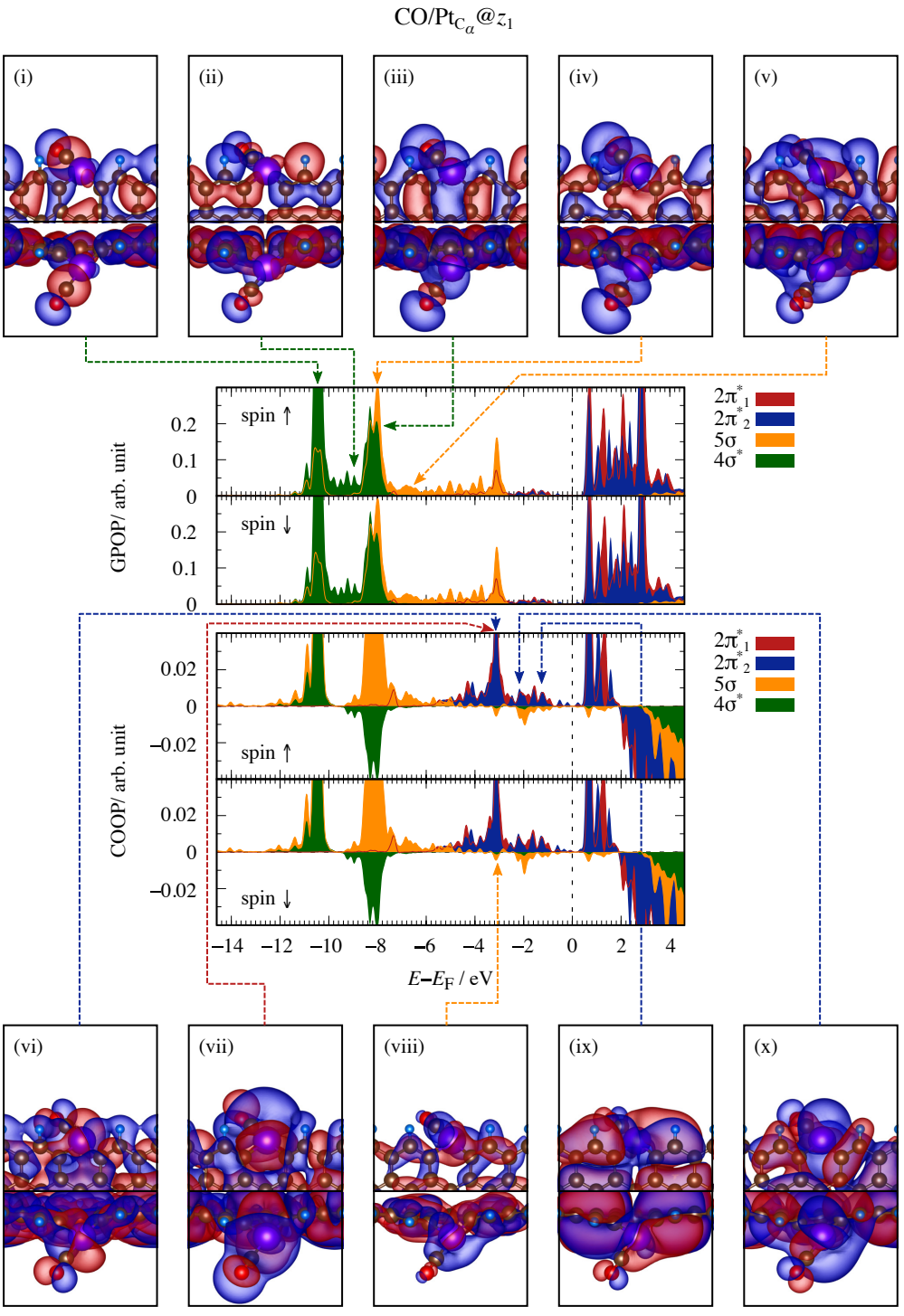

FIGURE B.8: GPOPs and COOPs of CO on Pt$_{C_\alpha}$@z_1. The $2\pi^*_1$, $2\pi^*_2$, 5σ, and $4\sigma^*$ orbitals are shown in red, dark-blue, orange, and green filled lines, respectively. Energy zero is set to the Fermi level (E_F). Wave functions which correspond to some peaks are shown.

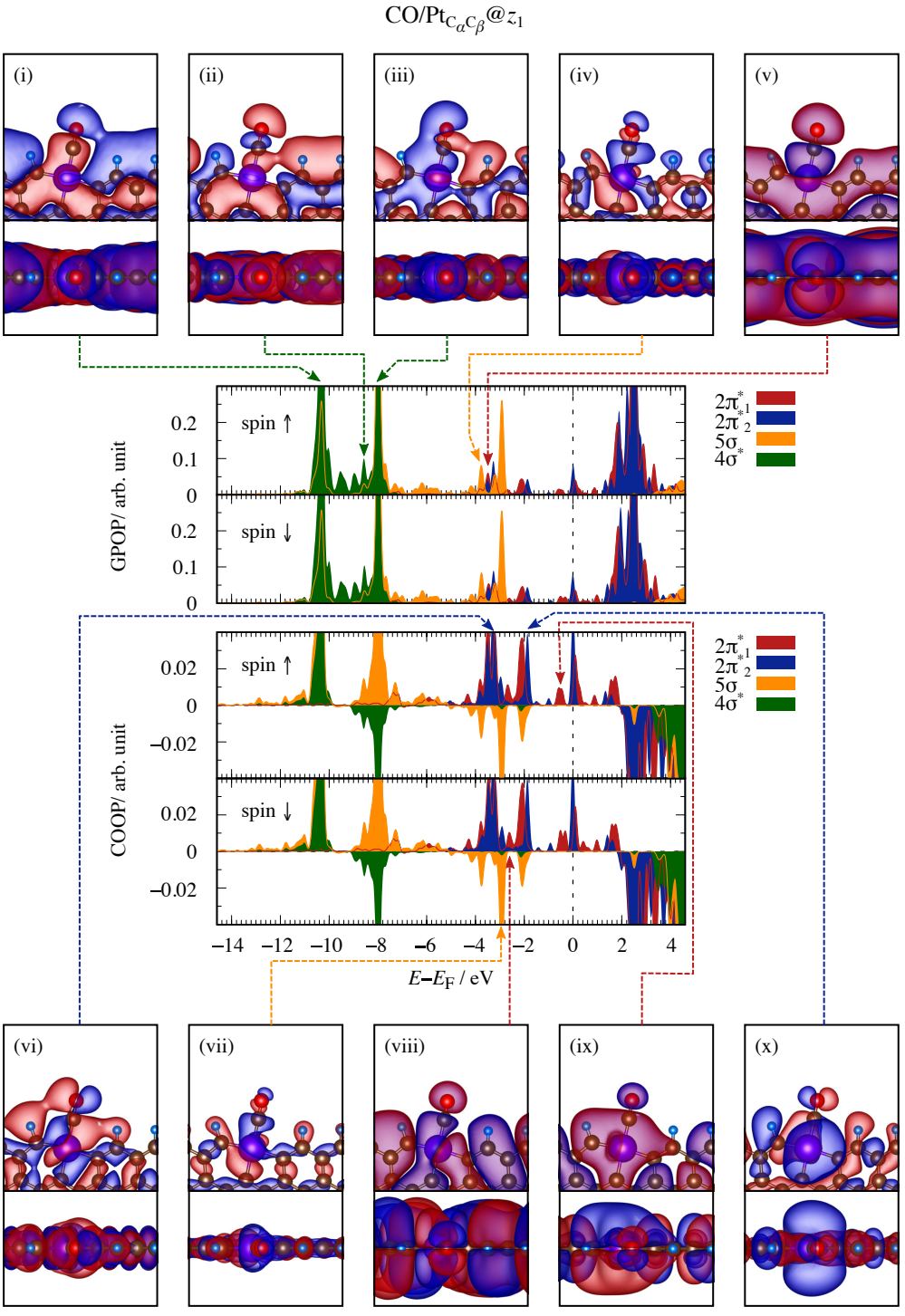

FIGURE B.9: GPOPs and COOPs of CO on Pt$_{C_\alpha C_\beta}$@z_1. The $2\pi^*_1$, $2\pi^*_2$, 5σ, and $4\sigma^*$ orbitals are shown in red, dark-blue, orange, and green filled lines, respectively. Energy zero is set to the Fermi level (E_F). Wave functions which correspond to some peaks are shown.

B.6 OH/Pt$_1$

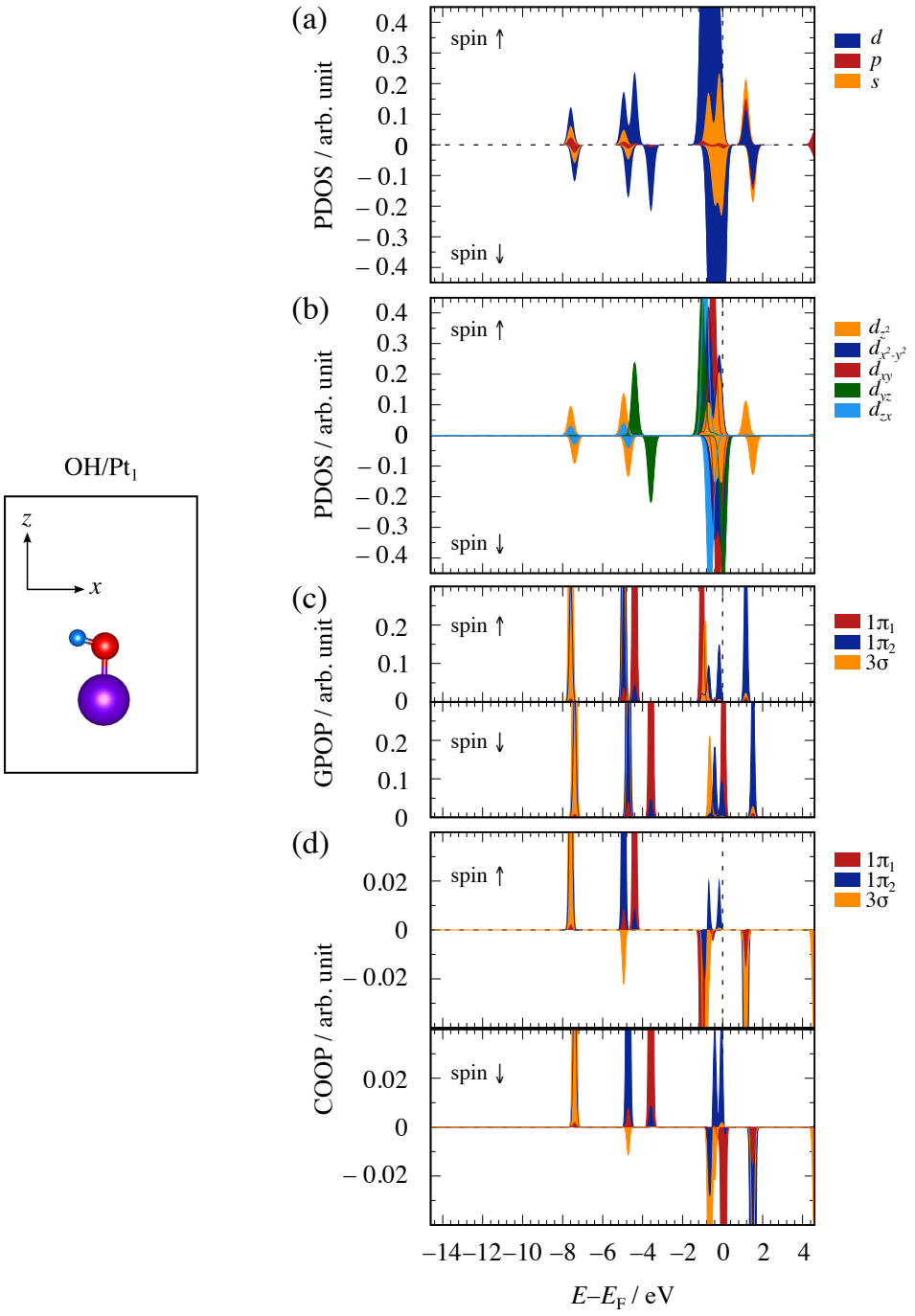

FIGURE B.10: (a) Density of states projected onto Pt s (orange), p (red), and d (dark-blue) states, and (b) m-resolved density of states of Pt atom for CO/Pt$_1$ system. GPOPs (c) and COOPs (d) of OH on single Pt atom. The $1\pi_1$, $1\pi_2$, and 3σ orbitals are shown in red, dark-blue, and orange filled lines, respectively. Energy zero is set to the Fermi level (E_F).

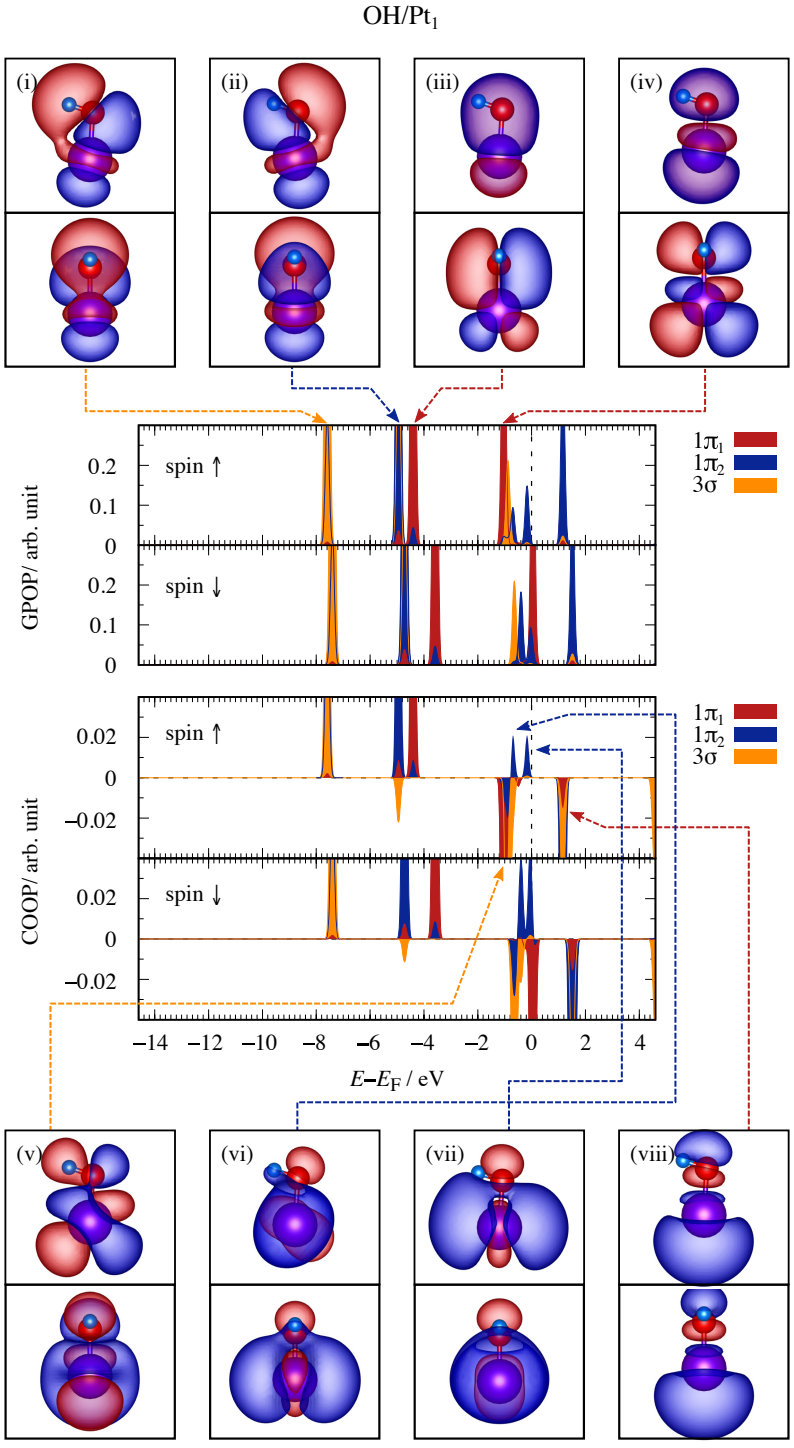

FIGURE B.11: GPOPs and COOPs of OH on single Pt atom. The $1\pi_1$, $1\pi_2$, and 3σ orbitals are shown in red, dark-blue, and orange filled lines, respectively. Energy zero is set to the Fermi level (E_F). Wave functions which correspond to some peaks are shown.

B.7 OH/Pt@GNRs

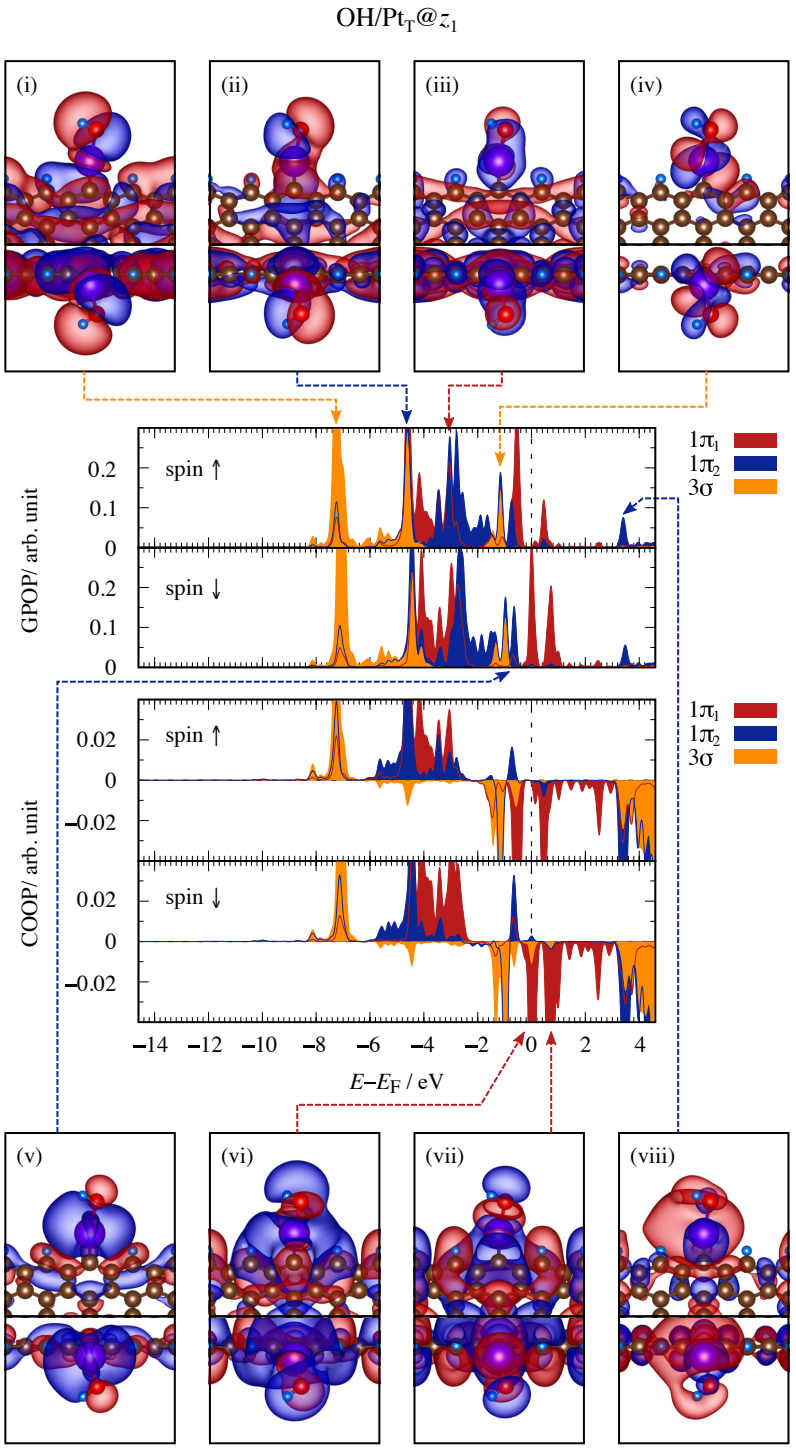

FIGURE B.12: GPOPs and COOPs of OH on on Pt$_T$@z_1. The $1\pi_1$, $1\pi_2$, and 3σ orbitals are shown in red, dark-blue, and orange filled lines, respectively. Energy zero is set to the Fermi level (E_F). Wave functions which correspond to some peaks are shown.

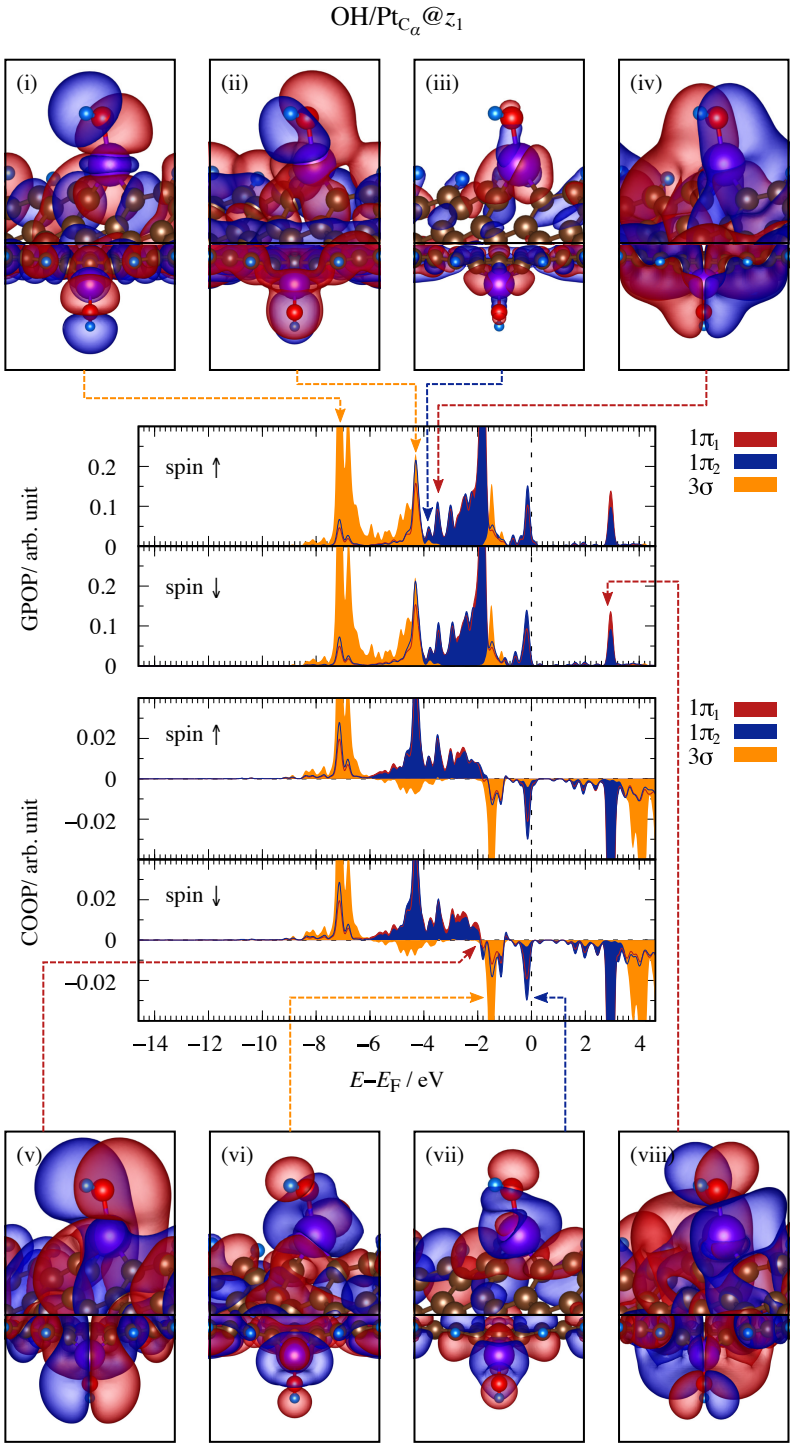

FIGURE B.13: GPOPs and COOPs of OH on on $Pt_{C_\alpha}@z_1$. The $1\pi_1$, $1\pi_2$, and 3σ orbitals are shown in red, dark-blue, and orange filled lines, respectively. Energy zero is set to the Fermi level (E_F). Wave functions which correspond to some peaks are shown.

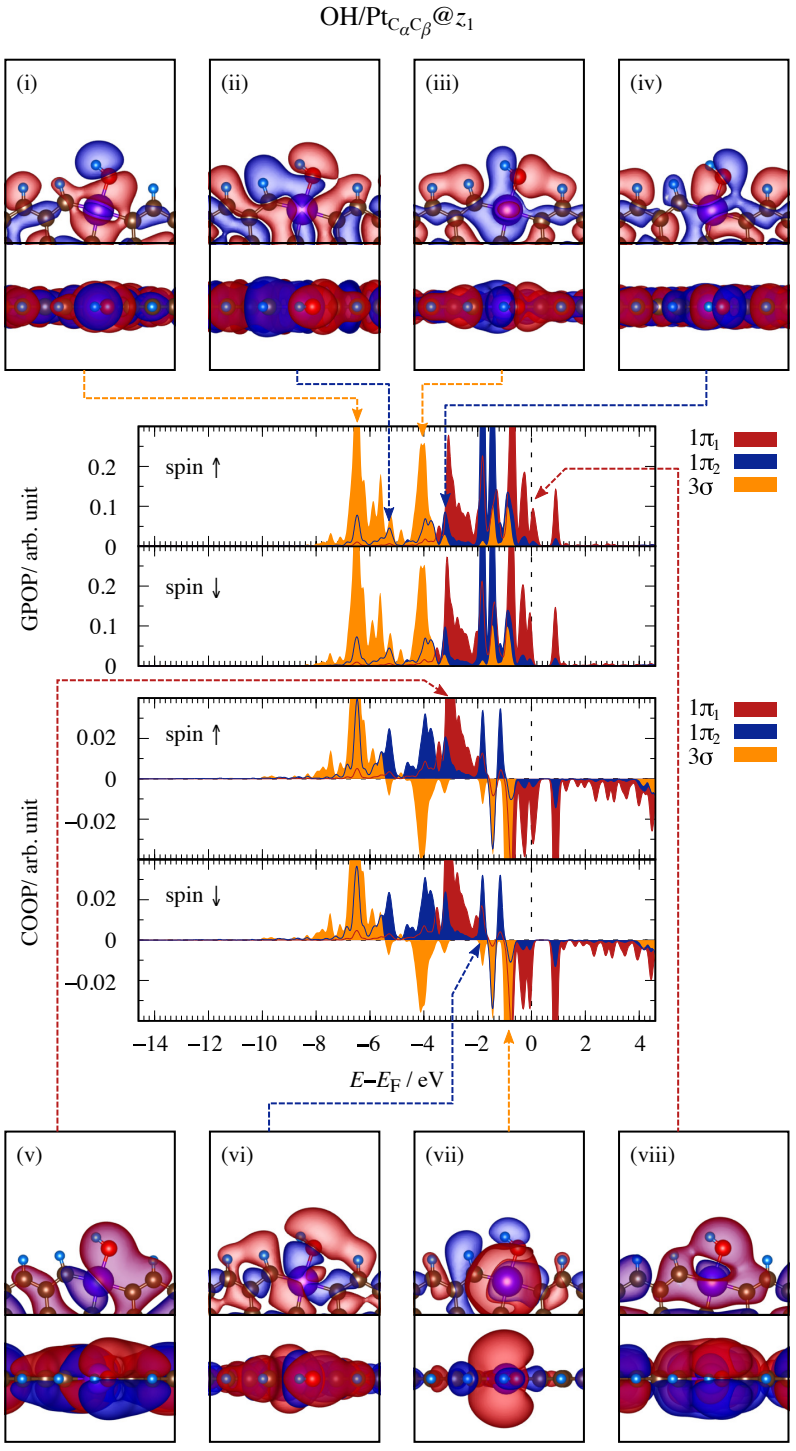

FIGURE B.14: GPOPs and COOPs of OH on on Pt$_{C_\alpha C_\beta}$@z_1. The $1\pi_1$, $1\pi_2$, and 3σ orbitals are shown in red, dark-blue, and orange filled lines, respectively. Energy zero is set to the Fermi level (E_F). Wave functions which correspond to some peaks are shown.

Appendix C

Energy diagrams of Molecular Orbitals

In this Appendix, I provide the energy diagrams of CO and radical OH molecular orbitals.

C.1 CO Molecule

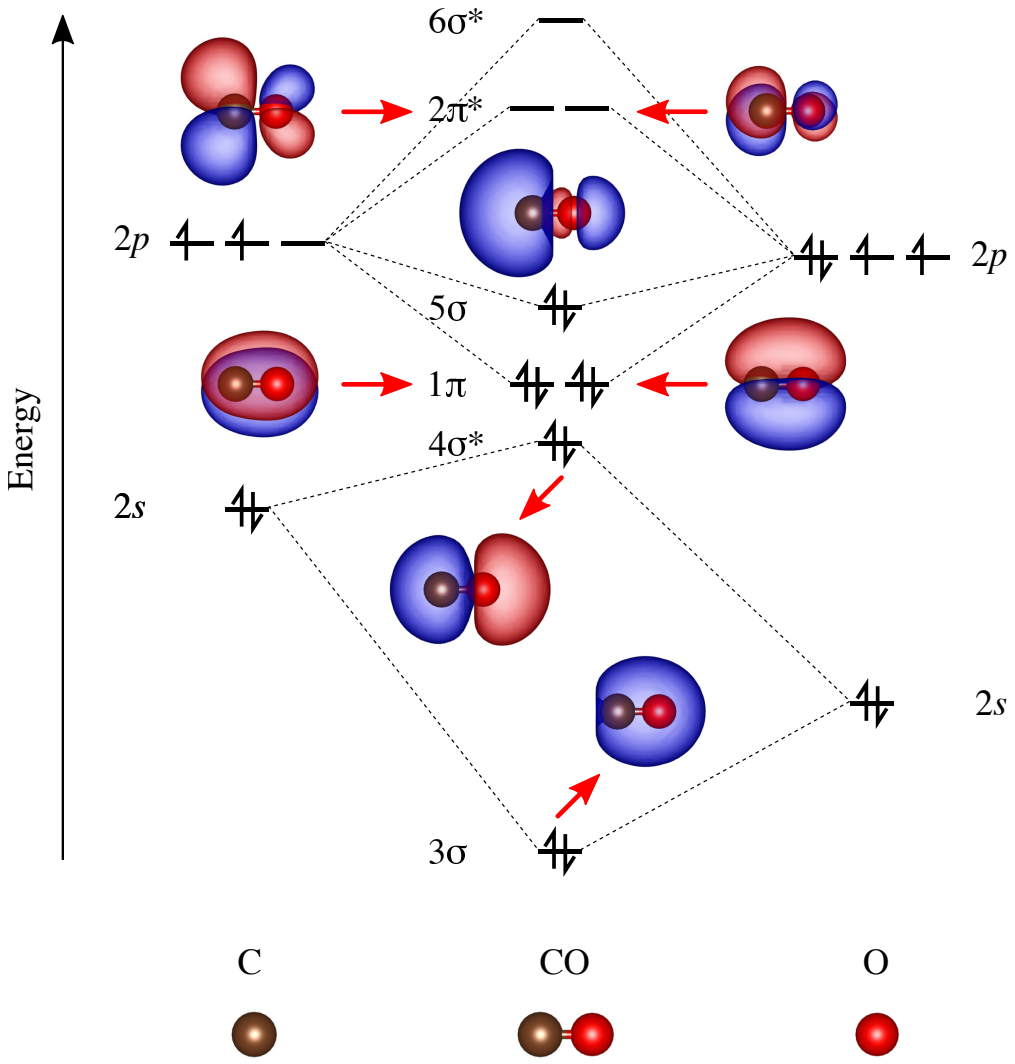

FIGURE C.1: Energy diagram of of carbon monoxide (CO) molecular orbitals. Wave functions which correspond to each molecular orbital are shown.

C.2 OH Molecule

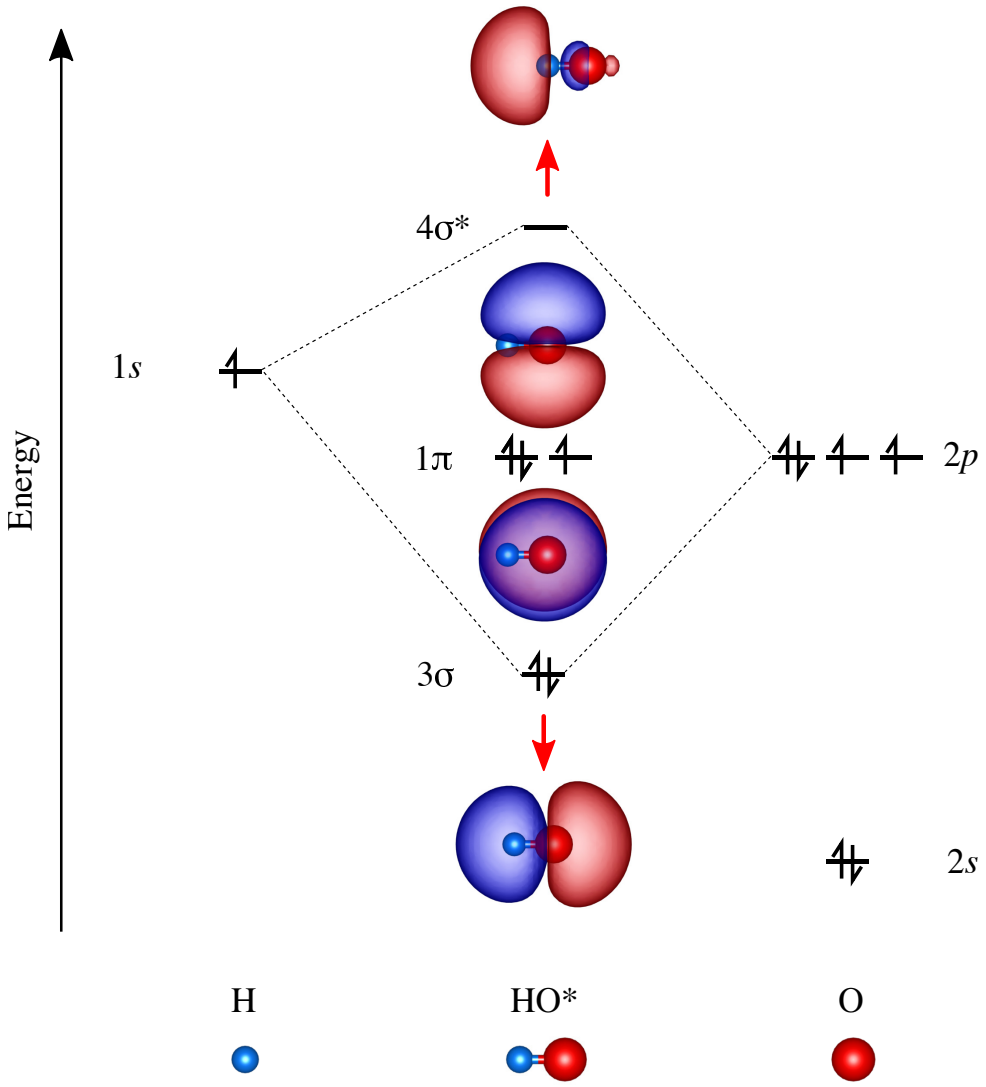

FIGURE C.2: Energy diagram of hydroxyl (OH) radical molecular orbitals. Wave functions which correspond to each molecular orbital are shown.

Acknowledgements

First, I would like to give my highest praise for **Jesus Christ** who makes all things become possible. He gave me strong and courage to face all my problems, especially during my study in Japan and in Indonesia. Thank you, Lord. You have been so good to me.

My greatest gratitude for all my supervisors, **Prof. Yoshitada Morikawa**, **Assoc. Prof. Ikutaro Hamada**, **Assist. Prof. Yuji Hamamoto**, **Prof. Suprijadi** and **Assoc. Prof. Ferry Iskandar** for their best advice, motivation supports, and patience in supervising me during my study both in Osaka University and in Institut Teknologi Bandung. They often gave me opportunity to explore my talent, my potential to be a better one, both in academic and life. *Doumo arigatou gozaimasu, sensei!*

I would like to acknowledge **Prof. Yuji Kuwahara** and **Prof. Tamio Oguchi** for their willingness to be vice examiners in my doctoral dissertation. I am also immensely grateful to **Prof. T. Munakata** and **Assist. Prof. T. Yamada** for the fruitful discussions about organic molecule on solid surface; and also to **Prof. J. Nakamura**, **Prof. J. Yoshinobu**, **Prof. K. Gohara**, **Assoc. Prof. T. Kondo**, **Assist. Prof. K. Yamazaki**, and **Dr. Y. Maehara** for providing prior publications and for the insightful discussions about platinum-based catalyst.

For my lovely family, **Keluarga Besar Op. Claudio Limbong**, thanks for the support in words, prayers and actions, in such I can reach my dreams. God bless you abundantly.

My sincere thanks also goes to all secretaries in Morikawa Laboratory: **Yamaguchi-san**, **Sakai-san**, **Baba-san**, and **Tanaka-san** for their help about the administration things during my stay in Osaka. Thanks for all friends in Morikawa Laboratory, in Quantum Engineering Design Course (QEDC) Program, in Minoh International Church (MIC), and in Indonesia for their continuous support and encouragement.

I would also like to thank to **Marubun Research Promotion Foundation**, Japan Student Services Organization (**JASSO**), and **WCU-ITB Sandwich Program** for the financial support during my study in Japan. This study was partly

supported by Grants-in Aid for Scientific Research on Innovative Areas "3D Active-Site Science" (Grants No. JP26105010, JP26105011, and JP15K21719) and "Molecular Architectonics" (Grant No. JP25110006); Grant-in-Aid for Young Scientists (B) (Grant No. JP15K17682) from the Japan Society for the Promotion of Science (JSPS); the Advanced-Catalytic-Transformation program for Carbon utilization (ACT-C) of Japan Science and Technology Agency (JST), "Elements Strategy Initiative for Catalysts & Batteries" (ESICB) supported by the Ministry of Education Culture, Sports, Science and Technology, Japan (MEXT); and the JSPS Core-to-Core Program (Type A) "Advanced Research Networks: Computational Materials Design on Green Energy." The numerical calculations in this work have been done with the facilities of the Supercomputer Center, Institute for Solid State Physics, University of Tokyo.

Sasfan Arman Wella

Biography

List of Publications

1. S. A. Wella, H. Sawada, N. Kawaguchi, F. Muttaqien, K. Inagaki, I. Hamada, Y. Morikawa, and Y. Hamamoto, "Hybrid Image Potential States in Molecular Overlayers on Graphene," *Phys. Rev. Materials*, vol. 1, p. 061001 (R), 2017.

2. S. A. Wella, Y. Hamamoto, Suprijadi, Y. Morikawa, and I. Hamada, "Platinum Single-atom Adsorption on Graphene: A Density Functional Theory Study," *Nanoscale Adv.*, vol. 1, p. 1165-1174, 2019.

3. S. A. Wella, Y. Hamamoto, F. Iskandar, Suprijadi, Y. Morikawa, and I. Hamada, "Atomic and Molecular Adsorption on Single Platinum Atom at the Graphene Edge: A Density Functional Theory Study," (submitted to *J. Chem. Phys.*).

List of Presentations

1. S. A. Wella, N. Kawaguchi, F. Muttaqien, K. Inagaki, Y. Hamamoto I. Hamada, and Y. Morikawa, Study of Naphthalene Adsorption on Graphene (Oral), The 71st Annual Meeting of the Physical Society of Japan (JPS), Sendai, Japan, March, 2016.

2. S. A. Wella, N. Kawaguchi, F. Muttaqien, K. Inagaki, Y. Hamamoto I. Hamada, and Y. Morikawa, Naphthalene Adsorption on Graphene: a van der Walls Density Functional Study (Oral), The 32nd European Conference on Surface Science (ECOSS), Grenoble, France, August, 2016.

3. S. A. Wella, N. Kawaguchi, F. Muttaqien, K. Inagaki, Y. Hamamoto I. Hamada, and Y. Morikawa, First Principles Analysis of Naphthalene on Graphene at High Coverage (Poster), The 2016 Autumn Meeting of the Physical Society of Japan (JPS), Kanazawa, Japan, September, 2016.

4. S. A. Wella, N. Kawaguchi, F. Muttaqien, K. Inagaki, Y. Hamamoto I. Hamada, and Y. Morikawa, Naphthalene Adsorption on Graphene (Oral), Kansai Thin Film and Surface Physics Seminar 2016, Kobe, Japan, November, 2016.

5. S. A. Wella, N. Kawaguchi, H. Sawada, F. Muttaqien, K. Inagaki, I. Hamada, Y. Morikawa, and Y. Hamamoto, A van der Waals Density Functional Study of Image Potential States of Naphthalene/Graphene Interface (Oral), International Conference on Computation in Science and Engineering (ICCSE) 2017, Bandung, Indonesia, July, 2017.

6. S. A. Wella, H. Sawada, N. Kawaguchi, F. Muttaqien, K. Inagaki, I. Hamada, Y. Morikawa, and Y. Hamamoto, First Principles Calculation of Unoccupied States of Monolayer Naphthalene on Graphene (Oral), The Japan Society for Precision Engineering Autumn Meeting 2017, Osaka, Japan, September, 2017.

7. S. A. Wella, H. Sawada, N. Kawaguchi, F. Muttaqien, K. Inagaki, I. Hamada, Y. Morikawa, and Y. Hamamoto, Hybridization of Low-lying Image Potential States at Naphthalene/Graphene (Oral), International Symposium on Nanoscience and Nanotechnology in Life 2017, Surabaya, Indonesia, November, 2017.

8. S. A. Wella, H. Sawada, N. Kawaguchi, F. Muttaqien, K. Inagaki, I. Hamada, Y. Morikawa, and Y. Hamamoto, Hybridization of Image Potential States of Naphthalene on $2\sqrt{3} \times 2\sqrt{3}$ R30° Structure of Graphene (Oral), International Symposium on Computational Science 2018, Bandung, Indonesia, May, 2018.